ACTIVE 3D DIFFRACTIVE OPTICS

by

HAIYAN WANG

B.S., Huazhong University of Science and Technology, 2008

M.S., Huazhong University of Science and Technology, 2012

M.S., University of Colorado Boulder, 2015

A thesis submitted to the

Faculty of the Graduate School of the

University of Colorado in partial fulfillment

of the requirement for the degree of

Doctor of Philosophy

Department of Electrical, Computer, and Energy Engineering

2019

This thesis entitled:
Active 3D Diffractive Optics
written by Haiyan Wang
has been approved for the Department of Electrical, Computer, and Energy Engineering

Prof. Rafael Piestun

Prof. Kelvin Wagner

Date_____

The final copy of this thesis has been examined by the signatories, and we find that both the content and the form meet acceptable presentation standards of scholarly work in the above mentioned discipline.

Wang, Haiyan (Ph.D., Electrical Engineering)

Active 3D Diffractive Optics

Thesis directed by Professor Rafael Piestun

Diffractive optics have increasingly captured the attention of the scientific community. Classical diffractive optics are 2D diffractive optical elements (DOEs) and computer-generated holograms (CGHs), which modulate optical waves on a solitary transverse plane along the direction of propagation. However, potential capabilities are missed by the inherent two-dimensional nature of these devices. Previous work has demonstrated that extending the modulation from planar (2D) to volumetric (3D) enables new functionalities, such as generating space-variant functions, multiplexing in the spatial or spectral domain, or enhancing information capacity. Unfortunately, despite significant progress fueled by recent interest in metasurface diffraction, 3D diffractive optics still remains relatively unexplored.

This thesis presents research on 3D diffractive optics in various aspects. First, to model and design 3D diffractive optics, two different approaches are presented: full-volume approach and stratified-layer approach. For each of them we analyze strengths and weaknesses. Second, to encode and multiplex information, algorithms are developed to iteratively optimize the volumetric structure to modulate light in the spatial, spectral, and frequency domains. Third, to realize the engineered devices, different methods are used including ultrafast laser direct writing, dynamic spatial light modulator (SLM) implementation, and photolithography.

Furthermore, I implemented 3D diffractive optics on a 2D SLM for dynamic operation for the first time. I also encoded multiple pages of information in the azimuthal dimension of 3D diffractive optics, showing a new type of multiplexing scheme, named azimuthal multiplexing. I explore active 3D diffractive optics numerically and experimentally, with the system performance investigated in terms of efficiency, scaling, and limits.

Dedication

To family and friends who always offer me love and support.

Acknowledgements

Pursing Ph.D. is a strenuous journey. I am so blessed to have met a number of people during this unforgettable period of my life, without whom I would not be where I am.

First and foremost, my advisor Professor Rafael Piestun, to whom I owe the most gratitude. He led me to this magic realm with his sharp vision, and guided me through it with his profound knowledge. He illustrates me the right path when I get stuck, and releases the rein when I get back on the track. He always encourages me to conduct research tasks independently, and allows me the freedom to chase my own ideas. He constantly provides me inspiring ideas and enthusiastically supports me to attend conferences for more. It is with the safe net, both scientifically and financially, he endeavored to provide, that I become a better researcher and better person in general. It is with him that there is more joy and less pain on my journey. I could not have asked for a better advisor.

Next, I would like to acknowledge my thesis committee Prof. Kelvin Wagner, Prof. Robert McLeod, Prof. Alexander Jesacher, and Prof. Shu-Wei Huang, for their time to supervise my dissertation and all the helpful discussions over the years. I am lucky to have met various superstars in my research field who generously offer provoking thoughts and tremendous encouragements; among them Prof. Joseph Goodman, Prof. David Miller, Prof. Dimitri Psaltis, Prof. Eugene Arthurs, Prof. Sylvian Gigan, and Prof. Monika Ritsch-Marte.

I am also grateful to all of the past and current members in Piestun's group, Dr. Ariel Libertun, Dr. Donald Conkey, Mr. Eyal Niv, Dr. Ginni Sharma, Dr. Anthony Barsic, Dr. Anurag Agrawal, Dr. Antonio Caravaca, Dr. Jian-wei Tay, Dr. Omer Tzang, Dr. Simon Labouesse, Ms. Evolene Premillieu, Ms. Sakshi Singh, Ms. Sarah Kerr, for their friendship, support, and collaboration. In particular, I would like to thank Dr. Wenjian Cai, Dr. Timothy Gerke, and Mr. Jeremy Brown for their previous efforts in this direction, which helped springboard my work to a new level. I would also like to thank my undergraduate assistants, Ms. Megan Borfitz and Ms. Carmen Vogt, who are the most motivated and talented students I have ever seen.

Last but not least, thanks go to my family and friends. It is their endless love that provides me shelter at the most frustrating moments and panacea to preserve inner peace in the everyday life.

CONTENTS

CHAPTER

TABLES

Table

FIGURES

Figure

Chapter 1

Introduction

1.1 Background

With feature sizes comparable to the electromagnetic wavelength, diffractive optics offers a unique pathway to light manipulation [1–3]. It expands the capabilities of conventional optics based on refraction or reflection and in conjunction with free-form [4,5], graded index [6], and artificial (meta) materials [7,8], provide full access to the spatial degrees of freedom of light.

Since its invention in 1948 by Gabor [9], holography has attracted tremendous attention from scientists. However, the majority of efforts in diffractive optics have been placed on gratings, a well-known optical element that couple an input wave into different output waves [10]. These planar periodic devices are simple to study because they essentially change the wave vector only in the transverse plane. Volume gratings and volume holograms expanded the capability to control light fields selectively. In 1967, Lohmann introduced the first computer-generated hologram (CGH), where an arbitrary pattern could be obtained without the original object to physically exist [11]. Hence begins a new era of diffractive optics designed by computers. The computer-

generated diffractive optics boosted applications in various fields, as some functions are very difficult or even impossible for conventional optics. For instance, Joseph Rosen demonstrated volume holograms optically recorded by CGHs that achieve multiplexing [12]. Rafael Piestun designed diffractive optical elements (DOEs) using iterative optimization algorithms to control light field in a three dimensional space [13]. Brogsmuller and coworkers then stacked the 2D DOEs together to achieve properties only available in volume hologram such as one diffraction order and multiplexing [14]. It is not until 2006 that Wenjian Cai developed the first strictly speaking computer generated volume hologram, also known as CGVH [15]. Therefore, if we divide diffractive optics into thin or thick, and by method optically recorded or computer generated (Table 1.1), most research has been done in the other three categories, except computer-generated 3D diffractive optics which is largely unexplored.

	Optically Recorded	Computer Generated
2D-thin	holographic optical elements (HOEs)	diffractive optical elements (DOEs)
3D-thick	volume holograms	**computer-generated 3D diffractive optics**

Table 1.1 Diffractive optics categorized by thickness (thin and thick), and by generation method (optically-recorded and computer-generated).

3D diffractive optics expand the capabilities of traditional two-dimensional elements not only by providing higher diffraction efficiency and higher information capacity, but also enabling functionalities such as multiplexing and space-variant functions [16,17]. The capability of controlling multidimensional spatial, spectral,

temporal, and coherence functions of light fields is originated from the multi-subject nature of 3D diffractive optics involving diffraction, refraction, absorption, resonances, and scattering.

In spite of being a topic of great interest, 3D diffractive optics have not been fully investigated due to their physical and mathematical complexity, where the challenge stems from three aspects: First, the wavefront propagation must obey Maxwell's equations, while most arbitrary target patterns do not, causing the problem to be inconsistent. Second, the finite degrees of freedom due to finite volumetric space-bandwidth and limited phase/amplitude modulation narrows the scope of possible solutions. Third, the interaction of novel physical phenomena within the volumetric optics and the need for multiplexing increasing information calls for mathematical models where multiple interdependent design metrics are optimized simultaneously. Moreover, it is often important to distribute the information evenly, within a relatively small volume under control.

Nowadays, new insight in wave manipulation and the ever-increasing power of computers enable diffractive optics to generate user-defined wavefronts from arbitrary inputs, by virtue of degrees of freedom from pixels that can be addressed individually and independently. As a result 3D diffractive optics become useful beyond classical applications such as beam shaping [18,19], 3D display [20,21], information security [22,23], spectroscopy [24], metrology [25], and astronomical imaging [26], emerging areas include optical tweezers [27,28], novel microscopies [29,30], coherent control [31,32], quantum information [33,34], neural networks [35,36], and optogenetics [37,38].

1.2 Active wavefront control

Modern photonic applications call for optical devices that can modulate light fields in multiple dimensions while changing parameters in real time. For instance, deformable mirrors create topography modulation with a reflective membrane which can be selectively distorted by actuators [39]. They are the core components in adaptive optical systems to correct low-order aberrations in astronomical or ophthalmic imaging. Electronically tunable lenses are used in 3D imaging where the focal lens can be controlled by the current [40]. For satellite quantum communications and light detection and ranging (LIDAR), beam steering and active control is essential. This section provides a brief overview of the state-of-art technologies for active wavefront control.

Liquid crystal spatial light modulators (SLM) are widely available optical components capable of modulating light fields with a liquid crystal layer on a silicon substrate which can be controlled by the voltage applied on it. They have become critical elements in applications such as beam shaping, optical tweezers, optogenetics, laser lithography, point-spread function (PSF) engineering, and dynamic structured illumination, all of which are at the forefront of current optics research.

The digital mirror device (DMD) consists of a large number of reflective aluminum micromirrors in an optical micro-electrical-mechanical system (MEMS). It can operate in high frequency but only in binary fashion. Therefore, they are suitable for applications in confocal microscopy, hyperspectral imaging, and compressive sensing [41].

Deformable mirrors are reflective optical devices composed of a membrane that can be continuously changed by pixelized actuators. With the feedback provided from

wavefront sensors, the topography control by deformable mirrors is capable of compensating low-order aberrations in real time. The process is called adaptive optics, which is beneficial for astronomical and ophthalmic imaging.

Freeform optics, originated in the 1990s, is considered to be a revolution in optical system design [42]. The most commonly used surface in optical devices and systems is spherical, for the following two reasons. First, spherical surfaces are simple, which allows straightforward approximate analysis based on geometrical and paraxial approximations. The analysis of spherical lenses was started early on in 1841 by Gauss. The second reason is that spherical surfaces are easy to manufacture, which includes cutting, grinding, polishing, and coating of glass. In the machining process, glasses are pushed towards abrasive tools with curtain curvatures, while both of them are spinning along different axes. Obviously, this method only works for spherical surfaces. However, if the beam size and propagation direction are not small enough to keep the paraxial approximation valid, geometric aberrations would occur. Meanwhile, optical beams with different wavelength undergo different refractions, which results in chromatic aberrations. On the other hand, freeform optics has no translational or rotational symmetry around an optical axis, allowing more degrees of freedom accessible to the designers. Together with the ever-growing computational power, optimization designs involving heavy computation are becoming feasible, enabling freeform optics designed by computers to become capable of compensating higher order aberrations and thus reducing the number of elements in the optical system. In 1982, Kodak introduced the first low cost massive production of aspherical lenses. Today, it is very common to find them in camera lenses and projection lens. Besides, freefrom optics are also applied in optical see through head-mounted displays (HMD), confocal photovoltaic (CPV), and augmented reality/virtual reality (AR/VR). Recently, researchers propose and demonstrate the use of thermal effects for active wavefront control with freeform optics [43].

Over the past few years, a family of metasurfaces emerged as fundamentally new pathway for wavefront engineering [44]. Metasurfaces are structured layers with features sizes below the optical wavelength, which can interact with light fields by scattering from dielectric nanostructures. As a result, desired phase, polarization, mode, and spectrum can be obtained. The most commonly investigated metasurfaces are metalenses. For instance, high NA metalenses are developed for compact microscopy imaging systems. Doublets metalenses are designed to compensate aberrations such as coma and astigmatism. Although they only work for a certain wavelength, like most diffractive optics, efforts have been made to address the dispersion, and have shown promising results for broadband operation. Metasurfaces also allow for phase-only or complex encoding, so called metaholograms, which could avoid recording and fabrication in bulky media as opposed to the traditional holography. For multi-wavelength operation, several metaholograms can be intertwined on a single flat surface, each provides full phase control for the corresponding wavelength [45]. Efforts have also been made to control the modulation dynamically and arbitrarily, enabling the transformation from passive metasurface to active metasurface, by applying voltage or physical force on phase change materials [46]. Reconfigurable matesurfaces are not only capable of tuning the parameters for a specific operation but also capable of performing completely different functions. By virtue of this versatility, a number of applications are proposed including self-driving automobile and dynamic holographic display, both are the new frontier of the research in the field.

The timeline for major milestones in diffractive optics historic development is summarized as in Fig. 1.1.

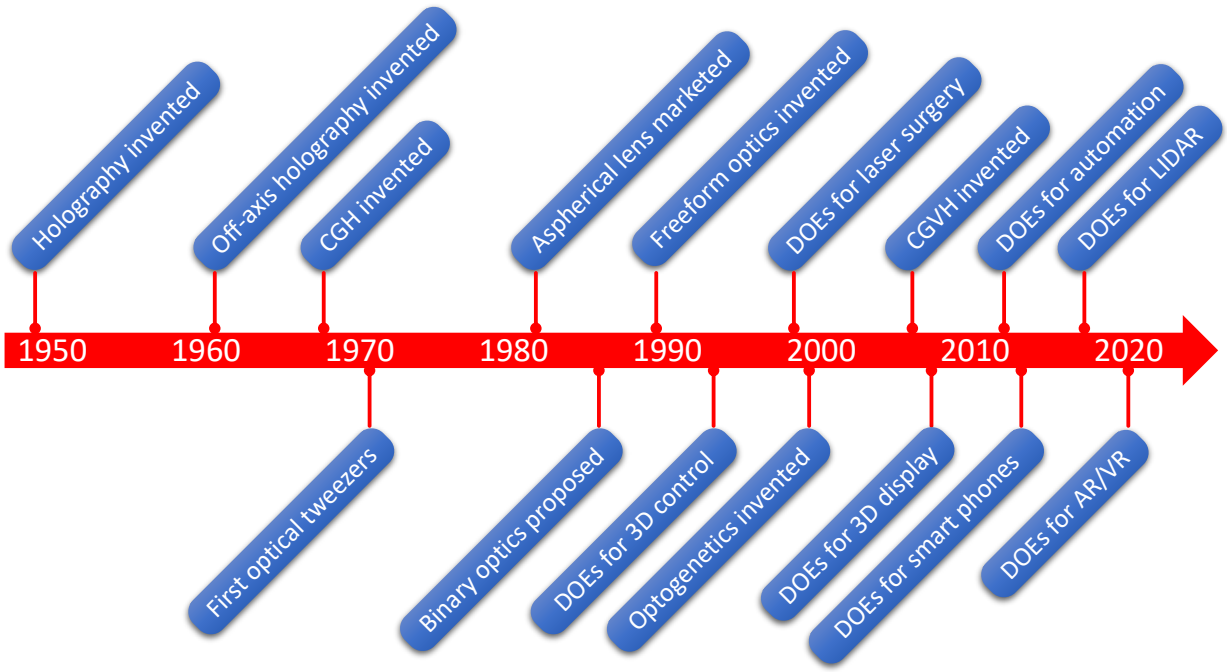

Figure 1.1 Timeline for major diffractive optics milestones.

1.3 Outline of the thesis

In this thesis, several topics in active 3D diffractive optics are discussed. Each topic includes a theoretical approach, experimental demonstration, a discussion of system performance, and conclusions.

Chapter 2 presents the design and implementation of 3D diffractive optics with full-volume approach. The volume of interest is considered as a whole. Under 3D scattering theory and Born/Rytov approximation, the reconstructed wave can be represented on a particular sphere (Ewald sphere) in the frequency domain. By applying coding/fabrication constraints in spatial domain and target constraints in frequency domain, the projection onto convex sets algorithm is built where the two domains are connected via 3D Fourier transforms. The design results show

multiplexing property as predicted. We also design large volumetric space-bandwidth 3D diffractive optics, and shift multiplexing 3D diffractive optics.

Chapter 3 introduces an alternative for the design and implementation of 3D diffractive optics. Instead of considering the volume as a whole, it can be represented by multiple thin elements cascaded with optical uniform region in between. We build physical model and compute the propagation of optical waves with in the 3D diffractive optics. Using iterative projection optimization algorithm with distribution on layers method, we design the device showing multiplexing. We also discuss the system performance and limitations.

Chapter 4 shows how 3D diffractive optics with stratified-layer approach enables the implementation on spatial light modulators for dynamic operation. With an imaging system, the stacked layers can be flattened on a 2D plane, while keeping its 3D features. In particular, angular multiplexing and frequency multiplexing are achieved with such devices. The system performance and limitations are also discussed.

Chapter 5 proposes a new multiplexing scheme, namely azimuthal multiplexing, based on 3D diffractive optics by stratified-layer approach. Multiple pages of information are encoded and can readout across independent channels by rotating one or more layers with respect to others. Compared with other multiplexing techniques, the azimuthal multiplexing is compact, efficient, and easy to implement without the need to change input parameters. Experimental results are obtained using photolithography method and are in good agreement with numerical results. The capabilities and limitations of the azimuthal multiplexing 3D diffractive optics are also discussed.

Chapter 2

3D Diffractive Optics by Full-volume Approach

2.1 Introduction

In this chapter, we outline an approach for designing 3D diffractive optics that considers the volume of the device as a whole. The diffractive volume optics are designed using a projection onto constraint sets optimization algorithm. As a model, we consider 3D scalar diffraction theory under weak scattering conditions based on the 1st Born approximation. Hence, the relationship between the volume index modulation and the scattered far-field is obtained via a 3D Fourier transform. We use the relationship between these two domains to create an iterative projection optimization algorithm. In addition, we explore the effect of scaling in volume optics performance.

Volumetric integrated-optical systems are becoming feasible with the latest developments in computational power and fabrication techniques. Previously unavailable design freedom for spatial and spectral functions is provided with the ability to control the material structure within a volume. For instance, volume structured materials have been tailored to control light using metamaterial, disordered media, and photonic crystals [47–49]. While periodic volumetric

structures have been thoroughly investigated, the domain of computer-designed aperiodic volumetric devices still remains largely unexplored. Computer-generated 3D diffractive optics enable control of the optical field via individually addressable voxels that can generate synthetic fields with encoding adapted to the technological fabrication constrains.

The space-bandwidth product (SW) is fundamental for evaluating the performance of classical optical systems. The SW of a system is defined as a number that counts the degrees of freedom of the system [50]. The information content of a volume optics device can be quantified by the volumetric space bandwidth (VSW), which is the product of the available space (size) and the available bandwidth in each dimension. A more rigorous method of counting the degrees of freedom when dealing with volume electromagnetic structures has been developed to target more applications [51,52]. The analysis of VSW will help elucidate the fundamental limitations and opportunities of volume optics in terms of functionality and scalability. Current volume optics designs and experimental demonstrations contain 2^{18} voxels [53]. While sufficient to prove the potential of multiplexing diffraction patterns in frequency and spatial (angular domain), it is still lacking for most applications.

Here, we expand the size of the aperiodic volumetric devices up to 2^{23} voxels. We investigate the diffraction efficiency and relative error as functions of index contrast and thickness. The numerical calculations show that computer-generated 3D diffractive optics with higher spatial bandwidth product can have higher diffraction efficiency, lower relative reconstruction error, and greater capability for multiplexing information due to their angular and frequency selectivity properties.

2.2 Theory and simulation

The idea behind 3D diffractive optics by full-volume approach is to consider a refractive index distribution in three-dimensional space. The index distribution is designed by computer such that when a wave propagates through, it will be shaped to generate a desired pattern on the reconstruction plane or volume. The schematic is shown in Fig. 2.1.

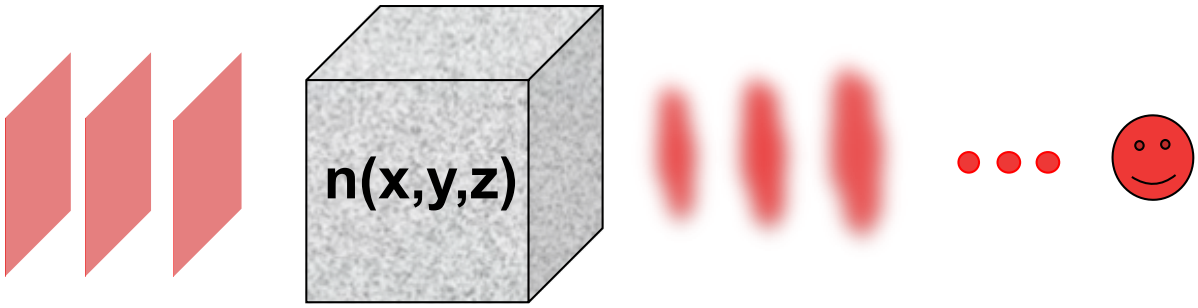

Figure 2.1 Schematic of 3D diffractive optics by full-volume approach.

Previous studies show that by extending the diffractive optics from 2D to 3D, many advantages can be realized such as enhanced design degrees of freedom, larger encoding capacity, increased diffraction efficiency, improved frequency and angular selectivity which can be used for multiplexing and easy integration to optical systems.

The diffractive volume optics are designed based on a 3D scattering approach and using a projection-onto-constraint-sets optimization algorithm [54,55]. The projection optimization algorithm is related to but more general than the phase retrieval algorithm [56,57], super-resolution algorithm [58,59], and the iterative Fourier transform algorithm [60]. While convergence is proven if the constraint sets are convex (for instance, continuous amplitude and phase), convergence to an acceptable solution can be realized even if the constraint sets are non-convex (for instance, binary amplitude, binary phase, discrete phase, or continuous phase) [61].

Given the wave nature of light, the Maxwell's equations set the foundation of classical electromagnetism and classical optics. They provide a mathematical model to analyze and synthesize wavefront distribution in 3D space.

$$\begin{cases} \nabla \times \vec{E} = -\dfrac{\partial \vec{B}}{\partial t} \\ \nabla \times \vec{H} = \dfrac{\partial \vec{D}}{\partial t} + \vec{J} \\ \nabla \cdot \vec{B} = 0 \\ \nabla \cdot \vec{D} = \rho \end{cases} \tag{2.1}$$

where $\vec{J}$ and ρ are electric current density and electric charge density, respectively.

The electric/magnetic field ($\vec{E}/\vec{H}$) and flux density ($\vec{D}/\vec{B}$) are linked by the constitutive equations

$$\begin{cases} \vec{D} = \varepsilon_0 \varepsilon \vec{E} \\ \vec{B} = \mu_0 \mu \vec{H} \\ \vec{J} = \sigma \vec{E} \end{cases} \tag{2.2}$$

Substituting $\vec{B}$ into the second Maxwell's equation and taking curl on both sides

$$\nabla \times \left(\frac{1}{\mu} \nabla \times \vec{E} \right) + \frac{1}{c} \frac{\partial \vec{H}}{\partial t} = 0 \tag{2.3}$$

Taking the derivative of the first Maxwell's equation and substituting for $\vec{D}$

$$\nabla \times \left(\frac{1}{\mu} \nabla \times \vec{E} \right) + \frac{\varepsilon}{c^2} \frac{\partial^2 \vec{E}}{\partial t^2} = 0 \tag{2.4}$$

Substituting $\vec{D}$ into the third Maxwell's equation, and use mathematical identities

$$\nabla^2 \vec{E} - \frac{\varepsilon \mu}{c^2} \frac{\partial^2 \vec{E}}{\partial t^2} + (\mathbf{grad} \ln \mu) \times \nabla \times \vec{E} + \mathbf{grad}\left(\vec{E} \cdot \mathbf{grad} \ln \varepsilon \right) = 0 \tag{2.5}$$

Consider a monochromatic wave incident on a scattering medium

$$\nabla^2 \boldsymbol{E}(\boldsymbol{r}, \omega) + k^2 \varepsilon(\boldsymbol{r}, \omega) \boldsymbol{E}(\boldsymbol{r}, \omega) + \mathbf{grad}[\boldsymbol{E}(\boldsymbol{r}, \omega) \cdot \mathbf{grad} \ln \boldsymbol{\varepsilon}(\boldsymbol{r}, \omega)] = 0 \tag{2.6}$$

Assume $\boldsymbol{\varepsilon}(\boldsymbol{r},\omega)$ varies slowly and set

$$\begin{cases} F(\boldsymbol{r},\omega)=\dfrac{1}{4\pi}k^2[n^2(\boldsymbol{r},\omega)-1] \\ \nabla^2U(\boldsymbol{r},\omega)+k^2U(\boldsymbol{r},\omega)=-4\pi F(\boldsymbol{r},\omega)U(\boldsymbol{r},\omega) \\ U(\boldsymbol{r},\omega)=U^{(i)}(\boldsymbol{r},\omega)+U^{(s)}(\boldsymbol{r},\omega) \\ (\nabla^2+k^2)U^{(i)}(\boldsymbol{r})=0 \end{cases}$$

where F is the scattering potential, and $U^{(i)}$ and $U^{(s)}$ are the complex amplitude of the incident wave and scattered wave, respectively. We obtain

$$(\nabla^2+k^2)U^{(s)}(\boldsymbol{r},\omega)=-4\pi F(\boldsymbol{r},\omega)U(\boldsymbol{r},\omega) \tag{2.7}$$

Defining the Green's function as

$$(\nabla^2+k^2)G(\boldsymbol{r}-\boldsymbol{r}',\omega)=-4\pi\delta^{(3)}(\boldsymbol{r}-\boldsymbol{r}')$$

then

$$\begin{aligned} U^{(s)}(\boldsymbol{r},\omega)=&\int_V F(r',\omega)U(r',\omega)G(\boldsymbol{r}-\boldsymbol{r}',\omega)d^3r' \\ &-\frac{1}{4\pi}\int_{S_R}\left[U^{(s)}(\boldsymbol{r}',\omega)\frac{\partial G(\boldsymbol{r}-\boldsymbol{r}',\omega)}{\partial n'}-G(\boldsymbol{r}-\boldsymbol{r}',\omega)\frac{\partial U^{(s)}(\boldsymbol{r}',\omega)}{\partial n'}\right]dS_R \end{aligned} \tag{2.8}$$

If we choose

$$G(\boldsymbol{r}-\boldsymbol{r}',\omega)=\frac{e^{ik|\boldsymbol{r}-\boldsymbol{r}'|}}{|\boldsymbol{r}-\boldsymbol{r}'|}$$

and

$$U^{(i)}(\boldsymbol{r},\omega)=e^{ik\boldsymbol{s_0}\cdot\boldsymbol{r}}$$

we finally obtain the integral equation for the scattering potential

$$U(\boldsymbol{r},\omega)=e^{ik\boldsymbol{s_0}\cdot\boldsymbol{r}}+\int_V F(r',\omega)U(r',\omega)\frac{e^{ik|\boldsymbol{r}-\boldsymbol{r}'|}}{|\boldsymbol{r}-\boldsymbol{r}'|}d^3r' \tag{2.9}$$

2.2.1 Born approximation

We start from a random index structure $n(\boldsymbol{r}, k_0)$, which is constrained to non-absorbing binary form (for fabrication) and fundamental physical limits. Consider three-dimensional scalar diffraction theory under weak scattering conditions based on the first Born approximation, the scattering potential can be expressed as:

$$F\left(\boldsymbol{r}, k_0\right) = \frac{1}{4\pi} k_0^2 \left[n^2\left(\boldsymbol{r}, k_0\right) - n_0^2 \right] \tag{2.10}$$

where k_0 is the magnitude of the wave vector in free space and n_0 is the refractive index of the material used. Next, using 3D Fourier transform to obtain the scattering potential in frequency domain:

$$\widetilde{F}\left(\boldsymbol{k}\right) \xleftrightarrow{\text{3D FT}} F\left(\boldsymbol{r}\right) \tag{2.11}$$

The far-field scattered wave is defined by a particular sphere (Ewald sphere) within the Fourier transform of the scattering potential, and can be extracted by

$$\widetilde{U}_S\left(\boldsymbol{k}_s\right) = \frac{e^{jkr}}{r} \widetilde{F}\left(\boldsymbol{k}_s - \boldsymbol{k}_i\right) \tag{2.12}$$

where $\boldsymbol{k}_s$ and $\boldsymbol{k}_i$ are wave vectors for scatted and incident waves, respectively. When multiplexing, two or more Ewald spheres are considered, with their positions depending on the direction of the incident wave (angular multiplexing), and their radius depending on the wavelength (frequency multiplexing), as shown in Fig. 2.2.

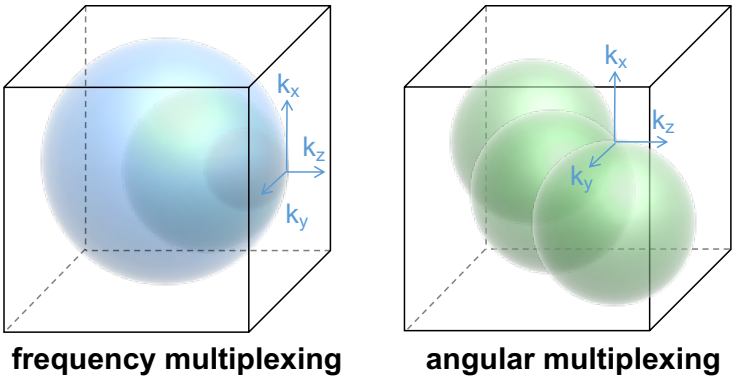

Figure 2.2 The radius of the Ewald sphere is related to the wavelength of the incident beam, which can be implemented for frequency multiplexing and angular multiplexing.

Hence, the relationship between the volume index modulation and the scattered far-field is obtained. We use the relationship between these two domains to create an iterative projection optimization algorithm. From equation (2.10) to (2.12), the far-field scattered wave can be computed from the initial index structure. The amplitudes are then updated to match the target through parallel projections, while the phases are kept. The new scattering potential is then obtained via an inverse 3D Fourier transform, where the coding and fabrication constraints are imposed. The optimization loop will iterate until a satisfactory result is reached. Fig. 2.3 shows the flowchart of multiplexing design algorithm.

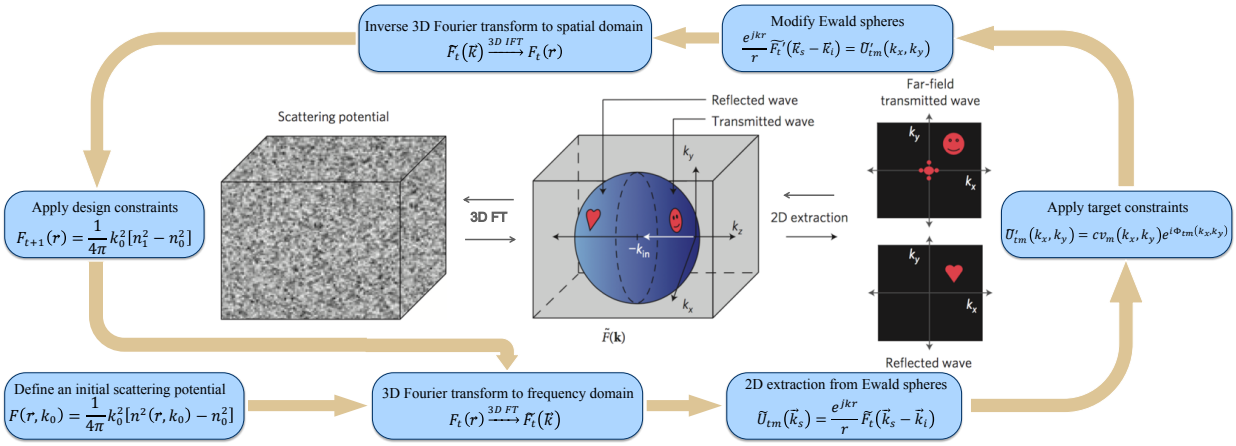

Figure 2.3 Flowchart of the iterative projection optimization algorithm for multiplexing design with 3D diffractive optics by full-volume approach.

We present the design results as a demonstration of principle. We use "CU" logo as our target. The 3D diffractive optics has 128×128×128 voxels, with the size of 1×1×5 μm for each voxel. The mean refractive index is 1.5, where the modulation is in binary fashion with index change of 10^{-3}. In frequency multiplexing, the letter "C" is encoded with 458nm illumination, and the letter "U" is encoded with 800nm illumination, both under normal incidence. The results are shown in Fig. 2.4.

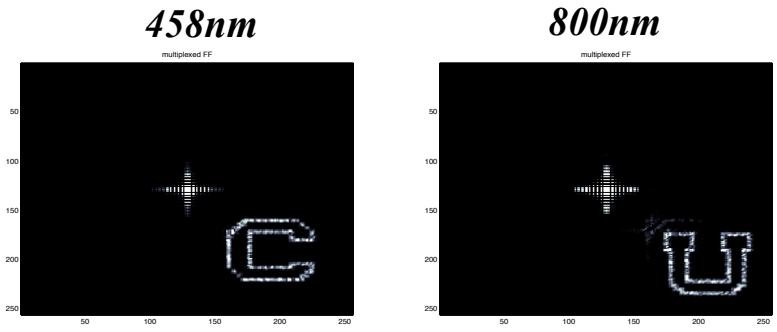

Figure 2.4 Simulation results for frequency multiplexing. Left: reconstruction image under 458nm illumination. Right: reconstruction image under 800nm illumination.

Figure 2.5 shows the diffraction efficiency of both letters as a function of iteration number. The algorithm converges to an acceptable solution, even though not necessarily to global optimum, only after a few iterations.

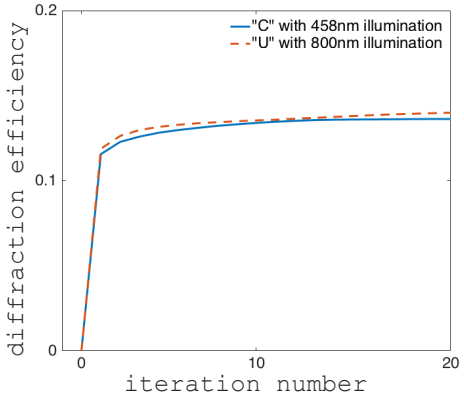

Figure 2.5 Convergence of diffraction efficiency for the iterative projection optimization algorithm.

Since the optimization algorithm starts from a random point, the design results would be slightly different each time the algorithm is executed. To find the more optimal solution, one can run the algorithm multiple times and select the best result. In general, the convergence to an acceptable solution does not depend on the starting point, namely if the algorithm converges the first time, it would converge when repeated. The factors affecting the convergence are the available degrees of freedom versus the task complexity, as discussed later in this thesis.

In angular multiplexing, we use a beam with wavelength of 532nm, and encode the letter "C" with incident angle of 0˚, and encode the letter "U" with incident angle of 15˚. The results are shown in Fig. 2.6.

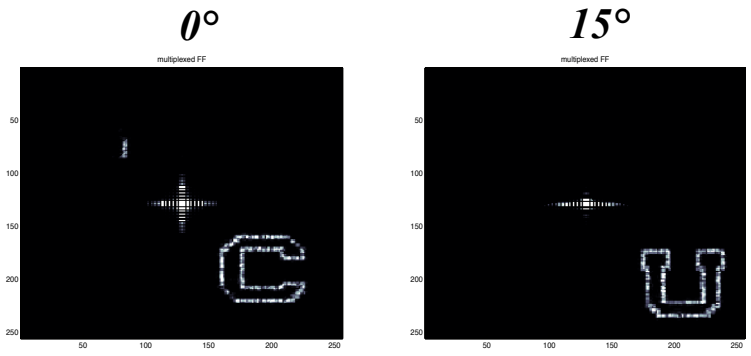

Figure 2.6 Simulation results for angular multiplexing. Left: reconstruction image with incident angle of 0˚. Right: reconstruction image with incident angle of 15˚.

We use the beam propagation method (BPM), which computes the propagation of a light beam in inhomogeneous media with diffraction and refreaction, to verify and assess the designs. BPM is a more accurate technique where there is no weak scattering assumption [62].

2.2.2 Rytov approximation

The first Rytov approximation is a method to implement volume scattering theory by representing the total field as a complex phase to approximate the scattered field. Compared to the first Born approximation, which assumes weak total scattering, the Rytov approximation requires weak incremental scattering. Thus, the Rytov approximation is more robust on thicker device sizes while rather limiting on smaller scale.

In 3D scattering theory, the total field for the Rytov approximation is represented as:

$$U_R(\vec{r}) = e^{\phi_R(\vec{r})} \tag{2.13}$$

where its phase is the sum of the incident phase and the scattered phase

$$\phi_R(\vec{r}) = \phi_i(\vec{r}) + \phi_B(\vec{r}) \tag{2.14}$$

It is related to the Born approximation as

$$\phi_R(\vec{r}) = \frac{U_B(\vec{r})}{U_i(\vec{r})} \tag{2.15}$$

The far-field wave scattered from the volume optics can be derived as

$$U_s(\vec{k}_s) = \exp\left[\frac{e^{jkr}}{r}\tilde{F}(\vec{k}_s - \vec{k}_i)/U_i(\vec{r})\right] \tag{2.16}$$

where $\tilde{F}$ is the scattering potential.

The above equation links the volume index modulation with the far-field wave that scattered from it. We use the relationship between these two domains and create an iterative projection optimization algorithm to design the 3D diffractive optics. The far-field scattered wave is defined by a particular sphere (Ewald sphere) within the

Fourier transform of the scattering potential. For frequency multiplexing, the Ewald sphere is a function of the index of refraction and the wavelength.

We implement frequency multiplexing using Rytov approximation. The design has feature size of 1×1×10μm. The voxel number is 128×128 in the transverse plane and 256 in the longitudinal direction. The letter "C" in the "CU" logo is projected for 458nm illumination, and the letter "U" for 800nm illumination. The simulation results from POCS algorithm under Rytov approximation are shown in Fig. 2.7.

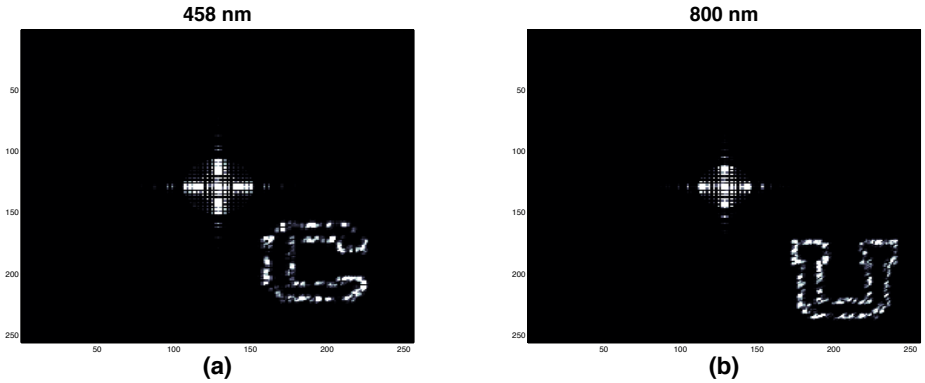

Figure 2.7 Far-field wave scattered from 3D diffractive optics using Rytov approximation under (a) 458nm illumination and (b) 800nm illumination.

The diffraction efficiency is measured with the BPM to be 0.24% and 0.11%, respectively. The index contrast is extremely low at 3×10^{-13}. Notice that the low index contrast is necessary to obtain the designed images using the Rytov approximation. Compared to the typical index contrast in the Born approximation (~10^{-3}), the Rytov approximation might be more restrictive with respect of the choice of index contrast.

2.3 Large space-bandwidth 3D diffractive optics

We use two factors that evaluate the performance of the volume optics: diffraction efficiency (DE) and relative mean square error (MSE). Both factors are calculated from BPM. The diffraction efficiency describes how much proportion of the total input intensity being diffracted towards the target area. In algorithm, the definition is:

$$DE = \frac{\iint \left| U_s\left(k_x, k_y, \infty\right)\right|^2 v_b\left(k_x, k_y\right) dk_x\, dk_y}{\iint \left| U_R\left(k_x, k_y, 0\right)\right|^2 dk_x\, dk_y} \tag{2.17}$$

where $U_s\left(k_x, k_y, \infty\right)$ is the scattered wave in the far-field, $v_b\left(k_x, k_y\right)$ is the target magnitude in binary form, and $U_R\left(k_x, k_y, 0\right)$ is the incident wave (or reconstruction wave) at the input plane. The relative mean square error is used to evaluate the uniformity in the target area and the background noise, which is defined as:

$$MSE = \frac{\iint \left| \left| U_s\left(k_x, k_y, \infty\right)\right|^2 - c v_b\left(k_x, k_y\right)\right|^2 dk_x\, dk_y \Big/ \iint \left[1 - v_b\left(k_x, k_y\right)\right] dk_x dk_y}{\iint \left| U_s\left(k_x, k_y, \infty\right) v_b\left(k_x, k_y\right)\right|^2 dk_x\, dk_y \Big/ \iint v_b\left(k_x, k_y\right) dk_x\, dk_y} \tag{2.18}$$

where c is the weighting factor to minimize MSE in the optimization and ensure the algorithm converge. The relative error is normalized by the number of pixels in both target area and the background such that the evaluation is independent of the designed pattern.

In frequency multiplexing case, the letters “C” and “U” are addressed with two normally incident plane waves with wavelength of 458nm and 532nm, respectively. Fig. 2.8 shows the diffraction efficiency and relative error changes as a function of index contrast and thickness.

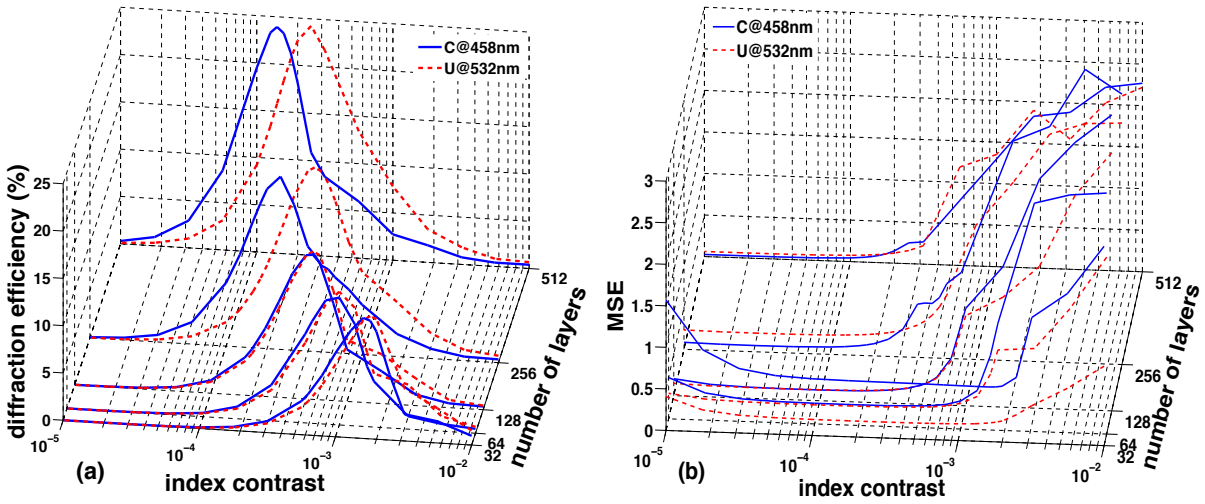

Figure 2.8 (a) Diffraction efficiency as a function of index contrast and thickness. The blue line is the diffraction efficiency of pattern C under 458nm illumination and the dashed red line is the diffraction efficiency of pattern U under 532nm illumination. (b) Relative mean square error as a function of index contrast and thickness. The blue line is the MSE of pattern C under 458nm illumination and the dashed red line is the MSE of pattern U under 532nm illumination.

The refractive index contrast changes in log scale from 10^{-2} to 10^{-5}, and the number of layers changes from 32 to 512 on the power of 2 to achieve fastest computing speed in FFT algorithm. As the volume optics become thicker, the diffraction efficiency for both patterns "C" and "U" are increasing, while the peaks are shifting towards the smaller index contrast end. The reason is that the design uses the first Born approximation which assumes weak total scattering. When the index contrast is too large, the weak scattering condition is not satisfied. On the other hand, if the index contrast were too small, the scattering effect would be too weak to diffract the incident beam into to the designed area. In addition, when the volume optics is small in thickness, the maximum diffraction efficiency occurs at larger index contrast. When the thickness increasing, the efficiency peaks move to smaller index contrast to keep the total scattering weak. The efficiency peak which corresponding to the shorter wavelength moves more because the index contrast affects more on

light with shorter wavelength. Thus, for the same thickness, the amount the two peaks separating depends on the wavelength spacing.

The MSE for all thicknesses are always large for larger index contrast where the weak scattering condition cannot be satisfied. In particular, the MSE at z=32 is high due to the crosstalk. As index contrast become smaller, the relative error decreased. For the same index contrast, the relative error is further decreased as number of layers increased because there are more layers to minimize the MSE. It goes up a little as index contrast approaching to 10^{-5}, because the scattering is too weak to produce any designed patterns.

Fig. 2.9 shows the intensity of the scattered wave in the far field with varying index contrast when the number of layers is 32, 128, and 512. All the images are scaled at the same. The weakly scattering assumption is invalid for index contrasts on the order of 0.01, resulting to speckle filed (Fig. 2.9d, h, i). The efficiency at z=128 reaches maximum of 15.29% when the index contrast of $10^{-3.25}$ (Fig. 2.9g), but its relative error is still high at 27.13%. As the index contrast lowers down to $10^{-3.85}$ (Fig. 2.9f), the error decreases to 13.54%, but the efficiency also decreases to 3.99%. Meanwhile, when we increase the number of layers to 512 (Fig. 2.9j), the maximum diffraction efficiency reaches to 23.93%, and the relative error is still as low as 7.06%. As the index contrast decreasing to 10^{-5}, we can hardly see any diffracted pattern in the far field (Fig. 2.9a,e) except a very week pattern "C" at z=512 (Fig. 2.9i). In particular, the error for z=32 is always high due to crosstalk (Fig. 2.9b-d). Figure 2m-o shows the calculated diffraction efficiency as a function of index contrast at z=32, 128, and 512. Thus, by increasing the number of layers, we can obtain higher diffraction efficiency with lower relative error by shifting the DE peak towards the smaller index contrast regime.

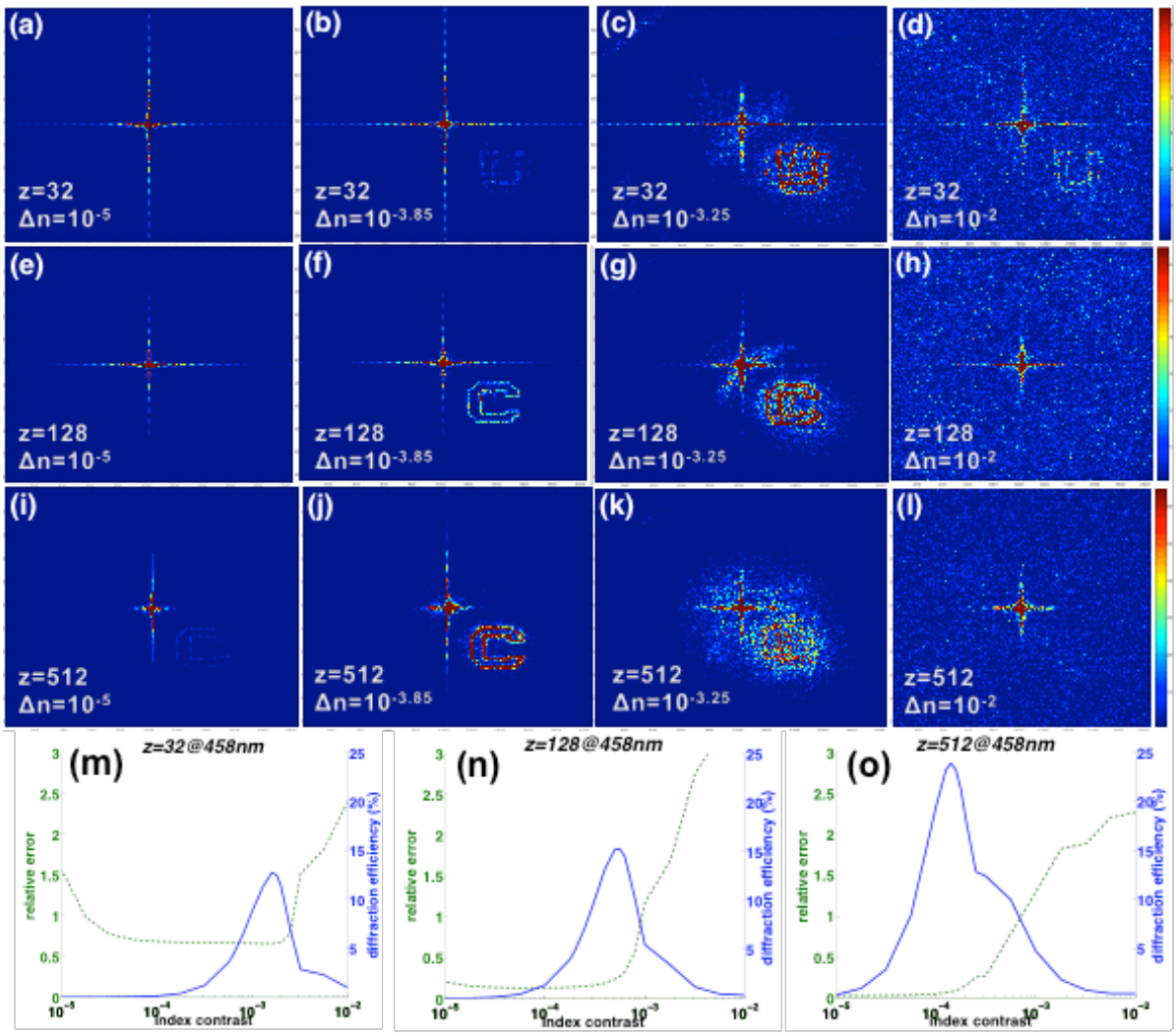

Figure 2.9 Far-field reconstructions modeled with a beam propagation method for a specific volume device with varying index contrasts. The number of layers are 32 (a)-(d), 128 (e)-(h), and 512 (i)-(l). The index contrasts are sampled at 10^{-2}, $10^{-3.25}$, $10^{-3.85}$, and 10^{-5}. All the far-field images are scaled at the same. The calculated diffraction efficiency and relative error are plotted for z=32 (m), 64 (n), and 512 (o).

2.4 Shift multiplexing 3D diffractive optics

Shift-multiplexing is a holographic technique first proposed by Psaltis *et al.* in 1995 [63]. They use a fan of plane waves as reference beam to interfere with the object

beam. As a result, multiplexing can be achieved by shifting the hologram with respect to the reference beam. In this work, we design the first computer-generated 3D diffractive optics to realize shift multiplexing.

The design schematic is shown in Fig. 2.10a. At the front focal plane of the lens, P1 and P2 are two point sources placed symmetrically off the axis. As a result, the device placed behind the lens is illuminated by two plane waves tilted with opposite angles. In 3D scattering theory under weak scattering conditions based on the first Born approximation, two corresponding Ewald spheres within the Fourier transform of the scattering potential define the far-field scattered wave. The two spheres in frequency domain are off axis by the same amount and the overlap area (Fig. 2.10b) can be used to create an iterative projection optimization algorithm to achieve multiplexing.

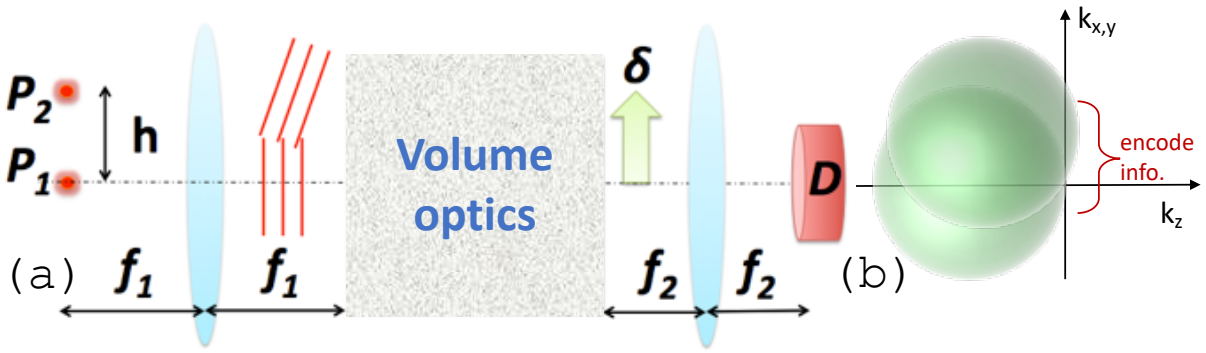

Figure 2.10 Schematic of shift multiplexing 3D diffractive optics: (a) real space representation, (b) in Fourier space representation.

The "CU" logo is implemented on the two Ewald spheres by parallel projections. Unlike angular multiplexing, the far-field image cannot be distinguished for each of the two incident waves (Figure 2.11a, 2.11b). However, the letter "U" in one of the Ewald spheres is set to be π radians out of phase from the other, whereas the letter "C" is in phase in the two Ewald spheres. Since the far-field pattern is the coherent superposition of the two scattered waves, when the device is at the center of

the optical axis, the letter "C" is obtained by constructive interference, whereas the letter "U" is eliminated by destructive interference (Figure 2.11c). As the device shifts normal to the optical axis, the induced phase change is different for the two incident waves (depending on the direction of the movement). When the phase change equals to π (or an odd number of π radians), the letter "C" will be destructively interfered and the letter "U" will appear by constructive interference (Figure 2.11d).

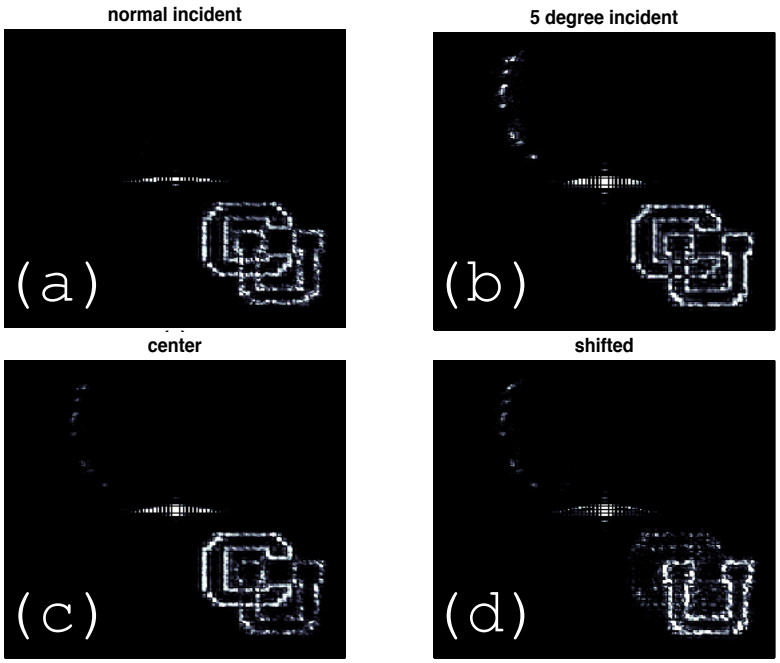

Figure 2.11 Simulation results for the far-field pattern with (a) normal incident only, (b) 5° incident only, (c) simultaneously incident without the device shifting, (d) simultaneously incident with the device shifting to induce a π phase change.

It should be noted that: 1. The amount of the shift of the device to induce a π phase change can be derived from simple geometrical considerations (not shown here). 2. The crosstalk between multiplexed images is due to the speckled nature of the far-field pattern. 3. The number of functions that can be multiplexed into the 3D diffractive optics is determined by the number of point source being considered.

2.5 Conclusion

We have shown numerically that large space-bandwidth frequency/angular multiplexed volume optics rapidly improve efficiency, pattern quality, as well as frequency/angular selectivity with thickness, while still satisfying the weakly scattering approximation. While the widely used coupled mode theory sufficiently predicts the diffraction efficiency as well as the tolerance for the deviation of the incident angle and/or wavelength used for reconstruction in periodic optically-recorded volume holograms, there is no such a theory that can analytically describe the performance of aperiodic computer-generated 3D diffractive optics. For accurate results, case-by-case studies are more appropriate. Although the general behavior can be derived from the related theories of volume holography, our numerical analysis provides a confirmation of the scaling laws as well as a design methodology. The fabrication of larger scale volume optics while challenging is within reach in the near future. This study should help guide the investigation in terms of the requirements and opportunities available with diffractive volume optics and help establish a roadmap towards implementation in application such as spectral imaging and quantum control.

Chapter 3

3D Diffractive Optics by Stratified-layer Approach

3.1 Introduction

In this chapter, we present an alternative approach to design and implement 3D diffractive optics, namely stratified-layer approach. Instead of the full volume design demonstrated in the previous chapter, the 3D structure is represented by multiple cascaded diffractive optical elements which are spatially separated by short distances in optically homogenous medium.

Diffractive optical elements (DOEs) and computer-generated holograms (CGHs) are 2D optical elements capable of modulating light fields in essentially arbitrary fashion within the fundamental limits imposed by the wave nature of light [11,13]. They are superior to optically recorded holograms in terms of customized wavefront generation from arbitrary wavefront illumination, which is due to the degrees of freedom offered by individually addressable pixels and possible optimization for a target metric. As a result, remarkable advances have been achieved in application fields including optical tweezers [64,65], beam shaping [18,19], holographic display [20,66], novel microscopies [67–69], optogenetics excitation [30,37,38,70], and femtosecond laser micromachining [71,72].

Previous work shows that additional degrees of freedom can be acquired by extending the diffractive optics from 2D (thin) to 3D (thick). Accordingly, system performance metrics are improved such as enhanced diffraction efficiency [73], better angular or frequency selectivity [74], and capability to generate space variant functions [75,76]. To fully take advantage of the ever-increasing computational power, procedures have been developed for the design and implementation of 3D diffractive optics, mainly through the following two approaches. One is by implementing full volume design with 3D scattering theory and projection-onto-convex-sets (POCS) algorithm, as demonstrated in the previous chapter. The other is by cascading of multiple 2D diffractive optics. The design is fulfilled with a distribution-on-layers algorithm, and experiments demonstrate that the diffraction efficiency is increased and two diffraction patterns are angularly multiplexed.

Here, we first introduce an approach for designing 3D diffractive optics with a stratified-layer model. We then design 3D diffractive optics composed of multiple diffractive layers using a POCS algorithm, which is a more general version of the well-known Gerchberg-Saxton iterative optimization algorithm. We theoretically investigate multilayer devices in terms of diffraction efficiency and spatial/spectral multiplexing properties.

3.2 Stratified-layer 3D Diffractive Optics Theory

3.2.1 Physical Model

Stratified-layer 3D diffractive optics consists of multiple thin layer DOEs, which are spatially separated and evenly distributed in optically homogenous

medium. As light propagates through the 3D optics, the amplitude and phase are modulated by each DOE and diffraction occurs in the intermediate homogeneous regions (Fig. 3.1). This model also applies to volume optics that continuously reshape light on propagation by considering infinitely thin homogenous layers [16]. If we consider only one single layer, it exhibits Raman-Nath characteristics because the thickness is infinitesimal. However, the 3D diffractive optics altogether shows Bragg-like behavior as a result of the diffraction in multiple DOEs and buffer layers. This property can be used for multiplexing, both in frequency and angular domains and to generate space variant systems.

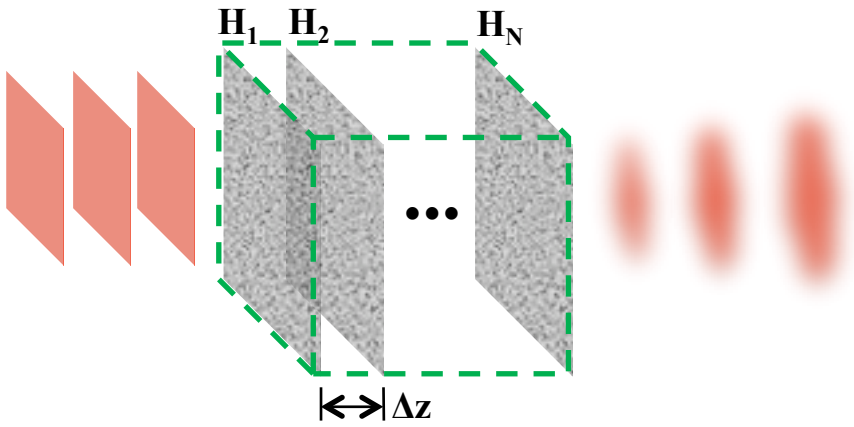

Figurer 3.1 Schematic illustration of a stratified layered 3D diffractive optics.

For simplicity, we consider the scalar approximation to be valid under the assumption that the feature size is large relative to the wavelength of operation. The complex transmittance function of each thin DOE can be expressed as

$$h_k(x,y) = |h_k(x,y)|exp[j\phi_k(x,y)] \tag{3.1}$$

where k is the layer number. To achieve maximum efficiency, we consider pure phase modulation, with the amplitude term always unity. Under the thin-element approximation, the effect of a single DOE layer on the complex amplitude is

$$E(x,y,z_k^+) = h_k(x,y)E(x,y,z_k^-) \tag{3.2}$$

where z_k^- and z_k^+ indicate the planes immediately before and after the kth layer DOE, respectively. The wave-field evolution between adjacent DOEs layers can be described by angular spectrum propagation in free space. Therefore, the relation between the complex amplitude after the k-th layer and the wave-field before the k+1-th layer can be expressed as

$$E(x,y,z_{k+1}^-) = \mathcal{F}^{-1}\left\{e^{-j\sqrt{k_0^2-k_x^2-k_y^2}\cdot\Delta z}\cdot\mathcal{F}[E(x,y,z_k^+)]\right\} \tag{3.3}$$

where λ is the design wavelength, Δz is the layer separation. If a Fourier lens is placed one focal length after the last DOE layer, the complex amplitude at the reconstruction plane satisfies

$$R(k_x,k_y,\infty) = \mathcal{F}\{E(x,y,z_N^+)\} \tag{3.4}$$

Hence, the relation between the 3D diffractive optics and the far-field reconstruction is obtained. The propagation process is also numerically reversible, namely waves can be back-propagated from the target $R(k_x,k_y,\infty)$.

3.2.2 Design algorithm

While different design strategies can be anticipated, here we design the multiplexing 3D diffractive optics using a POCS algorithm with a distribution-on-layers method. To calculate a 3D diffractive optics layer by layer, we first start by setting all of them to have a random phase and unit amplitude. Then we calculate the transmission function of the layer r by first calculating the wave-field before the layer r, $E(x,y,z_r^-)$, $r \in [1,\cdots,N]$. This process starts from the input $E(x,y,z_1^-)$ and

follows equations (3.1)-(3.4). For backward propagation, we start with the desired reconstruction field $\tilde{R}(k_x, k_y, \infty)$, and use the inverse propagation (conjugate of equations (1)-(4)) to calculate the wave-field after the rth layer, $E(x, y, z_r^+)$. The transfer function for layer r is then obtained as follows

$$\tilde{h}_r(x, y) = \frac{E(x,y,z_r^+)}{E(x,y,z_r^-)} \tag{3.5}$$

$h_r(x, y)$ is a complex function, so we extract its phase by projecting onto the set of phase-only functions,

$$h_r(x, y) = arg\{\tilde{h}_r(x, y)\} \tag{3.6}$$

If we perform forward propagation through the 3D diffractive optics, it is mostly likely that the field on the reconstruction plane will no longer match the original target. Hence we employ a generalized projection algorithm, which iterates between each layer and the reconstruction plane, applying equations (3.1)-(3.4) and their conjugate forms. The algorithm keeps running until the deviation from the reconstruction plane and target is acceptable.

This process provides the transmission function for one layer of 3D diffractive optics. The remaining layers are calculated following the same process. The layers can be calculated in sequential form, random fashion, or in parallel. As a result, the encoded information is evenly distributed among all the layers. This can significantly increase the design degrees of freedom and coding capacity of the 3D diffractive optics.

3.2.3 Design Algorithm for Multiplexing

Volumetric optics enables methods of multiplexing which can be implemented by design in 3D diffractive optics. Compared to 2D DOEs, the 3D counterparts exhibit strong angular or wavelength selectivity, i.e. different uncorrelated outputs can be achieved with different inputs in a single 3D diffractive optics. For instance, one can change the initial condition $E_p(x, y, z_1^-)$ to reconstruct different predefined images $R_p(k_x, k_y, \infty)$, respectively. The input can be addressed via wavelength, angle of incidence, or phase pattern.

$$E_p(x, y, z_1^-) = \begin{cases} Aexp\left\{j\frac{2\pi}{\lambda}xsin\varphi_p\right\}, angular\ muliplexing \\ Aexp\left\{j\frac{2\pi}{\lambda_p}\right\}, \quad frequency\ multiplexing \\ Aexp\{j\phi_p(x, y)\}, \quad phase\ multiplexing \end{cases}, p = 1,2, \dots, K \tag{3.7}$$

where K is the total number of pages to be multiplexed. For each input and its corresponding reconstruction, the transmission function of every single layer is calculated by the same procedure described above. Finally, to take all the multiplexed information into account, we apply parallel projections as follows

$$h_r(x, y) = exp\left\{jc_r\frac{1}{K}\sum_{p=1}^{k}\tilde{h}_{r,p}(x, y)\right\} \tag{3.8}$$

where c_r is a coefficient to facilitate algorithm convergence. Every layer of the 3D diffractive optics is calculated in this fashion, thus concluding one iteration. The generalized projection algorithm runs until a satisfactory result is reached. The overall flow chart of the algorithm is summarized in Fig. 3.2.

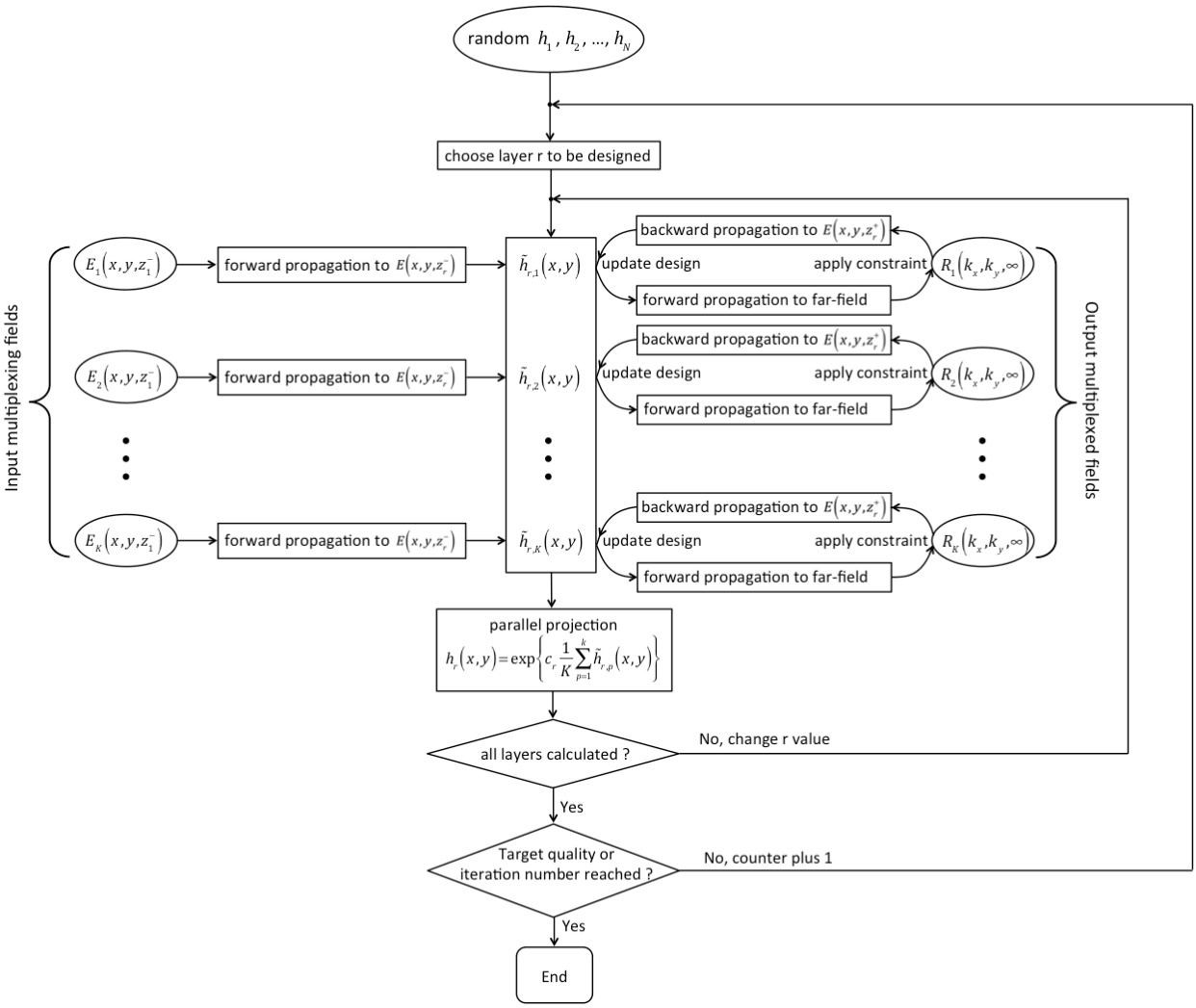

Figure 3.2 Flowchart of projection onto constraint sets with a distribution-on-layers algorithm. *h1*, *h2*, …, h_N are layers to be designed, and are set random prior to the computation. $R_1(k_x,k_y,\infty)$, $R_2(k_x,k_y,\infty)$, …, $R_K(k_x,k_y,\infty)$ are user-defined output multiplexed fields with the corresponding input multiplexing fields $E_1(x,y,z_1^-)$, $E_2(x,y,z_1^-)$, …, $E_K(x,y,z_1^-)$. The input field and output field are forward and backward propagated respectively to the field before and after the layer to be designed. The modulation function is updated during several iterations for each multiplexing pair and for each layer in the 3D diffractive optics. The process is followed by a parallel projection to ensure all the information is being encrypted and evenly distributed among all the *N* layers. The optimization algorithm ends when the target quality or the preset iteration number is reached.

3.3 Design Results

To illustrate the principle, we present the design of a two-layer 3D diffractive optics. The pixel number in each layer is 128×128, with pixel size of 8μm×8μm. The layer separation is set to be Δz=486μm. Those parameters are chosen to adapt to the SLM used in the experiment, as shown in the next chapter.

For angular multiplexing, we use the letter "C" and "U" from the CU logo (Fig. 3.3a) as the target images for incident angles at 7° and 10°, respectively. The wavelength of the incident beam is 633nm. The reconstructed image is shown in Fig. 3.3c. For frequency multiplexing, we use the same two patterns with the incident angle fixed at 7°, and the wavelength of illumination 633nm for "C" and 532nm for "U". The reconstructed image is shown in Fig. 3.3e. The phase patterns for the above two cases are shown in Fig. 3.3b and 3.3d, respectively.

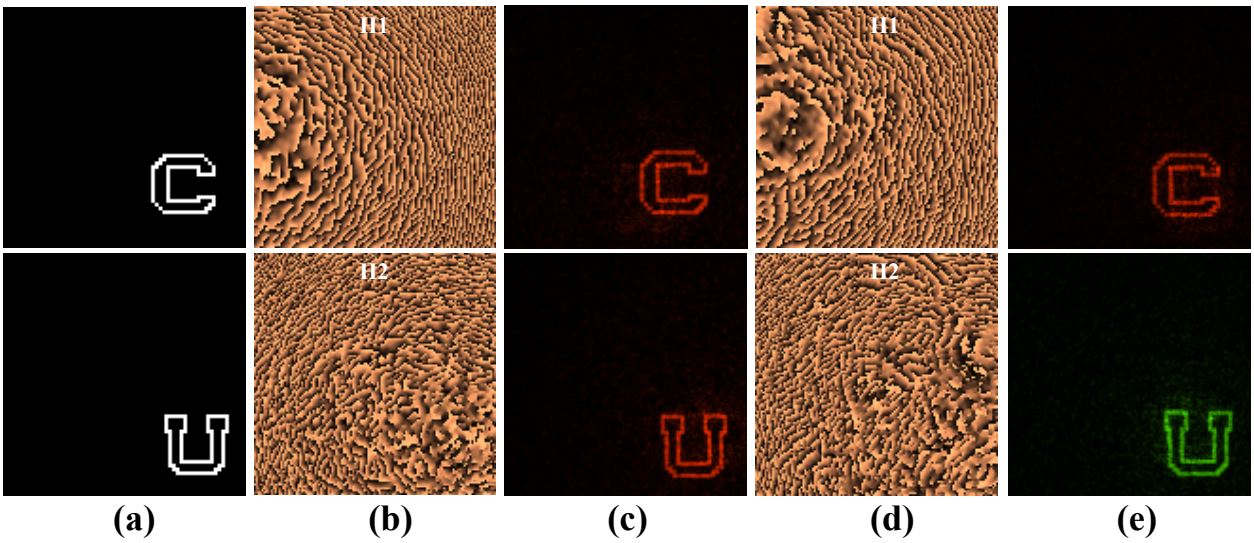

Figure 3.3 Simulation results for multiplexing 3D diffractive optics. (a) The letters "C" and "U" in the CU logo are the target images. (b) Phase patterns designed for angular multiplexing. (c) Reconstructed images with incident angle at 7° and 10° showing angular multiplexing. (d) Phase patterns designed for frequency multiplexing. (e) Reconstructed images with 633nm and 532nm illumination showing frequency multiplexing.

3.4 System performance

We use diffraction efficiency (DE) and relative error (Err) to evaluate the performance of the designs. The diffraction efficiency is defined as the ratio of the intensity in the target area to the intensity of the input beam, and can be calculated by the following equation:

$$DE = \frac{\iint \left| U_R\left(k_x, k_y, \infty\right)\right|^2 v_b\left(k_x, k_y\right) \mathrm{d}k_x \mathrm{d}k_y}{\iint \left| E\left(x, y, z_1^-\right)\right|^2 \mathrm{d}x\mathrm{d}y} \tag{3.9}$$

where U_R is the reconstructed field in wave-vector coordinates, and $v_b\left(k_x, k_y\right)$ is the target region in binary form, i.e. the target domain. The relative error is used to measure the quality of the reconstruction relative to the total light intensity directed on target:

$$Err = \frac{\iint \left| \left| U_R\left(k_x, k_y, \infty\right)\right|^2 - c_i v_b\left(k_x, k_y\right)\right|^2 \mathrm{d}k_x \mathrm{d}k_y}{\iint \left| U_R\left(k_x, k_y, \infty\right)\right|^2 v_b\left(k_x, k_y\right) \mathrm{d}k_x \mathrm{d}k_y} \tag{3.10}$$

where c_i is a weighting factor that changes with iteration number i to ensure the algorithm converges.

The diffraction efficiencies for C and U in the angular multiplexing example are 54.2% and 59.1%, respectively, while the relative errors are 0.13 and 0.10, respectively. For frequency multiplexing, the efficiencies are 62.5% and 65.5%, whereas the relative errors are 0.16 and 0.14.

Next, we investigate the relations between diffraction efficiency and parameters such as number of pixels, number of layers, and layer separation. We use the scheme for frequency multiplexing. First, we expand the number of layers to 16 at the increment of 2 with 128×128 pixels in each layer. The diffraction efficiency for

"C" under 633nm illumination and "U" under 532nm illumination are plotted in Fig. 3. 4a. Then we with two layers, we change the number of pixels to 1024×1024, at the increment of 128×128. The diffraction efficiency for "C" under 633nm illumination and "U" under 532nm illumination are plotted in Fig. 3. 4b. Both the number of pixels and number of layers are positively related to the degrees of freedom of the device. Therefore, with all other parameters unchanged, the diffraction efficiency can be enhanced by increasing the number of pixels or the number of layers. A longer computation time is required, which at some point can make the problem intractable. For example, the calculation of 16 layers with 2048×2048 pixels is beyond the computational power of a 2.8GHz quad-core CPU with 12Gb memory and could be tackled with parallel computation.

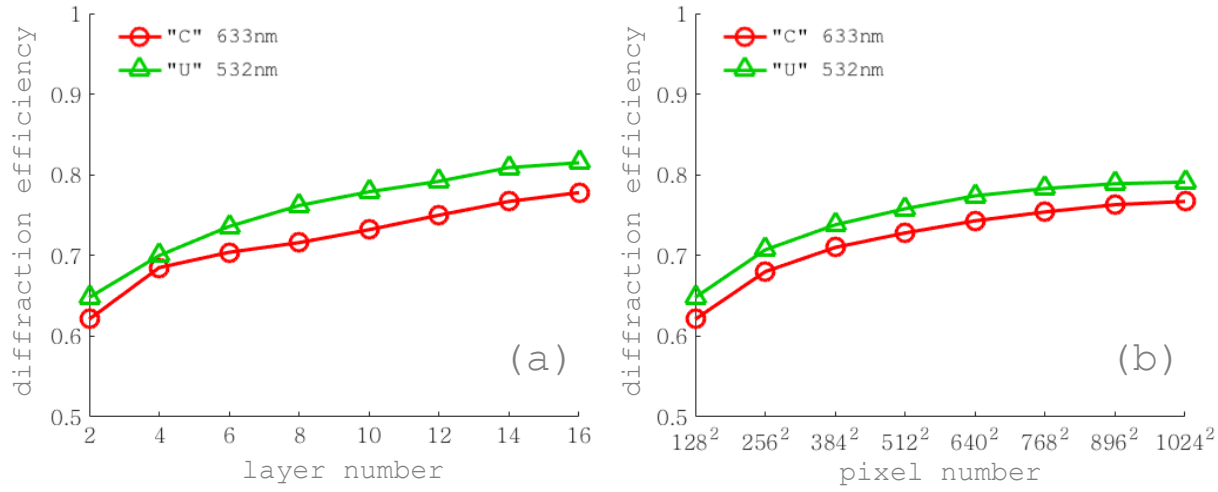

Figure 3.4 Diffraction efficiency as functions of layer number and pixel number in frequency multiplexing with two functions. (a) Diffraction efficiency as a function of layer number. (b) Diffraction efficiency as a function of pixel number.

Second, we study the effect of pixel and layer number on wavelength selectivity. The results are shown in Fig. 3.5. We start with 2 layers of 128×128 pixels, and reconstruct the 3D diffractive optics with wavelength from 500nm to 660nm. The

diffraction efficiency of “C” and “U” are recorded respectively. Then we use 4 layers with 1024×1024 pixels and record the data in the same way. We observe that both the diffraction efficiency increases and the wavelength selectivity improves with additional degrees of freedom.

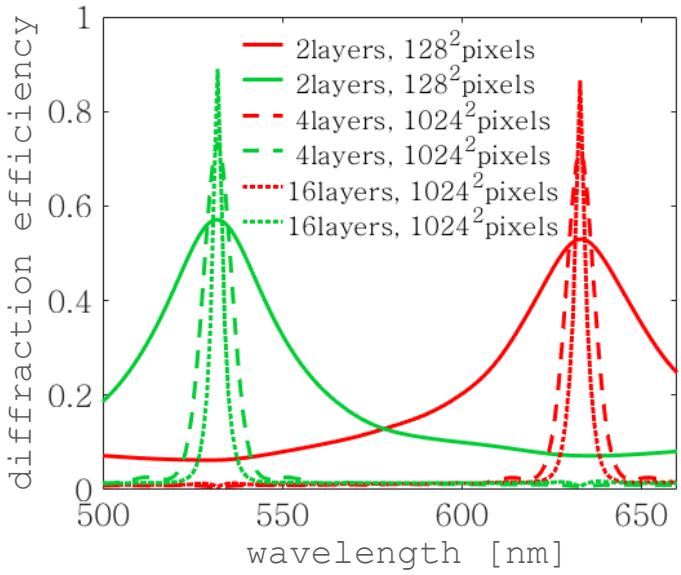

Figure 3.5 Wavelength selectivity for the letters “C” and “U” as a function of the number of pixels and the number of layers.

Third, we analyze the diffraction efficiency as a function of layer separation, shown in Fig. 3.6. We change layer separation from 1μm to 1mm, for two-layer elements of 128×128 pixels. We observe little effect of layer separation on diffraction efficiency.

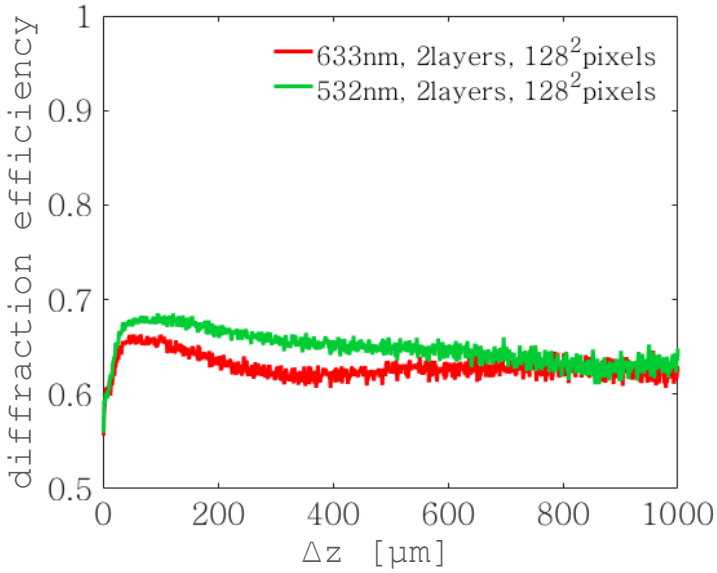

Figure 3.6 Diffraction efficiency of the letters “C” and “U” as a function of layer separation.

Fourth, we study the effect of layer separation on wavelength selectivity. The layer separation is selected to be 50μm, 486μm (used in the design and experiment), and 1000μm for two layers of 128×128 pixels. The wavelength in the reconstruction beam is changed from 500nm to 660nm in all three cases, as shown in Fig. 3.7. We observe a moderate increase in selectivity as the effective thickness of the element increases. The effect can be explained by the fact that the buffer layer is where the propagation effect of diffraction occurs so a wavelength deviation of the input leads to a larger effect for longer distances. Similar tendencies are observed for angular multiplexing.

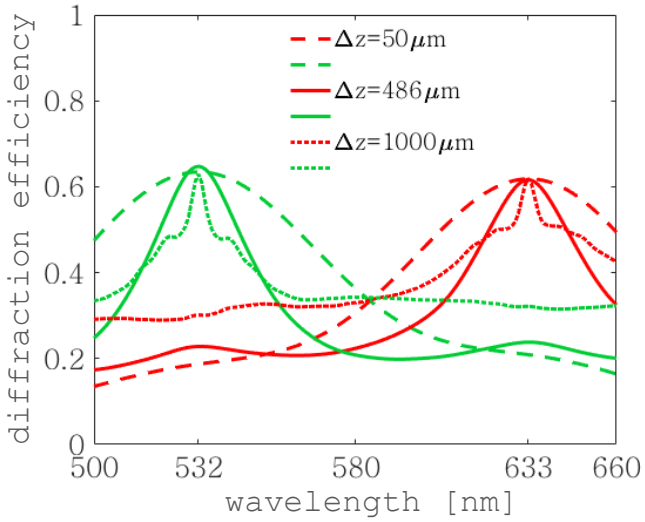

Figure 3.7 Wavelength selectivity of the letter "C" and "U" at layer separation of 50μm, 486μm, and 1000μm.

3.5 System limits

First, we show the results of a design for a 16-layer 3D diffractive optics using the procedure described in section 3.2. Frequency multiplexing of 2 functions, namely the letters "C" and "U" from the "CU" logo, is implemented with 633nm and 532nm illumination, respectively. Fig. 3.8 shows the designed phase patterns, which improves the diffraction efficiency of the two far-field images to reach 77.4% and 81.8% from 62.1% and 65.4%.

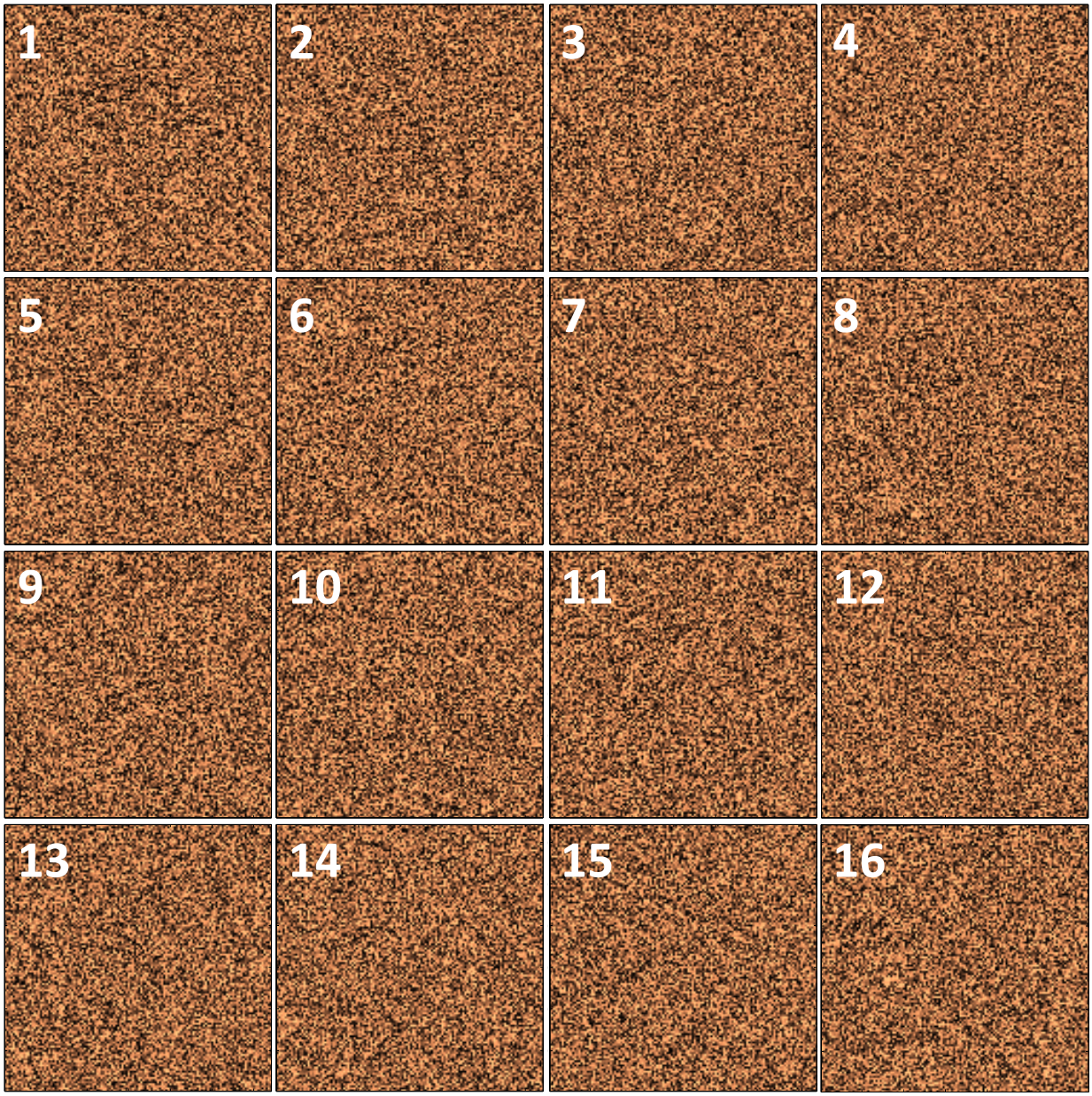

Figure 3.8 Phase patterns of 3D diffractive optics with 16 layers. The device is designed to multiplex "C" and "U" in frequency. The pixel number in each layer is 128×128, and the phase values are 8 bits.

Last, it is interesting to analyze the limit of angular or frequency multiplexing in layered 3D diffractive optics, namely the smallest angle or wavelength interval between multiplexed reconstructions that avoids information crosstalk. While the selectivity plots of Figs. 3.5 provide a sense of the multiplexing performance, a more

specific metric consists of the reconstruction error as a function of the angular/frequency separation of the different information channels. Accordingly, we design 3D diffractive optics for angular multiplexing with changing angular intervals and plot the normalized reconstruction error as a function of the angular separation. For demonstration, we use 4 layers with 128×128 pixels on each. In angular multiplexing, we vary the angular interval in angular multiplexing, from 0.02° to 1°, and plot the normalized error as a function of angular interval. Fig. 3.9a shows the plot and reconstructed images, from which we conclude the smallest angular interval to avoid severe crosstalk is ~0.2°. Similarly, for frequency multiplexing, we use the same parameters for the 3D diffractive optics, and encode "C" at 633nm while changing the encoding wavelength for "U" from 632nm to 583nm. The normalized error and reconstructed images for designs at selected wavelength intervals are shown in Fig. 3.9b. We conclude the smallest wavelength multiplexing interval to avoid severe crosstalk, with these same parameters, is ~20nm. The multiplexing interval in wavelength and angle are limited by the degrees of freedom available in the device. Thus, they can be improved by increasing the layer number or pixel number in each layer. With that, more functions can be encoded in the 3D diffractive optics.

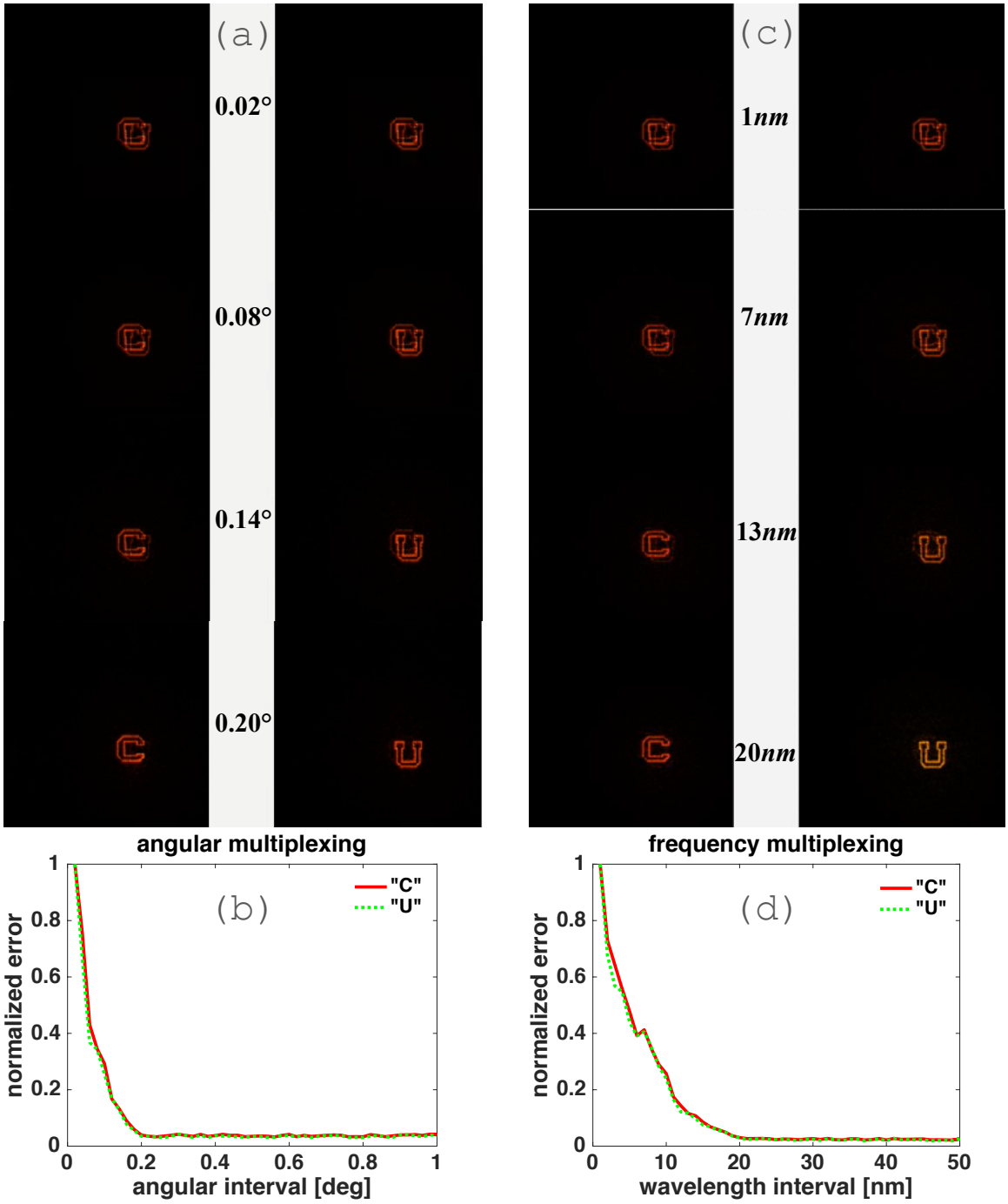

Figure 3.9 Crosstalk measurement for angular multiplexing and frequency multiplexing. (a) The reconstructed images are displayed for designs at selected angle intervals. (b) Normalized error in angular multiplexing as a function of angular interval between the two reconstructions. (c) The reconstructed images are displayed for designs at selected wavelength intervals. (d) Normalized error in wavelength multiplexing as a function of wavelength interval between the two reconstructions.

3.6 Conclusion

We proposed a stratified-layers approach to design 3D diffractive optics. Angular and frequency multiplexing is achieved, and the fundamental opportunities and limitations are analyzed.

3D diffractive optics not only enhance the design degrees of freedom and coding capacity, but also enable properties unique to volume (thick) holograms, such as having only one diffraction order, improved efficiency with lower crosstalk, and capability for angular and frequency multiplexing, as demonstrated numerically and experimentally. It is worth pointing out that our approach is different from the traditional use of multiple planar diffractive elements to encode amplitude and phase, but rather a carefully designed arrangement of diffraction, imaging, and propagation that provides the functionality of a volumetric structure, namely space variance, multiplexing in wavelength and spatially, and large information capacity, among others.

The 3D diffractive optics design implements a POCS algorithm with distribution-on-layers to spread information among multiple thin diffractive optical elements. The approach further contributes to the field of inverse problems by solving the nonlinear inverse problem of finding the 3D diffractive optics that achieves a given task without the need to assume weak scattering structures. From a fundamental point of view, the design of 3D diffractive structures mitigates the dimensionality mismatch inherent to the control of multiple dimensions of light fields (spatial, spectral, temporal, and coherence function) beyond what is possible with 2D devices.

Chapter 4

Dynamic Implementation of 3D Diffractive Optics on a Spatial Light Modulator

4.1 Introduction

In this chapter, we introduce an approach for 2D implementation of 3D diffractive optics that enables dynamic control of high volumetric bandwidth elements. We design multiple phase-only modulation layers using a projection-onto-constraint sets algorithm with distribution-on-layers optimization. The design is implemented on a single liquid crystal based spatial light modulator (SLM), which enables dynamic and multi-level phase modulation. The SLM is spatially divided to accommodate different layers, and each layer is diffraction propagated using a concave mirror. We theoretically and experimentally investigate multilayer devices in terms of diffraction efficiency and spatial/spectral multiplexing properties.

Cascaded 2D diffractive optics have been demonstrated with experiments showing improved diffraction efficiency, angular multiplexing of two diffraction patterns [14], and fiber mode multiplexing [77]. Full volume designs have been implemented applying 3D scattering theory and projection onto constraint sets

(POCS) algorithms. Experiments have demonstrated both angular and frequency multiplexing [16]. However, 3D lithographic methods still limit the implementation to relatively low space-bandwidth devices and mostly to binary form, which restrict the design degrees of freedom and performance. Further, once the devices are fabricated, no dynamic changes are allowed due to the permanently induced material modification. Volumetric spatial light modulators (VSLM) with capability to modulate micro-voxels would provide a unique opportunity to this field. Unfortunately, to the best of our knowledge, a viable device has never been conceived or demonstrated.

Liquid crystal based SLMs are dynamic 2D wavefront shaping devices with high efficiency and high resolution. They allow switching rates of hundreds of hertz enabling dynamic 2D diffractive optics. However, the phase patterns displayed on SLMs are two-dimensional; hence, they only work optimally for a certain wavelength due to diffractive and material dispersion. A simple solution for display applications is to use spatially or time multiplexed 2D phase patterns on a single or multiple SLM, with each phase pattern corresponding to a different color [78–80]. While these methods are appropriate for display, they cannot implement the space or frequency variant functionality of volume diffractive optics.

Previous approaches aimed at multi-wavelength operation of 2D diffractive optics are based on multiple-order diffractive optics, namely devices implementing phase delays beyond 2π. They are based on surface-relief fabrication or liquid-crystal SLM [81–85]. However, these methods are capable of a limited spectral bandwidth selectivity, enabling independent control of two or at most three-color bands, making them inappropriate to control a large number of spectral bands as possible with volumetric optics. Latest investigation of diffractive optics incorporating sub-wavelength structures, also called meta-surface optics, provides interesting opportunities for multifunctional devices [44,86–88].

4.2 2D implementation of 3D diffractive optics

3D diffractive optics consists of, or can be represented by, multiple thin, cascaded DOEs, which are spatially separated by short distances, in optically homogenous medium. As light propagates through the 3D optics, the amplitude and phase are modulated by each DOE and diffraction occurs in the intermediate homogeneous regions (Fig. 4.1a).

Therefore, to emulate a 3D diffractive optical element, we consider stratified layers separated by a short distance Δz. The transformation by diffraction between layers, namely free-space propagation through a distance Δz is equivalent to imaging with unit magnification followed by free-space propagation of Δz (Fig. 4.1b). This equivalence enables physical separation among layers while achieving the same functional form as a 3D optical element. Hence, existing planar (2D) diffractive technology can be implemented to generate 3D diffractive optics functionality.

Furthermore, this approach is also amenable to implementation in folded systems, for instance by substituting the lens by one or several concave spherical mirrors. As a result, the 3D design can be implemented on a single 2D plane (Fig. 4.1c), enabling display on a single phase-only DOE or a liquid-crystal SLM, which is spatially multiplexed to display the different layers.

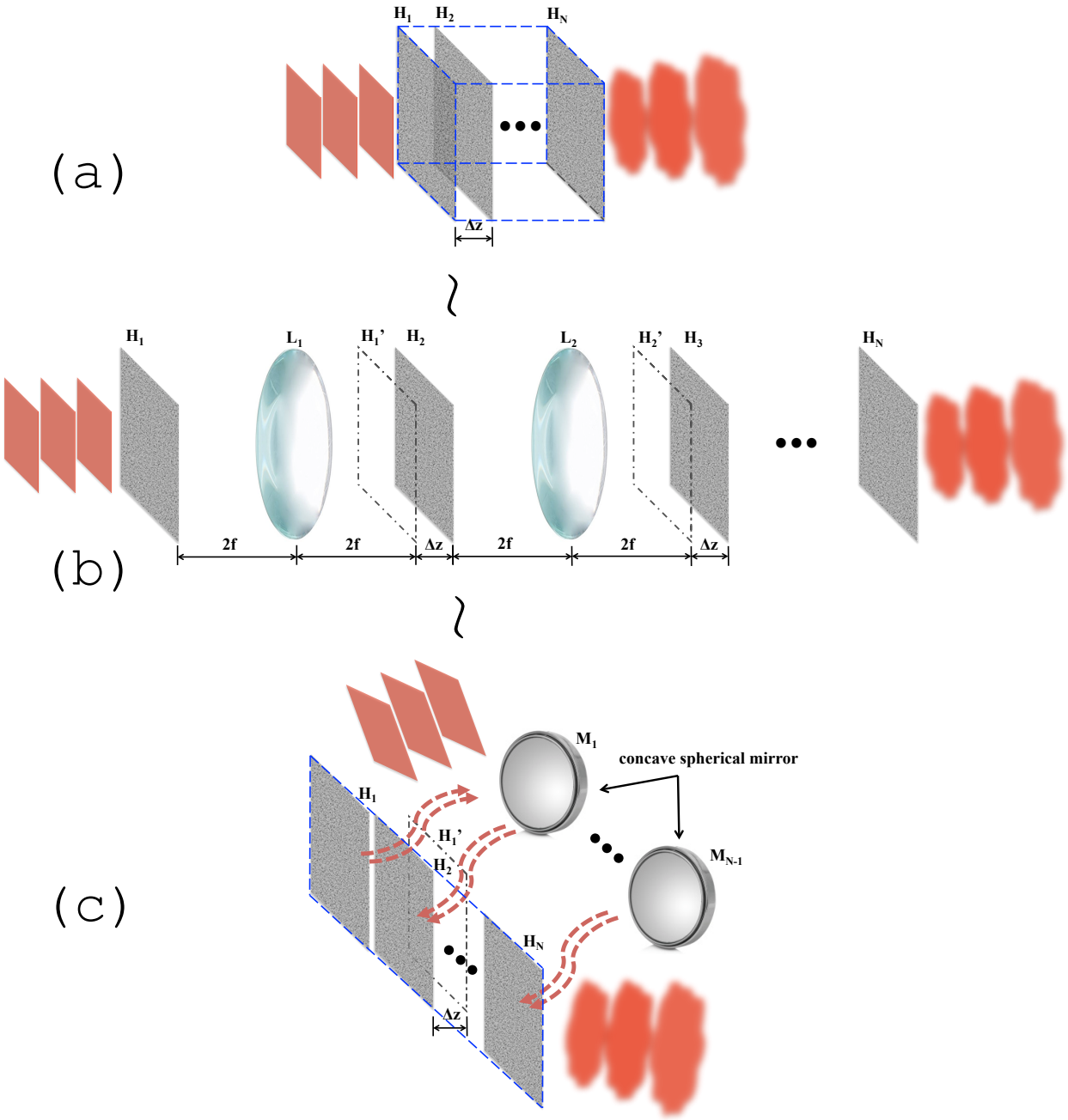

Figurer 4.1 3D diffractive optics implementation via 2D optics. (a) Decomposition in stratified layers. (b) Equivalent cascaded system using imaging optics. (c) 3D diffractive optics folded implementation on single spatially multiplexed DOE (e.g. SLM) with spherical mirrors.

The computation of wave propagation within the stratified-layer 3D diffractive optics is described in Chapter 3. In particular, eq. (3.1)-(3.4) apply for forward

propagation, where their conjugate forms apply for backward propagation. It should be noticed that the wave-field picks up a quadratic phase term after a single lens or upon reflection from the spherical mirror. Therefore, there is a difference in the relation between the complex amplitude after the kth layer and the wave-field before the k+1th layer. In this case, it can be expressed as

$$E(x,y,z_{k+1}^{-}) = \mathcal{F}^{-1}\left\{e^{-j\sqrt{k_0^2-k_x^2-k_y^2}\cdot\Delta z}\cdot\mathcal{F}\left[E(x,y,z_k^{+})\cdot e^{j\frac{2\pi}{\lambda}(x^2+y^2)\cdot 2f}\right]\right\} \tag{4.1}$$

where λ is the design wavelength, Δz is the layer separation, and f is the focal length of the lens or spherical mirror.

4.3 Experimental results

4.3.1 Experiment setup

The experimental setup is shown in Fig. 4.2. We use a supercontinuum fiber laser (Fianium FemtoPower 1060) to generate a tunable source covering spectral bandwidth from below 400nm to beyond 900nm. The beam is sent to a computer-controlled acousto-optic tunable filter (AOTF) to provide a narrowband output with bandwidth of 2nm to 4nm at the desired wavelength. The AOTF features a fast switching mode with less than 5 μs rise time, which is sufficient for real-time applications such as generating real time color holographic projection. A linear polarizer is used to ensure the polarization of the incident beam is parallel to the orientation of the liquid crystal on the SLM panel (horizontal in our case), even though the output from the AOTF is already linearly polarized at that direction. We

include a neutral density (ND) filter after the polarizer to adjust the intensity of the laser beam. To improve the uniformity of the beam profile, a spatial filter system is employed consisting of a microscope objective (20×, 0.25NA) and a pinhole (50μm diameter). A doublet achromatic lens (L1) is used to collimate the beam while avoiding chromatic aberrations. An iris adjusts the beam diameter for optimal illumination on the active area of the SLM (Holoeye HEO1080P, with 1920×1080 pixels and 8μm pixel pitch).

If we divide the SLM into two parts side by side, the largest beam size allowed could be up to 4.32mm, and the pixel number of each single layer could be up to 540×540. If more layers are designed, and a single SLM is still used, both the beam size and the design dimension will have to shrink. Accordingly, the beam size is adjusted to 1.5mm and 3mm for each case. To control the incident angle, a flat mirror (M3) mounted on a rotation stage is used. It diverts the beam at 7° respect to the normal of the SLM panel. In angular multiplexing, a flipped mirror (M4) is inserted at the proper position along the beam path to obtain an incident angle of 10°. The laser beam illumination setup is indicated by the orange square in Fig. 4.2.

In order to match the beam profile while suppressing the background of light unaffected by the SLM, the designed layers are first padded with tilted blazed gratings, as shown in Fig. 4.3. Then they are implemented on a single high-resolution SLM, which is horizontally divided in two sections. The beam incident on the right part (far side with respect to M3) displays the first layer. It is then imaged by a concave spherical mirror (SM) with focal length of 200mm at a small distance in front of the left section (near side with respect to M3), where the second layer is displayed. Based on these parameters, the distance between layers turns out to be 486μm.

Since the incident angle is small, we use a wedge with 10° beam deviation (Thorlabs PS814) to separate the output from the input. An achromatic doublet lens (L2) with focal length of 300mm is followed to yield a Fourier plane (equivalent to the

far field of the output form the diffractive optics) where a camera is installed to capture the reconstructed image. Considering the beam is diverging after incidence on the SLM for the second time, the Fourier plane is located farther than one focal length after the lens.

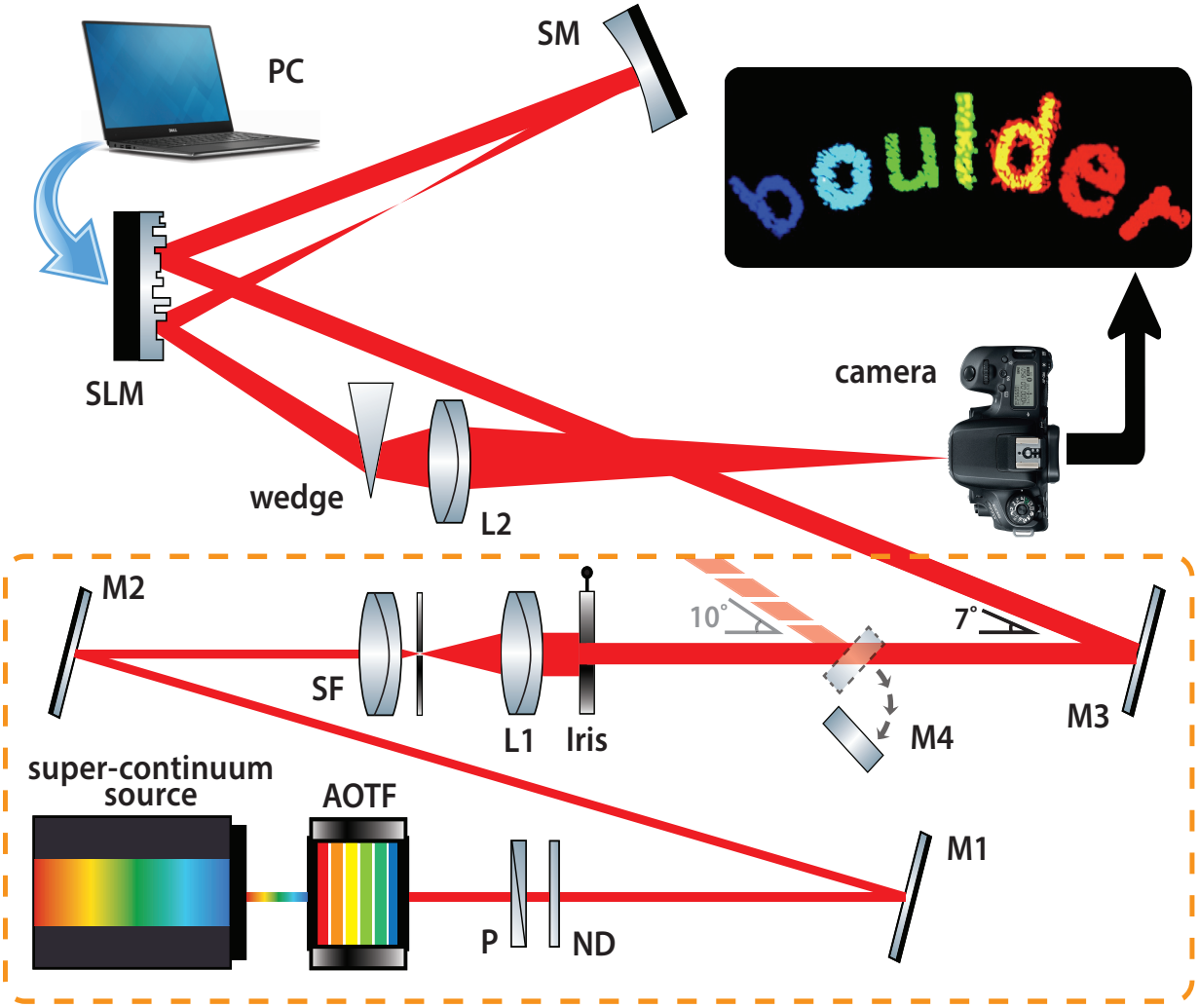

Figure 4.2 Experimental setup for 2D implementation and characterization of a dynamic 3D diffractive optics. A super-continuum source together with an acousto-optic tunable filter (AOTF) provide narrowband laser output in the visible spectrum. The designed layers are implemented on a single high-resolution liquid crystal SLM, which is spatially divided into two sections. The first layer is imaged at a small distance in front of the second layer, with an imaging system formed by a concave spherical mirror with focal length of 200mm. A color CMOS sensor is placed on the reconstruction plane after a Fourier lens to record the image.

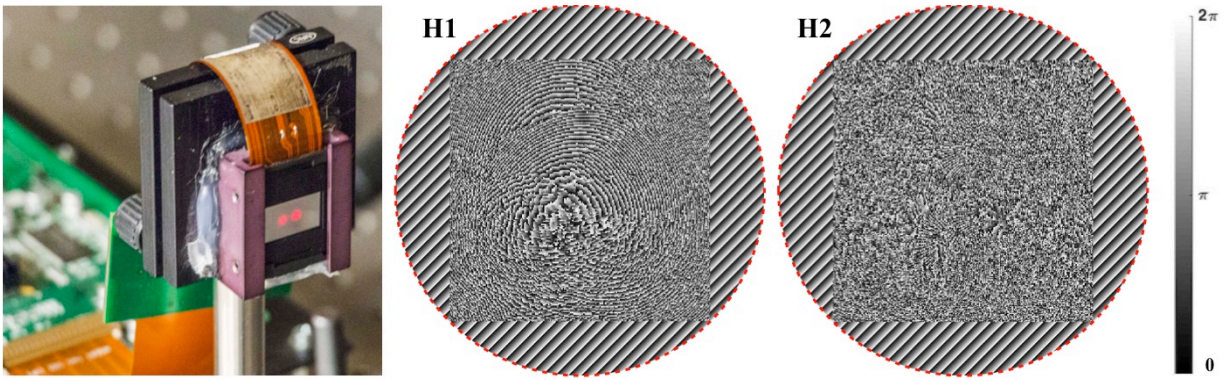

Figure 4.3 Designed layers for frequency multiplexing with 7 wavelengths. The continuous phase patterns are padded with tilted blazed gratings to match with the beam profile (indicated by red dashed circle) while suppressing the background of light unaffected by the SLM.

4.3.2 Angular multiplexing demonstration

To illustrate the principle, we use the design of a two-layer 3D diffractive optics presented in Chapter 3. The pixel number in each layer is 128×128, with pixel size of 8μm×8μm. The layer separation is set to be Δz=486μm. Those parameters are chosen to adapt to the SLM used in the experiment.

For angular multiplexing, we use the letter "C" and "U" from the CU logo (Fig. 3.3a) as the target images for incident angles at 7° and 10°, respectively. we set the output wavelength to be fixed at 633nm, and we use a monochromatic camera (Point Grey CMLN-13S2M) to record the reconstructed image. The results are shown in Fig. 6. When the flip mirror is down, the incident angle is at 7°, the letter "C" shows up on the reconstruction plane (Fig. 4.4a). As we switch the flip mirror up to get an incident angle of 10°, we see the letter "U" on the camera (Fig. 4.4b). The diffraction efficiencies are 50.5% and 52.1% for "C" and "U", respectively. We also notice a weak twin image on the camera which does not appear in the design simulation. This is attributed to imperfections of the SLM and non-ideal experimental conditions. To

verify the design is successful, we illuminate only one layer of the 3D diffractive optics, and a random speckle pattern is obtained (Fig. 4.4c). This indicates that the encryption is distributed among the layers of the 3D diffractive optics.

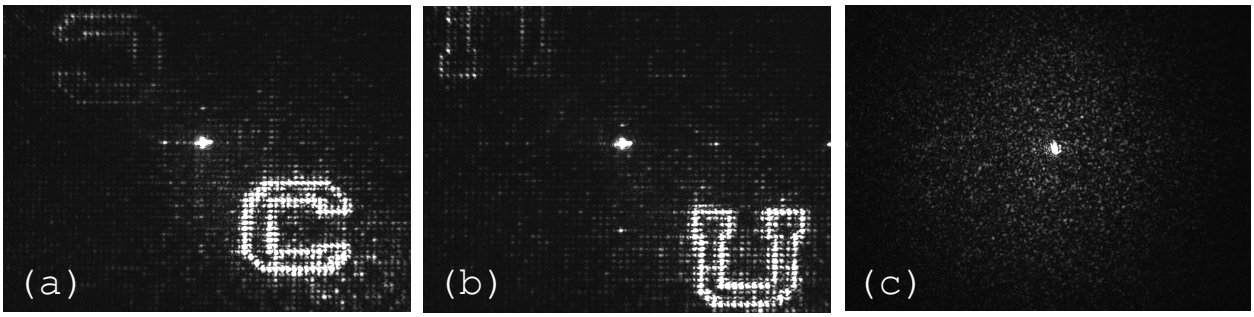

Figure 4.4 Experimental results for angular multiplexing. (a) reconstruction image with incident angle at 7° (b) reconstruction image with incident angle at 10°. (c) Speckle field with one layer blocked, indicating the 3D encryption is successful.

4.3.3 Frequency multiplexing demonstration

To demonstrate frequency multiplexing with high number of degrees of freedom, we multiplexed 7 functions with different colors. Specifically, each letter in the word "boulder" is encoded with wavelength 460nm, 496nm, 532nm, 568nm, 600nm, 633nm, 694nm, respectively.

There are three issues that had to be addressed in the experiment. The first one is coding capacity. Since there is more information to be encoded, we expand the pixel number in each layer from 128×128 to 256×256 to ensure the algorithm converges with acceptable crosstalk on the reconstruction plane.

The second issue is target scaling due to different diffraction angles at various wavelengths. In effect, the letters designed for shorter wavelength appear proportionally smaller on the reconstruction plane than the ones designed for longer

wavelength. This can be compensated by resizing the letters by a scaling factor before running the design algorithm. For example, without resizing, the letter "b" is scaled by 633/460=1.38 with respect to the reference wavelength (633nm), "o" is scaled by 633/496=1.28, and "r" is scaled by 633/694=0.91.

The third issue is phase shift compensation. This issue arises from the fact that the phase shift induced by each SLM pixel depends on both the applied voltage and working wavelength, as is given by the following equation:

$$\Phi\left(U,\lambda\right)=\frac{2\pi d}{\lambda}n\left(U,\lambda\right) \tag{4.2}$$

where d is the thickness of the liquid crystal, λ is the working wavelength, n is the refractive index, and V is the applied voltage, which changes the orientation of the liquid crystal molecules, thus producing various optical path differences for the selected wavelength. The voltage is generated by the SLM's control circuit board, which converts the 256 phase patterns (0~2π) uploaded on the computer to (8 bit) electronic signals. Normally, a lookup-table (LUT), either provided by the manufacturer or experimentally measured, is built in the control circuit to establish a linear, or quasi-linear, relation between the addressed grey phase level and the actual phase delay. Therefore, for the same phase value of the DOE, the phase modulation on the SLM shifts by a constant coefficient as the working wavelength deviates from the designed one. For each layer of the 3D diffractive optics, we have N individual phase patterns $\phi_{\lambda i}(x,y)$ calculated from the design algorithm. The task is to combine these independent phase patterns into one phase pattern while displaying the corresponding phase value for each predefined wavelength. We first convert all the phase patterns to the reference wavelength 633nm, for which the SLM is calibrated. The conversion is done by simply multiplying a scaling factor $\beta_{\lambda i} = \lambda_i/633\text{nm}$ to each individual phase pattern, where λ_i is its corresponding wavelength.

This linear compensation is sufficient in many cases, as the experiments below show, even though the nature of the material dispersion of the liquid crystal is nonlinear. Supplementary Fig. S2b shows that, in general, nonlinear phase deviations can still yield a good reconstruction with somehow reduced diffraction efficiency. If needed, though, the specific material dispersion can be included in the design process for optimal results. We then obtain the design in each iteration by a modified parallel projection, with the phase shift compensation being taken into account:

$$\phi_k(x,y) = \frac{1}{N}\sum_{i=1}^{N} \beta_{\lambda i}\phi_{\lambda i}(x,y) \tag{4.3}$$

where N is the total number of wavelengths used for frequency multiplexing. Fig. 4.3 shows the design results and experimental implementation. The reconstructed (4.3) is recorded with a color CMOS sensor (Canon 5D Mark II). The results are shown ın Fig. 4.5. The experimental diffraction efficiency for each reconstruction image is 38.2% (40.2%), 38.0% (38.9%), 38.5% (39.4%), 35.9% (38.2%), 41.1% (43.5%), 44.9% (47.0%), and 29.8% (30.7%), respectively, with values in simulation provided in the bracket for comparison. The efficiency is not as high as in the angular multiplexing example, because the information of each page decays as more functions are multiplexed. Other factors affecting the diffraction efficiency include the relatively broad spectrum of the laser source and imperfections of the SLM. However, we observed negligible crosstalk among the reconstructions.

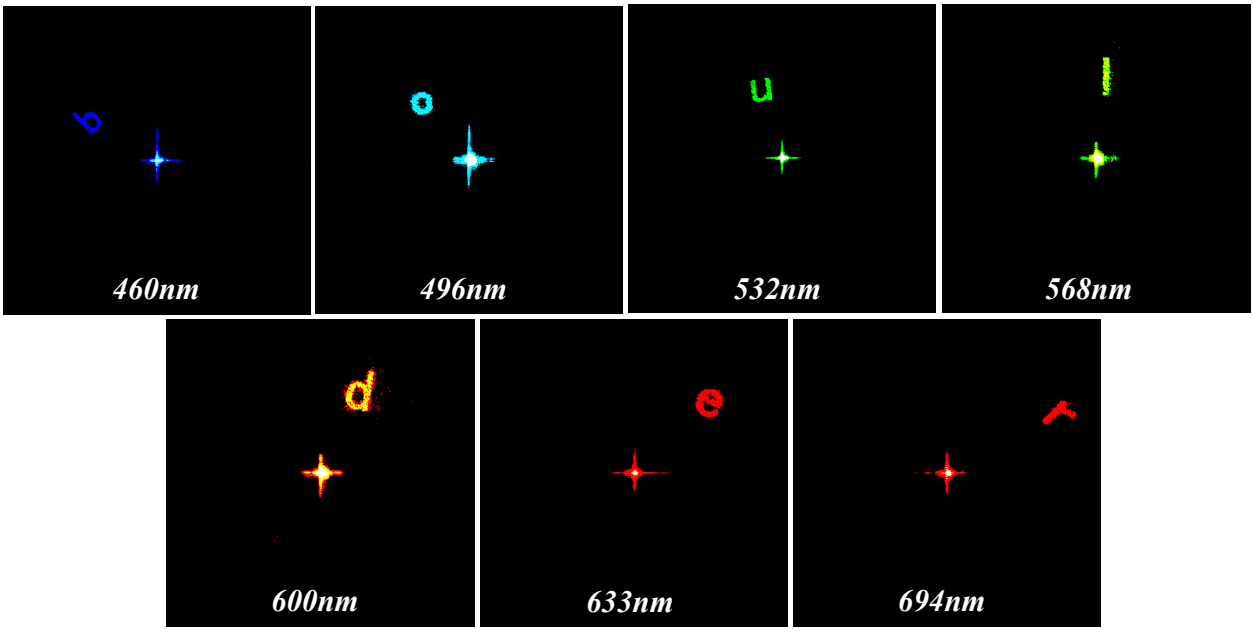

Figure 4.5 Experimental results for frequency multiplexing with 2-layer diffractive optics implemented on a single SLM. The letters in the word "boulder" are reconstructed with wavelength 460nm, 496nm, 532nm, 568nm, 600nm, 633nm, and 694nm, respectively.

4.4 System performance

3D diffractive optics has several interesting advantages relative to thin DOEs in terms of diffraction efficiency, spectral/angular selectivity, as well as new functionalities such as synthetic 3D spatial-temporal wavefront encoding, engineered space-variant functions, and space-time pulse shaping. Here we show the diffraction efficiency can be controlled and enhanced by proper design, due to the additional degrees of freedom provided by the third dimension, compared to 2D DOEs.

The system parameters of importance are the number of layers, N, layer separation, Δz, pixel sizes in the x and y directions, Δx and Δy, and number of pixels

in the x and y directions, Nx and Ny. For the examples shown here, $\Delta x = \Delta y = 8\mu m$, $\Delta z = 486\mu m$. We change $N = 2, 4, 6, \ldots, 20$, $Nx = Ny = 256, 1024$.

We implement a frequency multiplexing scheme with two wavelengths, 633nm and 532nm, to encode two desired reconstruction functions. For the purpose of investigating diffraction efficiency, the target images are two off-axis spots at different locations. The first (second) spot, which corresponds to the 633nm (532nm) illuminating wavelength is located halfway (three quarters) from the center to the edge of the far-field grid used.

The 3D diffractive optics are designed with the POCS algorithm with distribution-on-layers optimization. The two spots are reconstructed as designed, namely the first spot (left) shows up for 633nm wavelength reconstruction, and the second one (right) for 532nm. The diffraction efficiency of both spots as functions of the number of layers and the number of pixels are shown in Fig. 4.6.

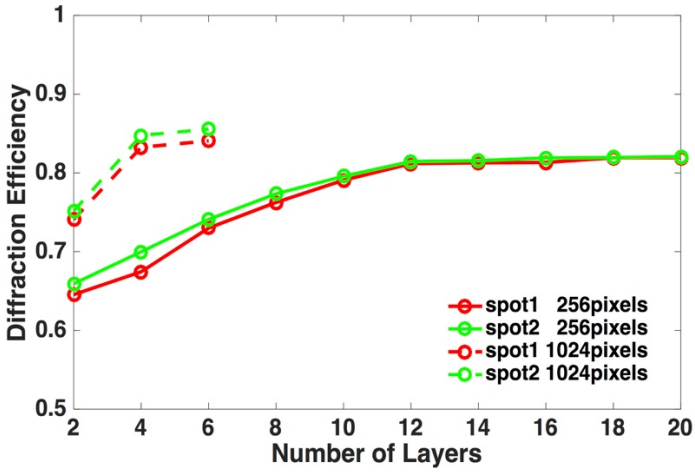

Figure 4.6 Diffraction efficiency as functions of the number of layers and the number of pixels in each layer. The solid red line is the diffraction efficiency of the first spot as a function of the number of layers with 256×256 pixels. The solid green line is the diffraction efficiency of the second spot as a function of the number of layers with 256×256 pixels. The dashed red line is the diffraction efficiency of the first spot as a function of the number of layers with 1024×1024 pixels. The dashed green line is the diffraction efficiency of the second spot as a function of the number of layers with 1024×1024 pixels.

It takes less than 1 minute to finish the design at two layers with 256×256 pixels, on a 2.8GHz quad-core CPU with 12Gb memory. The diffraction efficiencies for the two spots are 64.55% and 66.68%, respectively. As the number of layers increased to 20, the diffraction efficiencies increased to 70.28% and 72.07%, respectively. As we use 1024×1024 pixels in each layer, the diffraction efficiencies for the two spots are 74.11% and 75.16%, respectively, when the number of layers is 2. The numbers increase to as large as 83.26% and 84.77%, respectively, as 6 layers are used in the design. Designs with more layers are beyond the computational power of a personal computer but are still possible with more powerful hardware.

This result, like all other results, confirms the hypothesis that 3D diffractive optics indeed provides additional degrees of freedom to enhance system performance such as diffraction efficiency. One would expect further improvements in diffraction efficiency with more layers and more pixels.

4.5 System limits

4.5.1 SLM deviations analysis

SLMs are common devices for light manipulation purposes. In particular, reflective SLMs are more popular because of shorter response time and higher fill factor. The ideal phase-only reflective SLM addresses arbitrary phase profiles onto a coherent light beam. However, the reflective display panels usually suffer deviations between the applied voltages and the designed phase values, due to the non-ideal production process [89–91]. Those distortions could lead to performance degradation.

Here, we investigate the effect of SLM phase drifts on 3D diffractive optics in terms of diffraction efficiency and relative error.

The 3D diffractive optics is designed of 2 layers with 128×128 pixels in each layer. Letter "C" and "U" in a frequency multiplexing scheme, namely "C" with 633nm illumination and "U" with 532nm illumination. The pixel size is 8μm×8μm, and the layer separation is 486μm. The simulation yields diffraction efficiencies of 62.5% for "C" and 65.5% for "U", with a relative error of 0.16 and 0.14 respectively.

The investigation is conducted in four aspects. First, we test the linear deviation. This applies to an SLM that is not properly calibrated, or the wavelength or direction of the incident beam is drifted from the designed value. The result is the phase modulation from the SLM is linearly shifted from the original by a constant coefficient. We set the coefficient to be 0.8, 0.6, and the 0.4, as is shown in Fig. 4.7a. The corresponding diffraction efficiencies for the far-field pattern decrease as the deviation becomes larger and as more energy being transferred to the DC term. Accordingly, as expected, the relative error increases.

Second, we test the effect of a nonlinear deviation in the SLM phase. This occurs when there are errors in the look-up table which is a built-in mechanism in the SLM's control circuit to linearly convert the gray level of the input phase pattern to the resulting phase retardation of the liquid crystal molecule by properly adjusting the applied voltage. The phase map of the designed layers are converted in a nonlinear fashion, for the 2nd, 3rd, and 4th order, as is shown in Fig. 4.7b. The diffraction efficiencies drop more as higher order nonlinear deviations are induced. A stronger DC term shows up as well as larger errors are being generated.

Third, we add random noise with different levels to the phase map. This is to simulate irregularities of liquid crystal cells, which cause a spatially varying phase response of the SLM. Fig. 4.7c shows results for random noise levels of 20%, 40%, and

60%. The diffraction efficiencies of both patterns are impaired as the noise level increases, and speckles start to appear in the background.

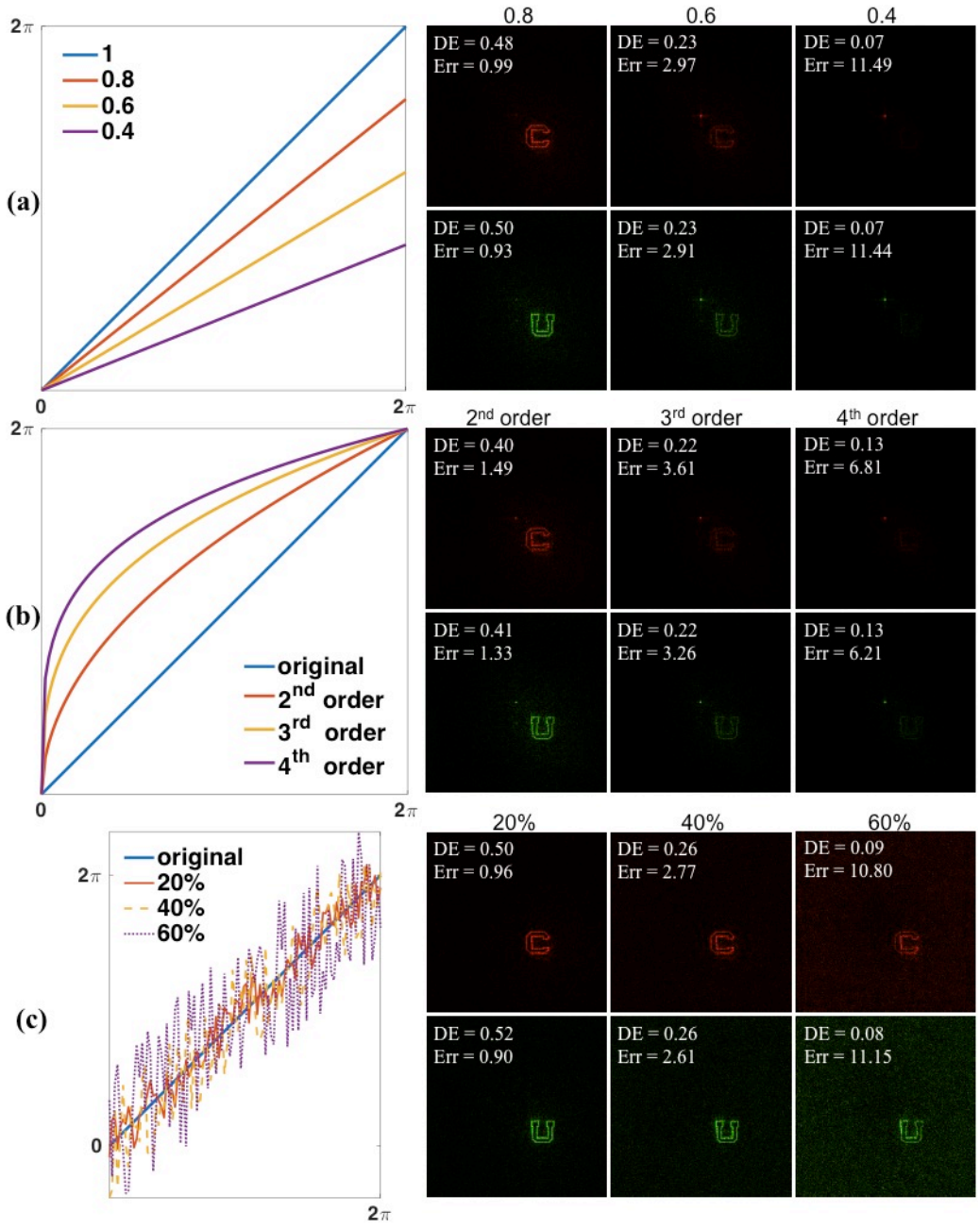

Figure 4.7 Simulation results for SLM phase deviation analysis. (a) linear deviation of the phase map of 20% (0.8), 40% (0.6), and 60% (0.4) with the corresponding reconstructed images. (b) phase map of nonlinear deviation of 2nd, 3rd, and 4th order with the corresponding reconstructed images. (c) phase map with added random noise at levels of 20%, 40%, and 60% with the corresponding reconstructed images.

Last, we investigate SLM phase deviations in a combined situation. As shown in Fig. 4.8, a cubic phase deviation is induced, and it comes with positive and negative linear phase shift. This is more likely to happen in the real world, and the result is decrease of diffraction efficiency and DC spots show up at the center.

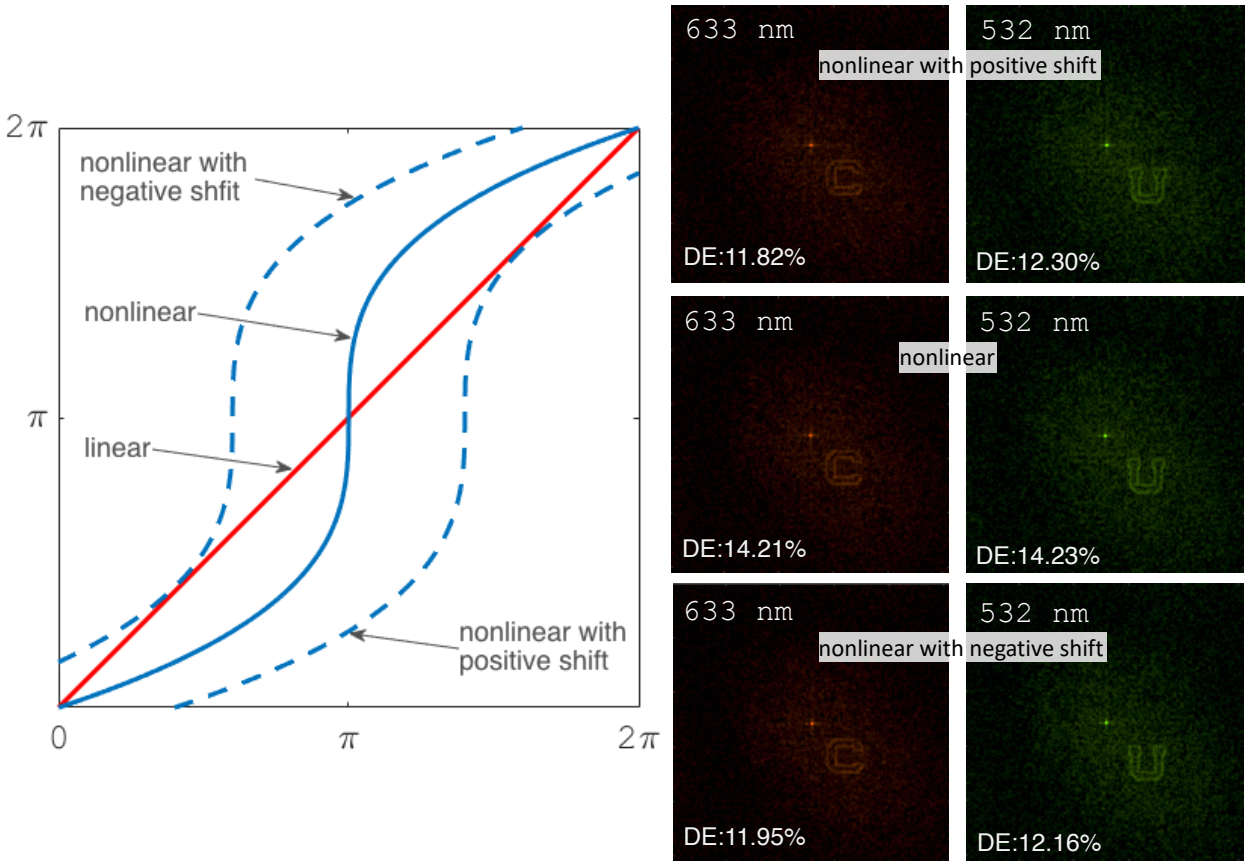

Figure 4.8 Simulation results for SLM phase deviation in cubic fashion with positive and negative shift. (left) Phase map indicating all the analyzed deviation situations. (right) the corresponding reconstructed images with diffraction efficiency.

4.5.2 Misalignment analysis

We investigate the effect of misalignment between the two layers. The design is up-sampled 8 times such that modeling of the layer can be shifted distances as

small as 1μm. Visualization 2 shows the reconstructed pattern under both 633nm and 532nm illumination as the second layer is misaligned from -20μm to 20μm. The corresponding diffraction efficiency and relative error are plotted in Fig. 4.9a. The results show that with 2 layers, the misalignment tolerance could be up to 1 pixel (8μm) and still yield acceptable reconstructed patterns. Visualization 3 shows the alignment tolerance in longitudinal direction. In frequency multiplexing scheme, the second layer is misaligned from -50μm to 50μm with respect to the 486μm layer separation in the design. The diffraction efficiency and relative error are plotted in Fig. 4.9b. Acceptable reconstructed patterns are obtained from in the misalignment range from -25μm to 25μm. Alignment tolerances become more critical as the number of layers is increased.

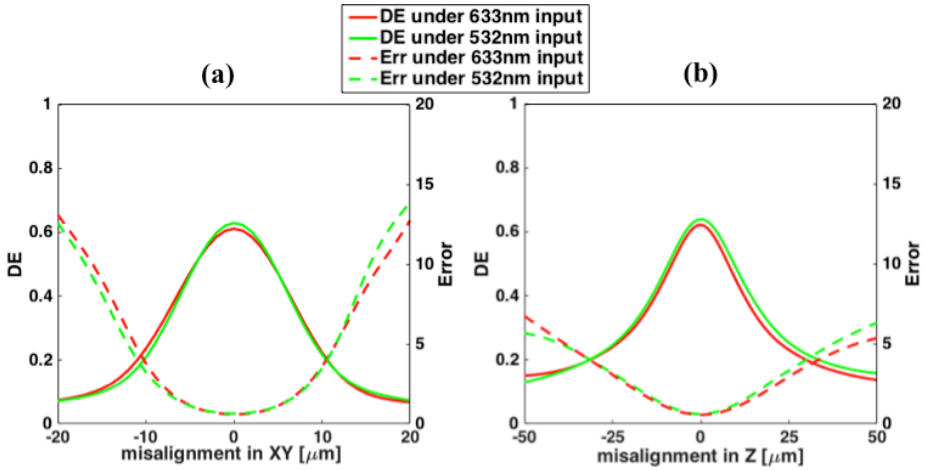

Figure 4.9 Simulation results for layer misalignment analysis. The diffraction efficiency and relative error of the two far-field patterns, corresponding to 633nm and 532nm in a frequency-multiplexing scheme, are plotted as a function of relative shifting distance between the two designed layers.

4.5.3 Multiplexing limits

Angular and frequency multiplexing are the two important functionalities of the proposed 2D implementation of 3D diffractive optics. Here, we provide a discussion on the impact of the interval between the multiplexed angles or wavelengths on the crosstalk of the encoded information. We design 3D diffractive optics consisting of 2 layers and 4 layers, each layer has 128×128 pixels in frequency multiplexing. We encode "C" at 633nm while changing the encoding wavelength for "U" from 632nm to 583nm. The minimum wavelength interval relates to the number of layers in the 3D diffractive optics. The results are shown in Fig. 4.10. We find similar trends for angular multiplexing.

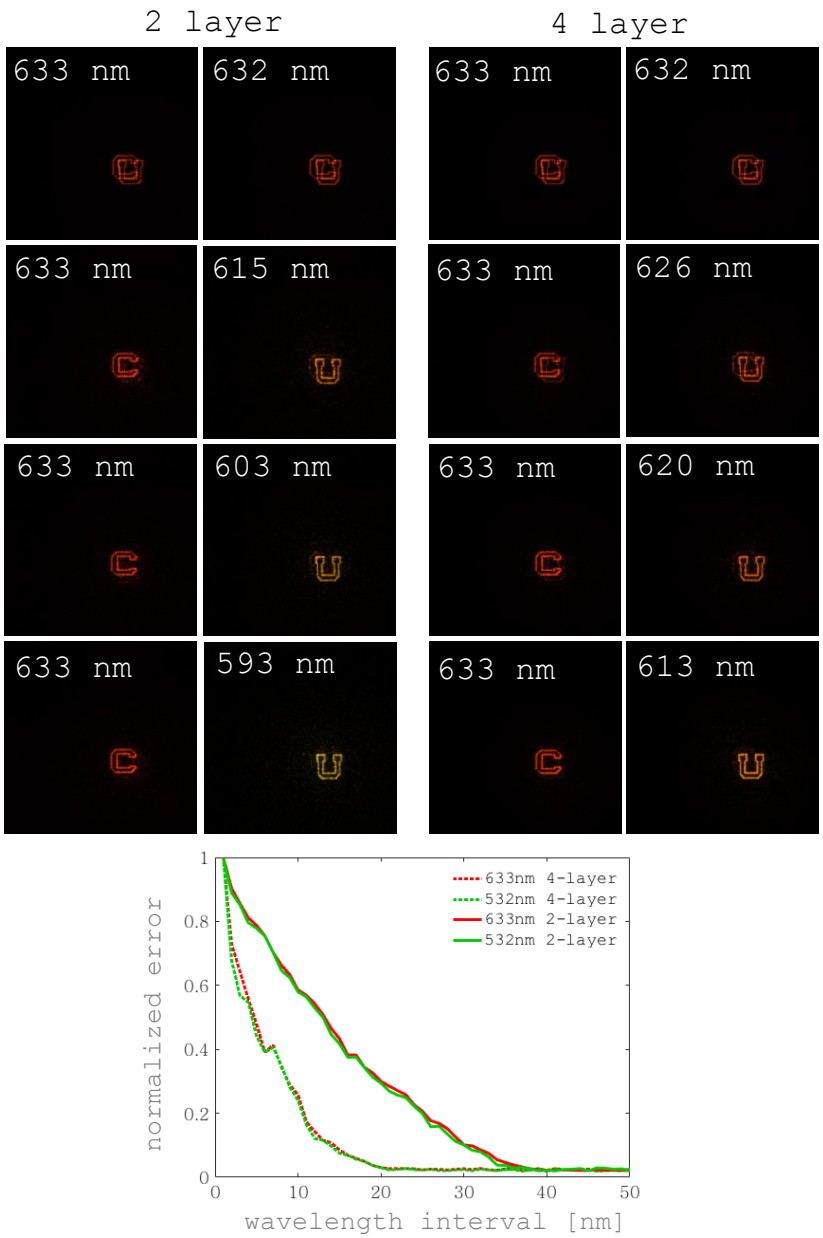

Figure 4.10 Crosstalk measurement for frequency multiplexing with 2 layers and 4 layers. Top left: The reconstructed images are displayed for designs using 2 layers at selected wavelength intervals. Top right: The reconstructed images are displayed for designs using 4 layers at selected wavelength intervals. Bottom right: Normalized error in wavelength multiplexing as a function of wavelength interval between the two reconstructions.

4.6 Conclusion

We proposed an approach to implement 3D diffractive optics on a 2D dynamic SLM. We analyzed the fundamental opportunities and limitations, while the experiments confirmed the predicted performance.

The design is implemented on widely available SLMs, which are capable of switching the phase patterns at relatively high frame rates, thus enabling operation with multiple wavelengths or codes both simultaneously and dynamically. While we show possible implementations for more than 2 layers, an alternative implementation could include a single large spherical mirror, with the addition of properly designed space-variant quadratic phase factors and blazed gratings onto the SLM to steer the reflected beam to the desired locations. Furthermore, one could use multiple SLMs to simplify the geometry and increase the total space-bandwidth product.

The results show that light fields are modulated in multiple dimensions with a compact and efficient system. Independent information is successfully encrypted and read out, with high efficiency and low crosstalk. This approach will benefit from the ever-increasing computational power and advances in SLM technology.

Dynamic 3D diffractive optics could be beneficial for numerous applications that require independent multi-color operation. For example, for an imaging lens, chromatic aberrations could be corrected at different wavelengths by pre-shaping the wavefront with a frequency multiplexing scheme. In optical tweezers, where attractive or repulsive force is generated from focused laser beams, 3D diffractive optics could implement multiple dynamic independent focused beams at different wavelengths, thus achieving manipulation of multiple microscopic objects. Furthermore, a 3D diffractive optical system could couple multiple modes into a multimode fiber, each matched in frequency and spatial shape, e.g. modes with

angular momentum of various wavelengths [32,77]. Likewise, one could use 3D optics to analyze (demultiplex) the modes coming out of such a system. In a totally different application, 3D diffractive optics could be used in multi-color single-molecule localization microscopy with higher efficiency and capacity than what has been recently demonstrated [92,93]. Other interesting applications include beam steering, beam shaping, 3D display, and data storage.

Chapter 5

3D Diffractive Optics for Azimuthal Multiplexing

5.1 Introduction

In this chapter, we propose azimuthal multiplexing, by which multiple output signals are switched upon the relative rotation of one or more layers within the 3D diffractive structure. We implement the inverse design with an iterative projection algorithm with distribution on layers. We demonstrate experimentally the principle with two phase layers fabricated lithographically following the multilevel binary optics technique [94].

Holographic multiplexing refers to the possibility of encoding multiple pages of data by changing spatial, frequency, or polarization of the inputs. It is a unique property of 3D diffractive optics which allows for independent information distributed throughout the recording medium. Individual signals can be retrieved with minimum crosstalk, as a result of the engineering of the volumetric refractive index structure [95]. The reconstruction degrades as the input beam deviates from the designed values, namely Bragg-like behavior, and this selectivity is mainly determined by the thickness of the structure [17].

Angular and frequency (wavelength) multiplexing are the most common forms of multiplexing. The former one enables additional information to be encoded but needs extra efforts in alignment, whereas the latter one is easier to arrange but requires a complicated laser system that can be tuned in broad spectrum. Other techniques, proposed in optically recorded holography, include peristrophic [96] and shift multiplexing [97], referring to rotation and translation of the holographic sample. However, they are limited by the possible 3D fields obtained from the interference of an object and reference waves inside photosensitive materials.

Early in the 1970s, Alvarez and Lohmann independently proposed composite lenses whose focal length can be adjusted continuously by shifting laterally two optical elements with cubic phase profile [98,99]. Recent work improved on this idea by implementing the tuning mechanism through rotation [100,101]. These devices are designed analytically to continuously change the optical power of lenses or axicons.

Here, we propose azimuthal multiplexing, a novel multiplexing technique that enables recording of multiple output signals switched upon the rotation of one or more layers with respect to the others, i.e. the information is encoded in the azimuthal dimension of the 3D diffractive optics.

5.2 Theory

5.2.1 Physical model

We consider a stratified 3D diffractive optical element composed of multiple 2D layers of phase modulation spatially separated by thin homogeneous isotropic

media (Fig. 5.1). Each layer can rotate with respect to a common axis (the optical axis). Under the scalar and thin-element approximation, the phase modulation for coherent illumination can be described by

$$E\left(x,y,z_k^+\right)=\exp\left\{j\phi_{k,\theta}\left(x,y\right)\right\}E\left(x,y,z_k^-\right), \tag{5.1}$$

where E is the complex amplitude, k is the layer number and θ denotes its rotation angle. In the homogenous region between adjacent layers, diffraction occurs and can be described by the angular spectrum propagation in free space

$$E\left(x,y,z_{k+1}^-\right)=\mathscr{F}^{-1}\left\{e^{-j\sqrt{k_0^2-k_x^2-k_y^2}\cdot\Delta z}\cdot\mathscr{F}\left[E\left(x,y,z_k^+\right)\right]\right\}, \tag{5.2}$$

where Δz is the layer separation, "z^+", "z^-" represent the coordinates immediately before and after the corresponding layer, and F is the Fourier transform. The wave field on the reconstruction plane is calculated using Fresnel or Fraunhofer propagation [102].

$$E_R\left(x,y\right)=\begin{cases}\mathscr{F}^{-1}\left\{e^{-j\sqrt{k_0^2-k_x^2-k_y^2}\cdot z_R}\cdot\mathscr{F}\left[E\left(x,y,z_N^+\right)\right]\right\}, \text{ Fresnel region}\\ Q[\frac{1}{\lambda f}]V[\frac{1}{\lambda f}]\mathscr{F}\left[E\left(x,y,z_N^+\right)\right], \text{ Fraunhofer region}\end{cases}, \tag{5.3}$$

where Q is the quadratic factor and V is the scaling factor [55]. z_R is the distance from the last layer to the reconstruction plane, and f is the focal length of the Fourier lens. The propagation process is also reversible, described by the conjugate forms of the above equations. Accordingly, the phase for each layer satisfies

$$\phi_{k,\theta}\left(x,y\right)=\arg\left\{\frac{E\left(x,y,z_k^+\right)}{E\left(x,y,z_k^-\right)}\right\}. \tag{5.4}$$

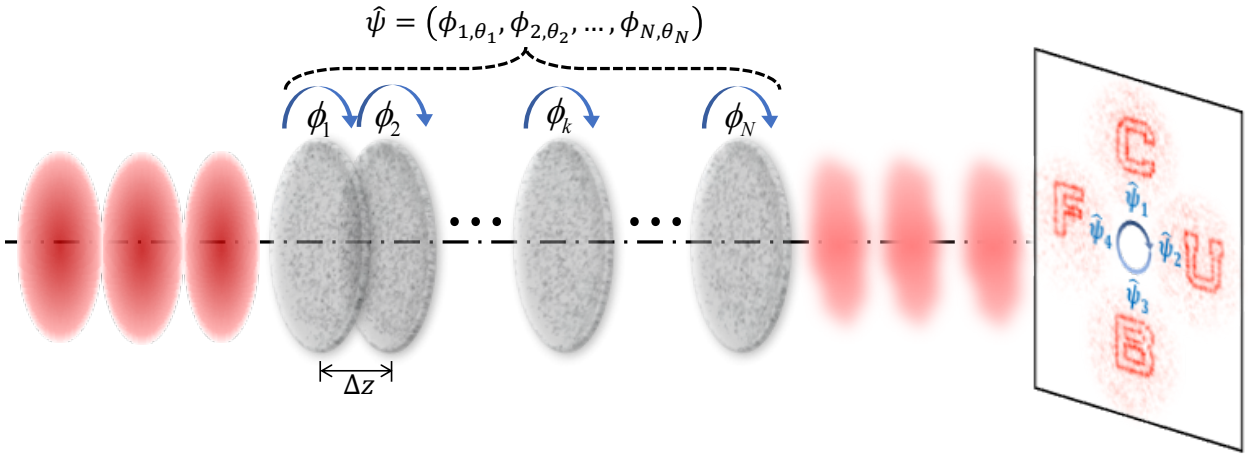

Figure 5.1 Physical model of 3D diffractive optics, which consists of N layer of phase modulation, separated by a short free-propagation distance of Δz. Each layer can rotate with respect to the optical axis while optical waves are modulated passing through the 3D diffractive optics.

5.2.2 Azimuthal multiplexing design

We design the layer of phase modulation in round shape to ensure it rotates to an arbitrary angle without redundant pixels or the need to enlarge the beam size, and we apply bilinear interpolation to keep the number of active pixels constant during rotation. It is worth noting that the calculation of backward propagation should apply the following constraints to avoid error caused by zero denominator due to the zeros outside the aperture

$$E\left(x,y,z_k^-\right)=\sum_{i,j}E\left(x_i,y_j,z_k^-\right)=\frac{E\left(x_i,y_j,z_k^+\right)}{\exp\left\{j\phi_{k,\theta}\left(x_i,y_j\right)\right\}} \quad (5.5)$$

$$\text{where } x_i,y_j \in circ\left(\frac{\sqrt{x^2+y^2}}{r}\right)$$

where r is the radius of the layer.

With the physical model described in Chapter 3, we establish the connection between the input $E(x,y,z_1^-)$and output $E_R(x,y)$ of the 3D diffractive optics.

Suppose a 3D diffractive optics consists of N layers. In order to calculate the phase modulation function layer by layer, we start by setting all of them to random values while the amplitude is a circular function. The input is $E(x, y, z_1^-)$ which contains the information of wavelength and incident angle, both are constants in this case. There are m+1 pages of reconstruction patterns to be multiplexed $E_R^0(x, y)$, $E_R^1(x, y)$, …, $E_R^m(x, y)$, with the corresponding rotation angle of the k-th layer at 0, θ_1, …, θ_m. We design azimuthal multiplexing 3D diffractive optics using an iterative projection optimization algorithm with a distribution on layers method. This approach is flexible, as the layer being rotated can be any one or any combinations from 0 to N, and can switch during the encoding process.

Basically, there are three optimization loops embedded in the design algorithm. The first loop is to optimize one single layer according to the target metrics. We apply the forward propagating model described by Eqs. (1)-(3) from input to the wave field in front of the k-th layer $E(x, y, z_k^-)$. We then continue to the reconstruction plane where the amplitude is updated with the pre-defined reconstruction field $E_R^0(x, y)$ and the phase is kept unchanged. Next, the backward propagation described by the conjugate form of equation (1)-(3) is applied from the reconstruction field to the wave field after the k-th layer $E(x, y, z_k^+)$. Thus the phase modulation can simply be derived from equation (4). We update $\phi_{k,0}^0$ and iterate until it reaches a satisfactory solution or a predefined number of iterations is completed. This is the first loop, which is repeated for all the remaining layers $\phi_{1,0}^0$, $\phi_{2,0}^0$,… , $\phi_{N,0}^0$.

We then rotate the k-th layer to θ_1, and repeat the above process except the reconstruction field is $E_R^1(x, y)$. As a result, we obtain the phase modulation optimized for the second target $\phi_{1,0}^{\theta_1}$, $\phi_{2,0}^{\theta_1}$,…, $\phi_{k,\theta_1}^{\theta_1}$,…, $\phi_{N,0}^{\theta_1}$. We follow the same procedure until all the targets are encrypted in all the layers, and that becomes the second loop.

To ensure all the multiplexing cases being considered are evenly distributed among all the layers, we apply a parallel projection, described by the following equation

$$\phi_{j,0} = \frac{1}{m}\sum_{i=0}^{m}\phi_{j,0}^{\theta i},\ j = 0,\ 1,\ ...,\ N, \tag{5.6}$$

and update the phase modulation functions. All the calculations up to this point conclude one iteration in the third optimization loop. The algorithm keeps iterating until the results are satisfactory or the iteration number is reached. The overall flowchart of the design algorithm is shown in Fig. 5.2.

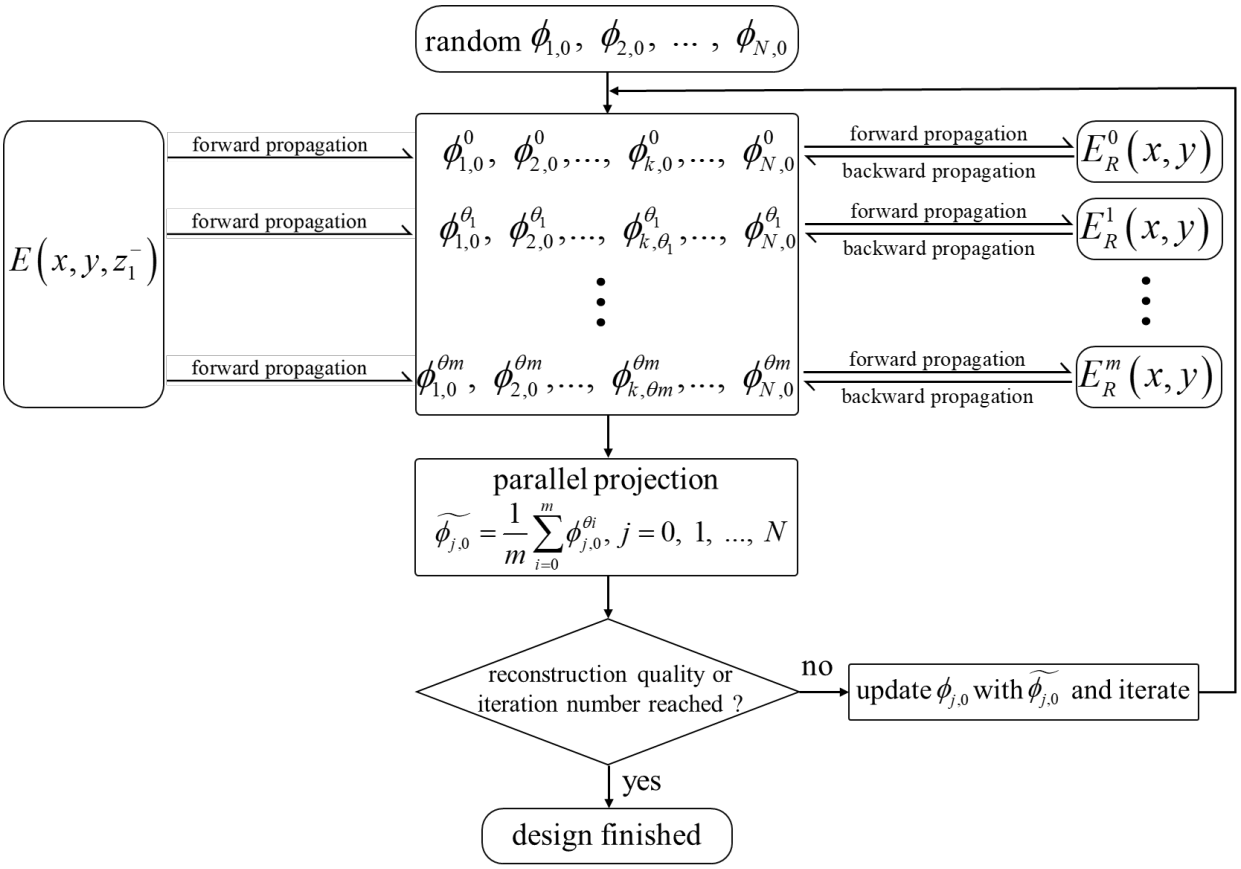

Figure 5.2 Flowchart of the iterative projection optimization algorithm used for the azimuthal multiplexing design. Within each iteration, the wave fields are forward propagated from the input to the plane right before the *k*-th layer to be designed, and backward propagated from the preset target to the plane right after the *k*-th layer to be designed.

It should be noted that the convergence of the algorithm depends on the task complexity, namely the number of functions to be multiplexed, and degrees of freedom available, namely the number of layers and number of pixels in each layer.

5.3 Simulation results

To demonstrate the principle, we design a two-layer 3D diffractive optics for azimuthal multiplexing of 4 functions. The target patterns are arbitrary, and defined digitally on a computer as the letters "C", "U", "B", "F" (Fig. 5.3b). They are encoded with 4 rotation angles of the second layer respectively, which are purposely chosen to be off multiples of 90˚ at 0˚, 88˚, 195˚, and 287˚.

The initial design of a 3D diffractive optics consists of two layers, separated by 1 mm. Each layer has 128×128 pixels with the pixel pitch of 40 μm. The parameters are chosen to facilitate the alignment in the experiment in the lab environment. If that is not a concern, with high precision mounts, more compact devices can be designed using smaller pixel size, and/or large volumetric bandwidth with enhanced pixel number.

Under a plane wave normal illumination at 633 nm, the two layers with continuous phase modulation ranging in $0\sim2\pi$ are designed using the algorithm described in Section 5.2. However, to implement experimentally with photolithography, we need to discretize the phase distribution. Here we design it to 8 phase levels, because it simplified the experimental implementation without compromising too much efficiency. There are two approaches. The first one is the commonly used "hard-cut" approach where at each iteration the phase values are forced to the allowed ones they are closed to. The second one is the "soft-cut" approach

which we built in our design algorithm. In this approach, we set regions centered in the allowed 8 phase values, and if the designed phase value is outside those regions, it will be expelled to the edge of whichever region it closed to. The allowed regions shrink with the iteration number until, at the end, there are only 8 phase values allowed. Compared with the "hard-cut" approach, the "soft-cut" approach helps the algorithm's convergence and improves the efficiency of the reconstruction.

Fig. 5.3a shows the two designed layers with 8 phase levels using the "soft-cut" approach. The numerical reconstruction of the design with the second layer rotated at 4 encoded angles are shown in Fig. 5.3c. Note that the reconstruction plane is enlarged twice (via zero-padding of the near field) to avoid wrap-up aliasing and to take light scattering into account. The diffraction efficiency of the 4 reconstruction patterns are 43.60%, 42.38%, 47.12%, and 44.83%, respectively.

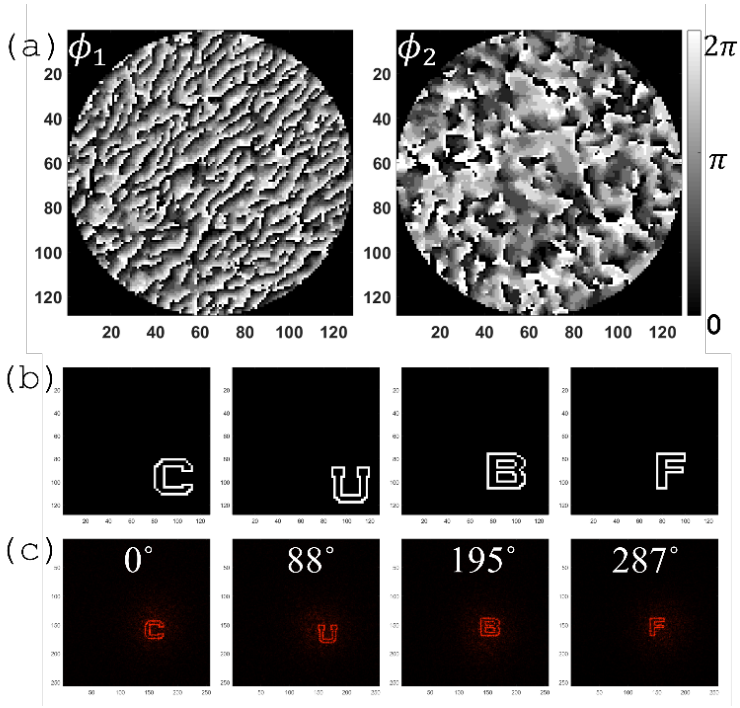

Figure 5.3 Simulation results of azimuthal multiplexing 3D diffractive optics. (a) The design of two layers of phase modulation discretized to 8 levels. (b) Target images of the 4 letters to be multiplexed. (3) Numerical reconstructions form the 3D diffractive optics while the second layer is rotated at angles specified by design.

5.4 Experimental results

5.4.1 Device fabrication using photolithography

In this section, we present experimental demonstration of azimuthal multiplexing with two-layer 8 phase level diffractive optics. To fabricate the DOEs, we first convert each of the two layers to three binary amplitude masks, as shown in Fig. 5.4a. The three binary masks are then arranged together with another mask defining the aperture and orientation angles on a single wafer with a size of 4 inch by 4 inch (Fig. 5.4b). It should be pointed out that the second layer is horizontally inverted, since we etch the two substrates on the edge and place them facing each other during the reconstruction. It is also crucial that the three binary masks are aligned at the exact same location during the exposure process. To facilitate that, several alignment markers, coarse and fine, are embedded around the modulation area.

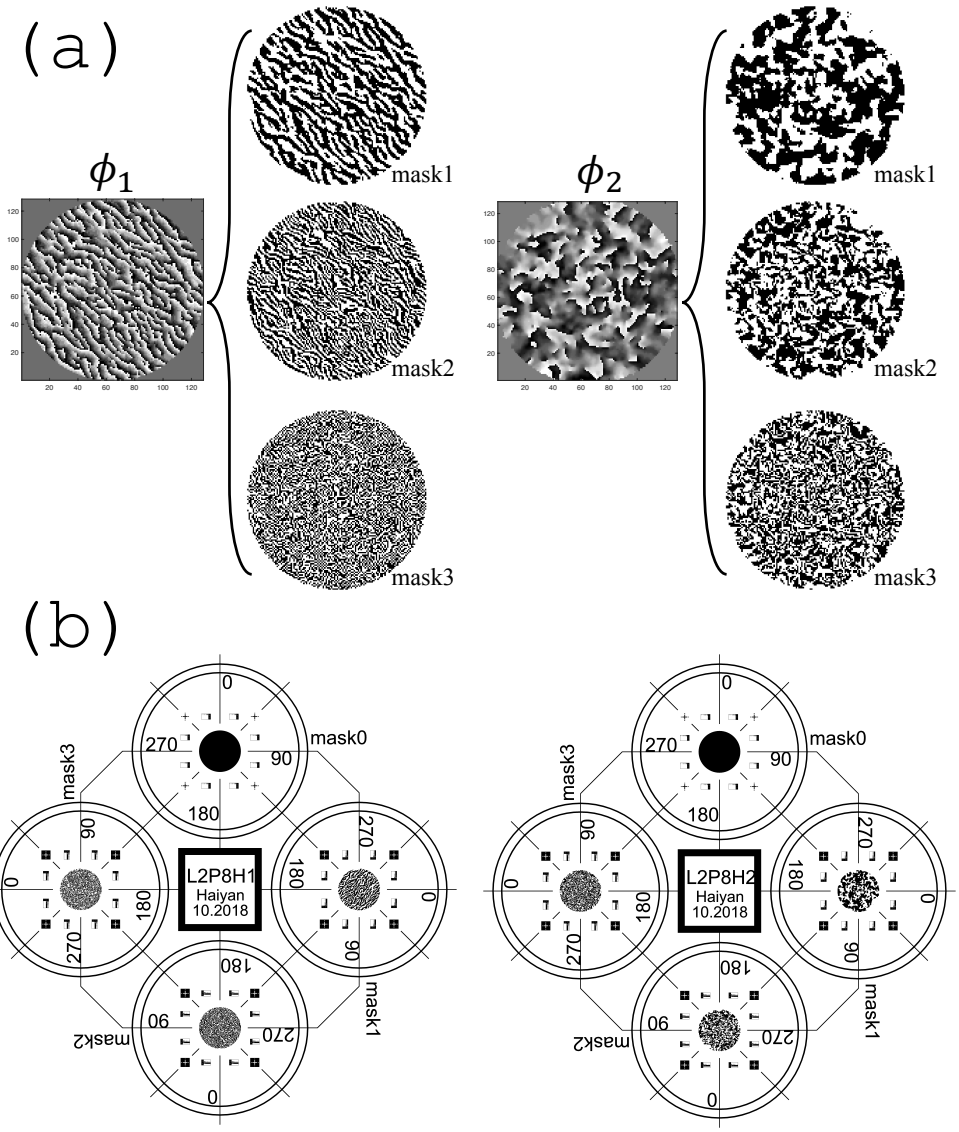

Figure 5.4 Binary amplitude mask designs for 3D diffractive optics. (a) Each of the two 8-level phase masks are generated by three binary masks. (b) The three binary masks are arranged on a same wafer with another mask defining aperture and orientation angles. The design is fabricated using Heidelberg 66FS mask writer.

The wafer is fabricated with a Heidelberg DWL 66FS (Fig. 5.5a), and the examination under microscope shows good quality structures (Fig. 5.5b). The DOE substrate is an uncoated UV fused silica precision window (Thorlabs WG41010), with 1 inch diameter and 1mm thickness. We first coat the substrates with 80nm chromium using CVC thermal evaporator. Then we use chemical etching to take away

the parts that define the aperture as well as the orientation. The substrates are then coated with AZ 4210 for 3µm, a positive photoresist, on a spinner at the speed of 3000 rpm for 60s. The photoresist is then pre-baked on a hotplate at 100C for 90s. During the exposure process on the SUSS MJB3 mask aligner, the pattern on the binary mask allow the photoresist on substrate to be exposed by UV light. That induces chemical change in the exposed region which is removed after developing with 1:3 concentration of AZ400K and de-ionized water. The last step is reactive ion etching (RIE), which is suitable for removing material along the vertical direction. Here we use a mixture of CF4 for 16 standard cubic centimeters per minute (SCCM) oxygen for 4 SCCM, which yields an etching rate of 31nm per minute. By proper control of the etching time, we obtain different etching depths for different exposures. The whole process is repeated 3 times for each phase mask and an 8 level modulation is achieved as a result (Fig. 5.5c).

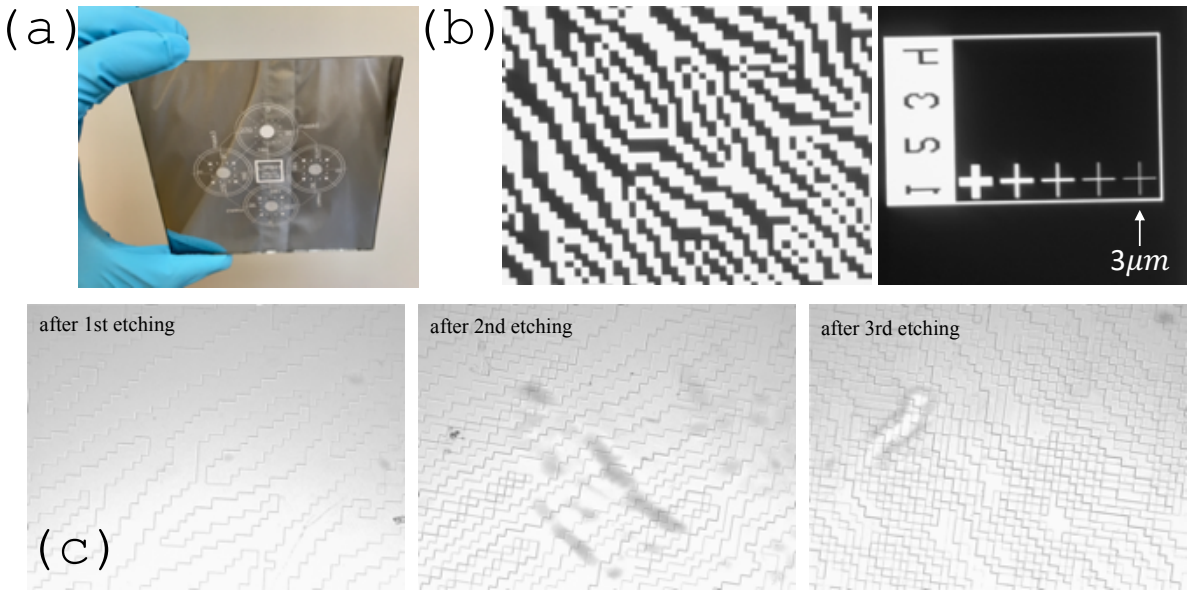

Figure 5.5 Fabrication of diffractive optical element using photolithography. (a) Binary masks fabricated by Heidelberg 66FS mask writer. (b) Microscope images of the fabricated binary masks. The binary masks are aligned well during each exposure/etching. (c) Microscope images of the substrate after each of the three etching processes.

5.4.2 Reconstruction results

Fig. 5.6a shows the fabricated sample with a microscopic image of the surface after etching 3 times. We can see each etching step overlaps appropriately with the help of the alignment markers. The surface profile is examined with a 1D stylus profilometer, where 8 phase steps are recognizable. In spite of some roughness on the surface, which is probably due to the non-ideal condition of the RIE, the 3D diffractive optics samples are robust and the desired reconstructions are still successfully obtained as shown below. Fig. 5.6b shows the reconstruction setup. We use industrial grade double-sided tape to attach the two substrates on adaptors, with the etched sides facing each other (the phase pattern of one layer is mirrored left-right in the fabrication process). The two adaptors are then secured on two lens mounts, one of which is mounted on a 3-aixs translation stage to provide control of tip/tilt and translation in X, Y, Z direction, the other provides control for the same as previous in addition to rotation (Thorlabs K6XS). Both layers are adjusted concentric and normal to the incident beam, with a separation distance of 1 mm as in the design. After the second layer, we place a Fourier lens with a focal length of 300 mm to yield a far-field plane of the output from the 3D diffractive optics, where a color CMOS sensor (Canon 5D Mark ii) is placed to capture the reconstructed images. With spatial-filtered and collimated illumination from a He-Ne laser, we obtained the reconstructed images (Fig. 5.6c) as the second layer is rotated to the designed angles. The measured diffraction efficiency is 33.65%, 29.28%, 36.46%, and 31.50%, respectively.

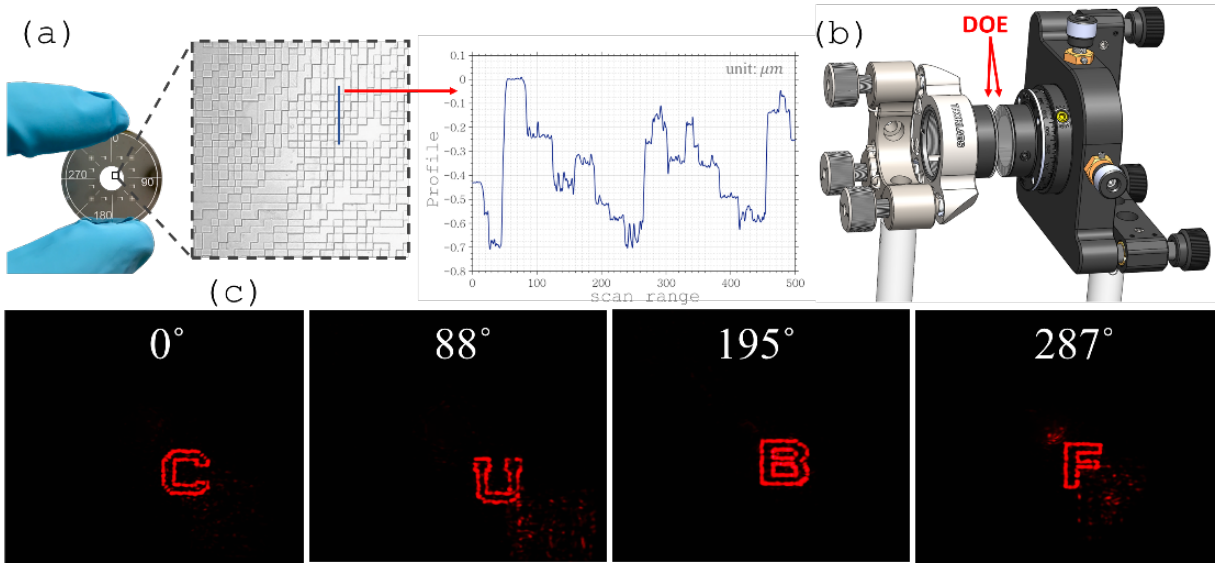

Figure 5.6 Experimental results of azimuthal multiplexing 3D diffractive optics. (a) One DOE fabricated using photolithography. The substrate is coated with chromium that contains markers on the periphery indicating orientation. The aperture encircles the layer of phase modulation at the center. The phase modulation is achieved by a 3-step exposure and etching. The plot shows a characterization of the surface profile using a 1D stylus profilometer. The diffractive optics is robust as the reconstructions can still be obtained with some roughness on the surface. (b) The setup for reconstruction. The two layers are attached on adaptors which are secured on lens mounts, with the etched sides facing each other. Both layers are adjusted normal to the incident beam, and separated by 1 mm. The layers are adjusted to be concentric by transverse shifts and can rotate with respect to each other. (c) Reconstructed images with threshold value 10% relative to maximum when the second layer is rotated, with respect to the first layer, at 0 ˚, 88˚, 195˚, and 287˚ (the angles specified by design).

5.5 System performance

5.5.1 Phase quantization methods

There are various ways to implement the designed DOEs. A widely used method is via spatial light modulators (SLMs), which allows for easy and fast display

of phase patterns with 8 bit resolution (256 grey levels) on the liquid crystal panels. However, SLMs are polarization sensitive thus suffer from substantial loss of energy [103]. Moreover, they are 2D devices thus not suitable for implementing 3D diffractive optics unless cascaded or creating a folded system [17]. Alternative methods generate surface relief structures in an optically transparent material such as glass, quartz, or polymer, and include ion beam etching, direct diamond tuning, gray-level lithography, and multi-step binary exposure photolithography [104].

In our experiment, each layer of the 3D diffractive optics is fabricated using a photolithographic method. To approximate a continuous surface profile, the lithography process is repeated M times to yield a discrete structure with 2^M steps. Here we use 8 phase levels and accordingly 3 amplitude masks are needed for the fabrication. The phase modulation induced by the depth change is given by

$$h(x,y) = \frac{\lambda}{n(\lambda)-1}\frac{\phi(x,y)}{2\pi} \tag{5.7}$$

where λ is the wavelength of operation and n is the refractive index.

To prepare for the fabrication, we need to discretize the phase values in the design. In particular, we allow 8 etching depths which correspond to phase values of 0, 1/4 π, 1/2 π, 3/4 π, π, 5/4 π, 3/2 π, and 7/4 π. One common quantization method is "hard-cut" where at each iteration the phase values are compelled to the closest allowed values. Here, in contrast, we use a "soft-cut" method to improve the coding. In this method, during the iterative optimization, the design phase values are allowed in a region around the preset values. These regions shrink after each iteration until only 8 phases are allowed in the end. In order to evaluate the performance of this phase discretization method, we design azimuthal multiplexing 3D diffractive optics consisting of two layers, with 128×128 pixels in each layer. In one case, we multiplex two functions, namely "C" and "U" with 0˚ and 90˚ of the rotation angle of the second

layer. In another case, we multiplex four functions of “C”, “U”, “B”, “F” with 0˚, 88˚, 195˚, and 287˚. The diffraction efficiencies are shown in Fig. 5.7.

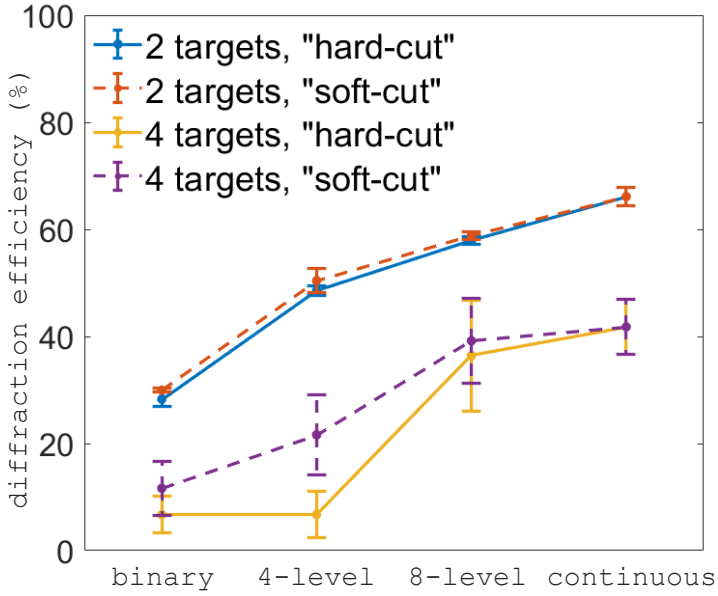

Figure 5.7 Comparison of diffraction efficiency of azimuthal multiplexing 3D diffractive optics designs using different phase discretization methods and number of targets to be multiplexed.

5.5.2 Design with large volumetric space-bandwidth

We show the proposed design method can be extended to obtain results for large volumetric space-bandwidth devices. We design 3D diffractive optics consisting of 16 layers, with 1024×1024 pixels in each layer. The device presents azimuthal multiplexing of four functions representing the letters “C”, “U”, “B”, “F”, each appearing when the last layer is oriented at 0˚, 88˚, 195˚, and 287˚. Fig. 5.8a shows the 16 design phase patterns with 8 quantization levels. The calculation is completed within 24 hours on a PC with Intel-Core i7-8700 CPU at 3.2GHz and 16GB RAM. The diffraction efficiencies are improved to 55.95%, 56.32%, 60.46%, 52.50% for each reconstructed pattern (Fig. 5.8b).

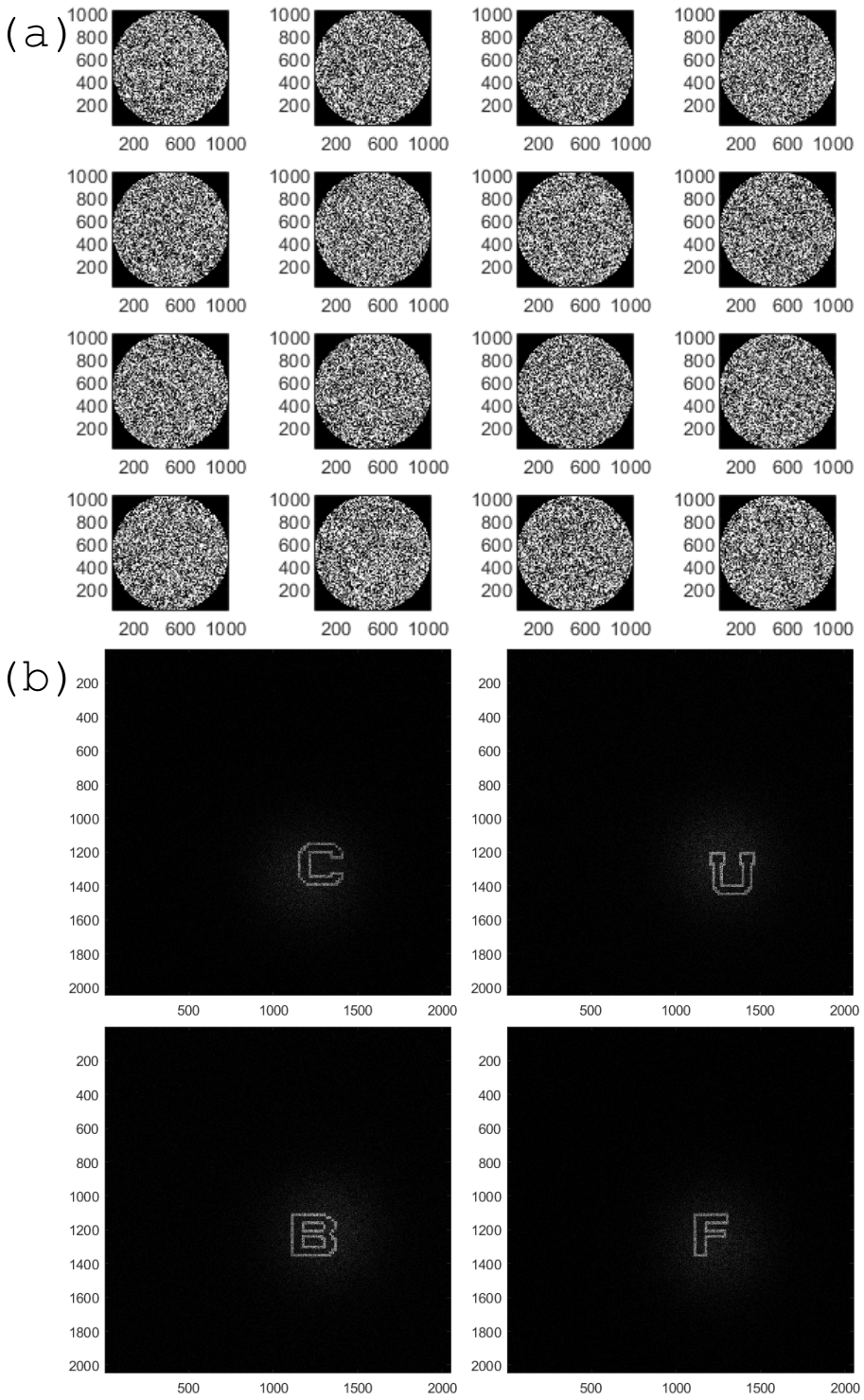

Figure 5.8 Demonstration design of azimuthal multiplexing 3D diffractive optics with large volumetric space-bandwidth product. (a) Azimuthal multiplexing 3D diffractive optics with 16 layers and 1024×1024 pixels in each layer. (b) Reconstructed patterns when the last layer is rotated at 0˚, 88˚, 195˚, and 287˚.

5.5.3 Diffraction efficiency characterization

We study numerically the effect of system parameters on the diffraction efficiency (DE). The diffraction efficiency is defined as the ratio of the intensity in the target area to the intensity of the input beam. We multiplex 4 functions representing the letters “C”, “U”, “B”, “F”. We change the number of layers from 2 to 16 and the number of pixels in each layer from 128 to 1024. We record the mean of the 4 diffraction efficiencies and the result is shown in Fig. 5.9. The diffraction efficiency is enhanced by either increasing the number of layers or the number of pixels. However, the rate of improvement of the DE becomes slower with larger parameters, and saturates at some point. A longer computational time is also required when increasing the number of layers or the number of pixels.

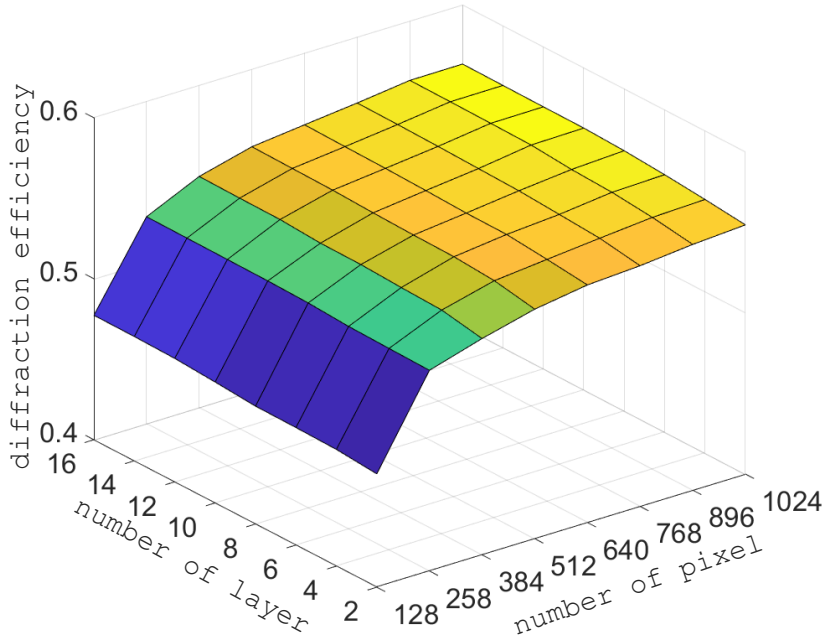

Figure 5.9 The mean of the diffraction efficiencies of “C”, “U”, “B”, “F” as functions of the number of layers and the number of pixels.

5.5.4 Azimuthal multiplexing limit

We investigate the minimum angular interval to avoid crosstalk. We apply the azimuthal multiplexing scheme to two functions, namely the letters "C" and "U". We change their angular interval from 10˚ to 0.1˚, at decrements of 0.1˚. We use the relative error, defined as the ratio of the intensity outside the target area to the one in the target area, to evaluate the quality of the reconstructions. The result is shown in Fig. 5.10(left). The error is higher as we decrease the angular interval, with no crosstalk, partial crosstalk, and complete crosstalk showing in Fig. 5.10(right). We obtain a smaller angular interval without crosstalk by either increasing the number of layers or the number of pixels.

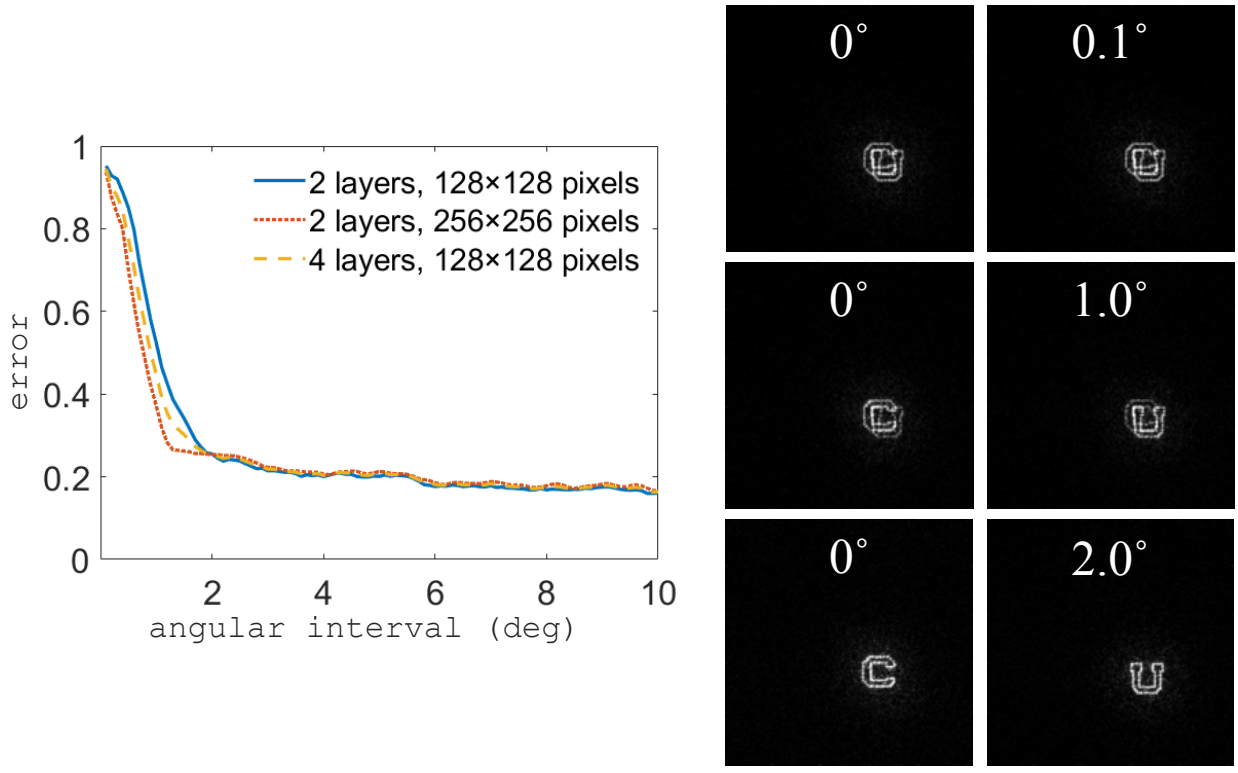

Figure 5.10 Left: The relative error of "C" and "U" as a function of angular interval between the functions. Each point on the plots corresponds to a different design. Right: Simulated reconstructions for angular intervals equal to 0.1˚, 1˚, and 2˚, showing progressive reduction of crosstalk.

5.5.5 Azimuthal selectivity

Azimuthal multiplexing is an important functionality enabled by our proposed 3D diffractive optics. The azimuthal selectivity is the angular interval where the reconstructed patterns are still recognizable. A direct sense of multiplexing system performance can be perceived in Visualization 1. For the design described above, we rotate the second layer 360˚ with respect to the first layer, and record the diffraction efficiency of the 4 encoded patterns around their design angles, as shown in Fig. 5.11. The FWHM of one reconstruction is between 5˚ to 6˚.

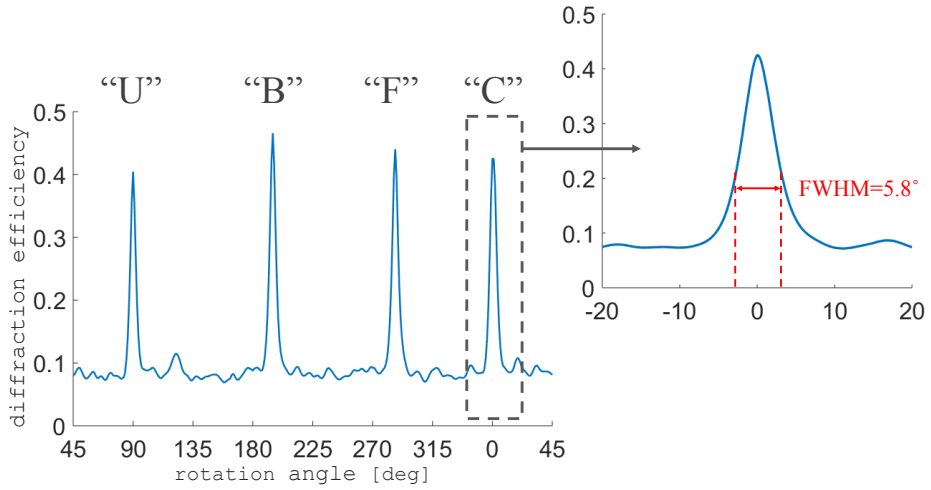

Figure 5.11 Azimuthal selectivity of 3D diffractive optics in the far-field. The diffraction efficiency as a function of rotating angle of the second layer with respect to the first layer. The FWHM of each single reconstruction patterns are between 5˚ to 6˚.

We also investigate the selectivity in the near-field, in non-multiplexing case. To simplify, we use 4 points as the targets. They are located at the 8th, 24th, 40th, and 56th column in the 128 columns target plane. The parameters of the 3D diffractive optics are the same as previous case, except the reconstruction is at 50 μm after the second layer. The selectivity of the 4 points as the second layer rotates in a ±10˚ at the increment of 0.1˚ is shown in Fig. 5.12. We find the azimuthal selectivity in the

near-field depends on the location of the target, i.e. the targets closer to the edge have better selectivity than the ones closer to the center. The reason is that as the layer rotates, the induced pixel changes is proportional to the radial values.

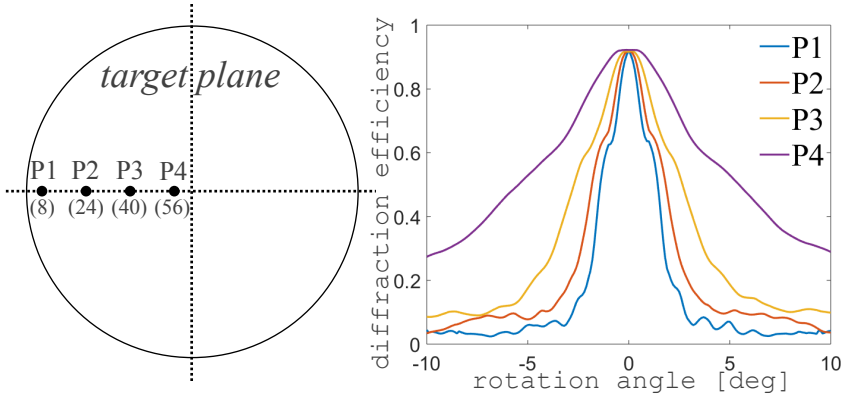

Figure 5.12 The azimuthal selectivity in the near-field for 4 point targets located radially on the target plane. The point closer to the edge has better selectivity than the one close to the cent, indicating the azimuthal selectivity in the near-field depends on target location.

5.6 Azimuthal memory effect

The memory effect refers to an interesting physical phenomenon where optical beams that are sufficiently akin in space or frequency, after propagation through a scattering medium, produce speckle patterns that are highly correlated to one another up to a global transformation. It enables imaging through previously inaccessible environment such as diffusing materials, turbid scatters, or biological tissues. Other than the already reported memory effect including tilt, frequency, and shift, we find a new type of memory effect associated in our proposed 3D diffractive optics. In particular, when we set all the phase modulation layers to be random, a speckle pattern is obtained on the reconstruction plane. As we rotate one or more

layers in the 3D diffractive optics, we find that the speckle pattern also rotates along the same direction in a small angular interval before evolving to a completely new pattern, therefore exhibiting azimuthal memory effect.

We analyze the relation between the speckle correlation and device parameters including the number of layers and the number of rotating layers. In the first case, we set the 3D diffractive optics with 2, 4, and 8 layers, all of which exhibit random phase modulation. We then record the speckle pattern on the reconstruction plane and calculate the cross-correlation with the speckle pattern as we rotate the last layer in a ±5˚ interval with respect to its original orientation. The normalized correlation as a function of rotating angle is shown in Fig. 5.13a. The azimuthal memory effect for different number of layers is almost identical. In the second case, we set the 3D diffractive optics to 8 random layers. We rotate 1, 2, 3, and 4 layers from those 8 layers. The results are shown in Fig. 5.13b. The ranges of azimuthal memory effect are narrower as more layers are involved in the rotation.

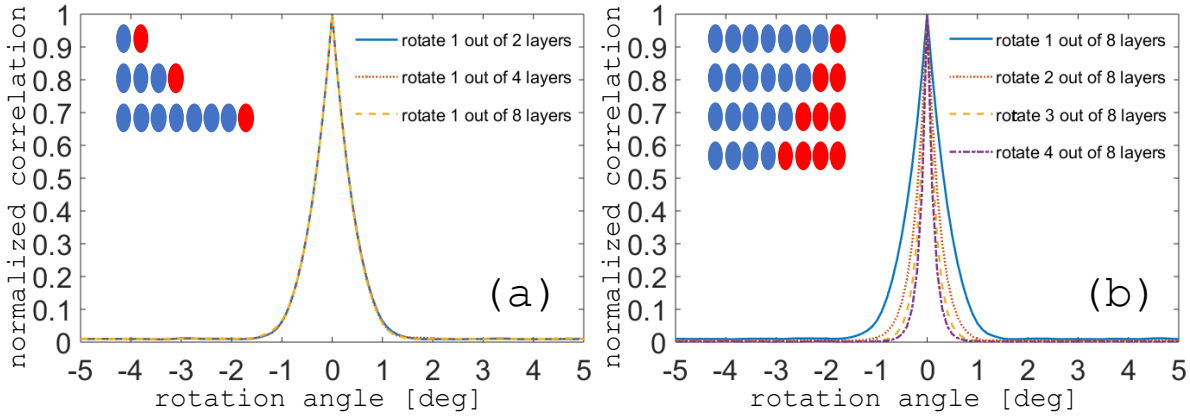

Figure 5.13 Azimuthal memory effect of 3D diffractive optics. (a) The normalized cross-correlation as a function of rotation angle, where we fix the number of rotating layer and change the number of total layers. The blue plate indicates the layer keeps still in the analyzations while the red plate indicates the layer is rotated for the angle in a ±5˚ interval with respect to its original orientation. (b) We conduct the same calculation except the number of total layers is fixed at 8 and the number of rotating layers changes from 1 to 4.

The introduced azimuthal memory effect is intriguing for applications such as information security or imaging through scattering media as discussed in Chapter 6.

5.7 Conclusion

We demonstrated an innovative approach to design and implement azimuthal multiplexing 3D diffractive optics. This is achieved by a stratified DOEs layout with iterative optimization algorithms. As a result, arbitrary optical information can be encoded azimuthally in the 3D diffractive optics and retrieved by rotating part of its components relative to the others. The designs are not based on weakly scattering or the Born approximation enabling for multiple forward scattering events while neglecting the weak backward scattering. This enables higher flexibility and efficiency through the use of high index contrast diffractive layers. The fundamental opportunities and limitations were analyzed, while the experiments using photolithography confirmed the predicted performance.

The results show that extending diffractive optics from two dimensions to three dimensions enables new multiplexing opportunities. Rather than the traditional use of cascaded diffractive optical elements to encode amplitude and phase, our proposed layered 3D diffractive optics is a computationally designed volumetric structure that enables multiplexing. This is the result of multiple independent spatial mode channels being established between the input and the output of the system, reducing the dimensional mismatch essential to the control of light fields in multiple dimensions (spatial, spectral, temporal, or coherence function). The approach also provides a different perspective on 3D diffractive optics design and further

contributes to the inverse problem community by solving the nonlinear inverse problem to achieve a given task using azimuthally rotating phase layers.

A number of applications of azimuthal multiplexing 3D diffractive optics can be envisaged that require switching of different outputs without changing the input and changing the numerical aperture of the system. For instance, information security is a critical issue in optical communication network systems to prevent data acquisition from unauthorized personnel. The proposed azimuthal multiplexing could be applied in information encryption and authentication. The complexity of deciphering the code would increase exponentially as more layers are employed in the 3D diffractive optics. In a different application, it is intriguing to analyze the relation between azimuthal multiplexing and the generation of beams with orbital angular momentum associated with azimuthal phase functions. Such beams have been applied in optical trapping [105], quantum key distribution [106], optical communications [107], and stimulated emission depletion microscopy [108].

Chapter 6

Concluding remarks and future work

6.1 Concluding remarks

Diffractive optics have become critical components in applications such as adaptive optics, optical tweezers, optogenetics, laser lithography, PSF engineering and dynamic structured illumination, all of which are at the forefront of current optics research. However, existing devices cannot access the functionality enabled by volumetric diffractive optics, such as the capability to multiplex different functions, to generate space-variant responses, or to implement wavefront coding. 3D diffractive optics not only enhance the design degrees of freedom and coding capacity, but also enables properties unique to volume (thick) holograms, such as having only one diffraction order, improved efficiency with lower crosstalk, and capability for angular and frequency multiplexing, as demonstrated numerically and experimentally.

This thesis presents the theory of modeling and designing 3D diffractive optics, by full-volume approach and stratified-layer approach. Further, we present the implementation of volume diffractive optics functionality on spatial light modulators that enables dynamic control of high volumetric bandwidth elements. The design

methodology for 3D diffractive optics follows. We introduce a projection onto constraint sets algorithm to solve the inverse design problem.

We implement design examples on a liquid crystal SLM, enabling dynamic and multi-level phase modulation. We theoretically and experimentally investigate the devices in terms of diffraction efficiency and spatial/spectral multiplexing properties. The thesis also introduces the concept of azimuthal multiplexing and presents a design methodology as well as experimental implementation of 3D diffractive optics. We implement design examples on cascaded DOEs fabricated by photolithography, enabling azimuthal multiplexing by rotating one layer with respect to the others. We theoretically and experimentally investigate the devices in terms of diffraction efficiency, reconstruction fidelity, and multiplexing capacity.

6.2 Future work

6.2.1 3D field controlling

In principle, 2D diffractive optical elements are capable of controlling optical waves in three dimensions. The applications include information display, energy distribution, optoelectronic interconnections, and precision measurements. As the 2D elements upgrade to 3D, a number of new functionalities can be envisaged. For example, the multiplexing of several 3D fields in a single 3D diffractive optics, namely different 3D field can be encoded and retrieved with different parameters of the input beam such as wavelength, phase, or incident angle. With the azimuthal multiplexing scheme, it is also possible to obtain different outputs by rotating one or more layers in the 3D diffractive optics.

Point spread function (PSF) engineering is one of the cornerstones in modern microscopy. The point spread function is the response of an imaging system to a point source. Traditionally, a desired PSF can be generated by placing a phase or amplitude mask in the Fourier plane of the imaging system [109]. Here, with the 3D diffractive optics, we can conduct 3D PSF engineering such as generation of double-helix point-spread functions.

Double helix is a powerful 3D PSF for depth estimation with two main lobes rotating continuously with defocus. With iterative projection optimization algorithm, each 2D transverse plane of the desired 3D intensity distribution is applied as a constraint. The iterative optimization procedure enforces those constraints specifically designed for achieving PSF rotation, as well as enhancing efficiency in the PSF main lobes and ensuring a phase-only design result. To impose PSF rotation, the phase pattern can be decomposed into Gauss-Laguerre (GL) modes and multiply a weight function. This is to boost the modes that lie on a cloud around the line defining the exact rotating PSF. The cloud weight function can be expressed as:

$$d(m,n)=\Pi_{k=1}^{N}\left[(m-m_k)^2+(n-n_k)^2\right]^p \tag{6.1}$$

where m and n are the indices of the GL modal plane, m_k and n_k are the m and n indicies of the k^{th} GL mode along the rotating PSF line, N is the number of modes selected along the rotating PSF line, and p is a parameter that determines the width of the cloud. The weight function is directly obtained as:

$$w_{gl}(m,n)=\max\left[d(m,n)\right]-d(m,n) \tag{6.2}$$

To improve the efficiency of the main lobes of the entire 3D PSF, we compute the coherent PSF for a particular defocus value and multiply by a weight function to boost the main lobes at that position. The weight function consists of two spatially

separated Gaussians whose locations and widths are the same as those of the main lobes of the rotating PSF. Due to the continuous rotation of the PSF, the weight functions need to change values accordingly.

The possibilities of creating arbitrary, complex, 3D PSFs open up new opportunities in 3D microscopy with super-resolution [110–112], as well as several other fields such as optical manipulation, optical trapping, 3D display, coherent control, and nanophotonics.

6.2.2 Wavefront aberration correction using 3D diffractive optics

3D diffractive optics designed by the stratified-layer approach is also capable of controlling the phase. Generally speaking, the phase control is more difficult than amplitude. The reason is that when the amplitude is the constraint, the phase is a free parameter. The amplitude outside the target area provides free parameters as well. They both enable the algorithm to converge. However, when the phase is the constraint, the amplitude is uniform by default, which means there are fewer free parameters.

Here we show an example of wavefront aberration correction. We consider two beams incident on a plano-convex lens with focal length of 100mm, as shown in Fig. 6.1a. The spot fields at the focal plane are shown in Fig. 6.1b, while the wavefront aberrations are shown in Fig. 6.1c.

We derive the Zernike coefficients for the two beams and find the terms described coma to be -2.453 and -4.884, respectively. Accordingly, the phase pattern and the corresponding PSF can be obtained (Fig. 6.2), and the task is to generate the conjugate from of the aberrated phase.

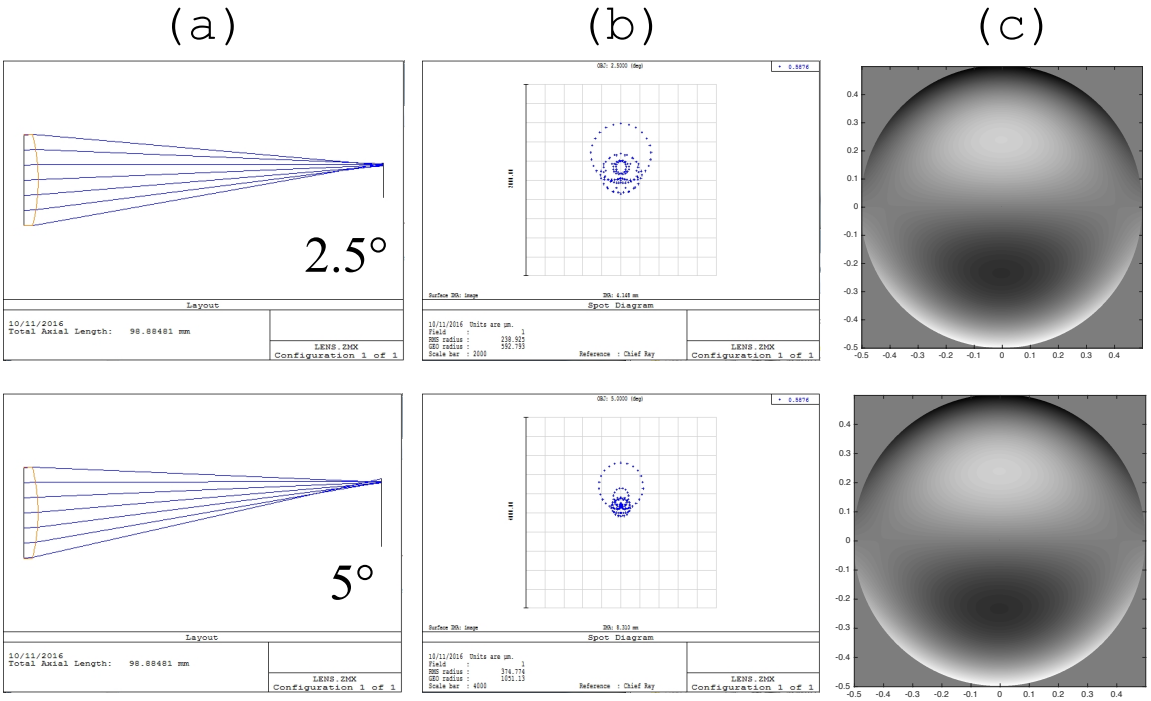

Figure 6.1 Simulation results of two beams incident on a plano-convex lens with focal length 100mm. (a) Ray tracing from the lens to the focal plane. (b) Spot field at the focal plane. (c) Wavefront aberration at the focal plane.

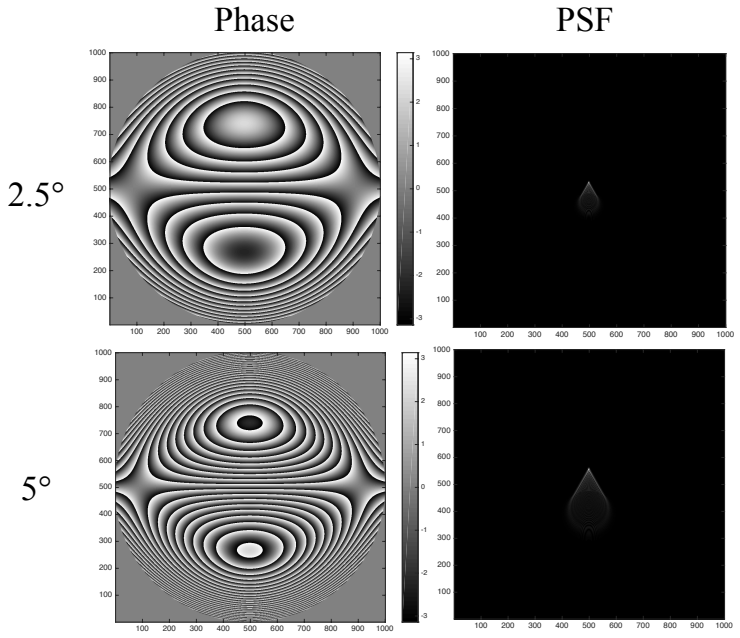

Figure 6.2 Aberrated phase pattern with the corresponding PSF for the beam with incident angle of 2.5° and 5°.

Here we use 4 layers and each layer has 512×512 pixels. Fig. 6.3a shows the design results and Fig. 6.3b shows the reconstructed phase pattern. We add two more phase patterns at minus 2.5 degree and 5 degree. This is beyond the capability of traditional adaptive optics, which can only correct the wavefront aberrations in one direction.

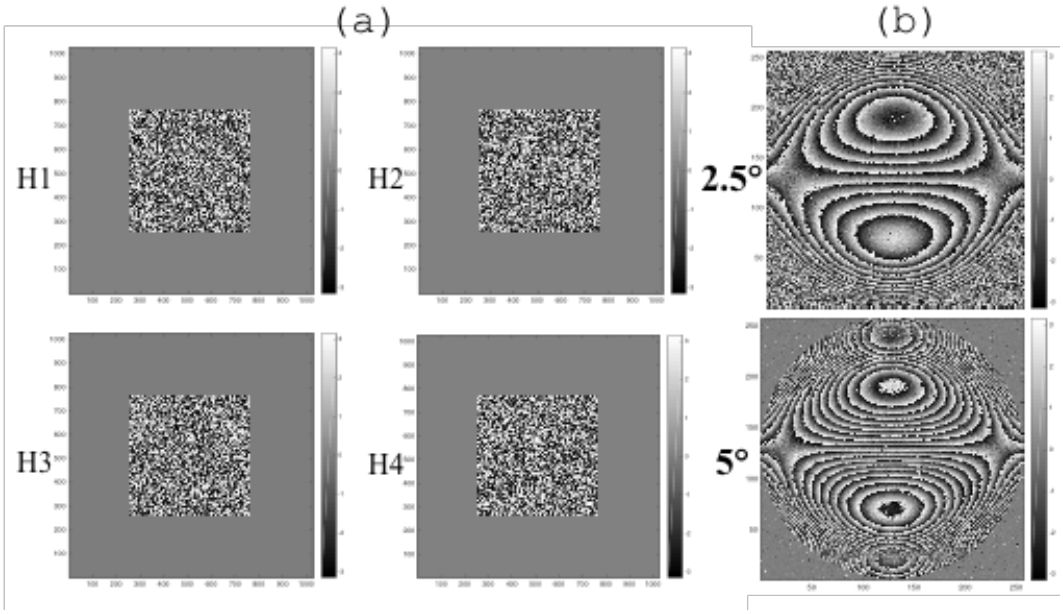

Figure 6.3 Design results for 3D diffractive optics with 4 layers to compensate wavefront aberration. (a) The designed phase pattern of the 4 layers. (b) The reconstructed phase pattern with incident angle of 2.5˚ and 5˚.

6.2.3 Azimuthal memory effect in 3D diffractive optics

3D diffractive optics can emulate scattering media, when the modulation is set to be random values. With stratified-layer model, the total number of layers is positively related to the scattering strength, and the layer separation is similar to the mean free path. We observe memory effect associated with 3D diffractive optics,

namely the speckle pattern on the reconstruction plane experiences decreasing correlation as we change the incident angle or input wavelength.

An interesting work is to explore the effect of the parameters of 3D diffractive optics on different types of memory effect. For instance, we explore the frequency memory effect. We use 2 layers, each layer has 256×256 pixels, and they are separated by 486 μm. We set both layers to be phase-only, and in random value, as shown in Fig. 6.4a. As a result, we obtain speckle patterns when we illuminate the device with 633nm or 532nm (Fig. 6.4b).

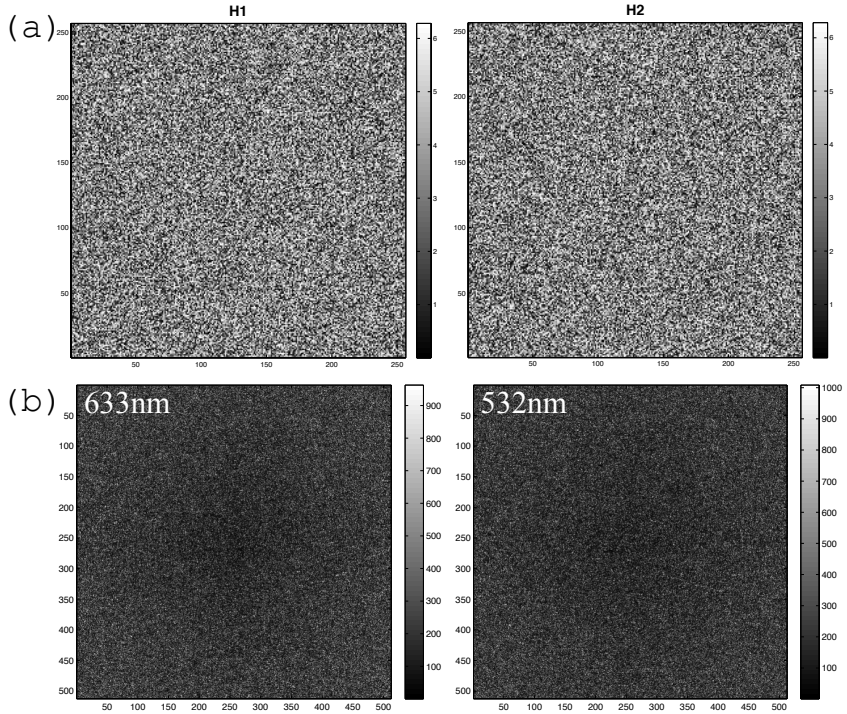

Figure 6.4 3D diffractive optics simulate random scattering media. (a) two layers of phase-only modulation are set to random values. (b) Different speckle patterns are obtained with 633nm and 532nm illumination.

We then calculate the cross-correlation between these two patterns and repeat as we change the wavelength for other values in between. Experimentally, this can be verified with a supercontinuum laser and AOTF. The results are plotted in Fig.

6.5a. We then repeat the above process for 4 layers and 8 layers. The memory effect is plotted in Fig. 6.5b.

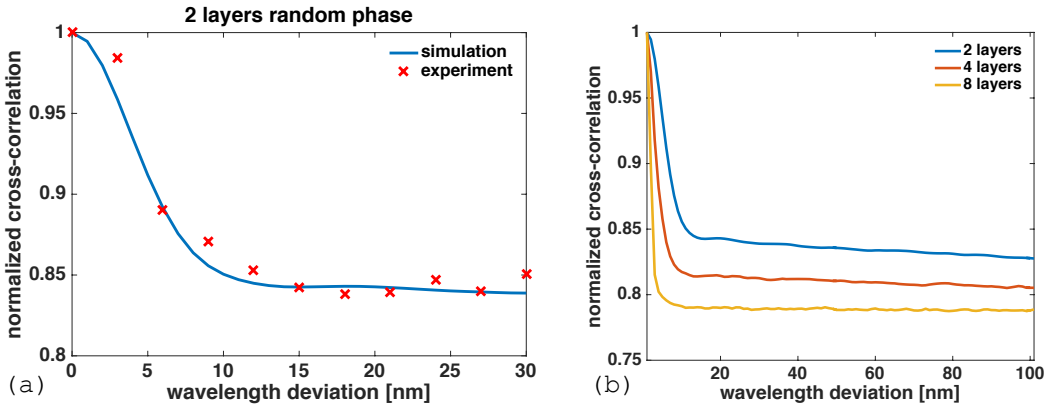

Figure 6.5 Results for frequency memory effect in 3D diffractive optics. (a) simulation and experiment results with 2 layers of random phase. (b) memory effect as number of layers to be 2, 4, and 8.

With azimuthal multiplexing scheme, there is a new type of memory effect, and we call it azimuthal memory effect. Instead of the speckle pattern shifting and evolving to a new pattern as in angular memory effect, or the speckle pattern scaling and evolving to a new pattern as in the frequency memory effect, in the azimuthal memory effect the speckle pattern rotates as we rotate one or more layers of the DOE, and then evolves to a new pattern. Interestingly, the azimuthal memory effect not only relates to the total number of layers in the 3D diffractive optics, but also the number of layers being rotated, and the order of the layer being rotated. This new type of memory effect is worth exploring as well as its potential applications.

Bibliography

1. D. G. Grier, "A revolution in optical manipulation," Nature **424**, 810–816 (2003).

2. J. B. Pendry, D. Schurig, and D. R. Smith, "Controlling Electromagnetic Fields," Science **312**, 1780–1782 (2006).

3. K. Dholakia and T. Čižmár, "Shaping the future of manipulation," Nat. Photonics **5**, 335–342 (2011).

4. A. Zhan, S. Colburn, C. M. Dodson, and A. Majumdar, "Metasurface Freeform Nanophotonics," Sci. Rep. **7**, 1673 (2017).

5. M. Bawart, S. Bernet, and M. Ritsch-Marte, "Programmable freeform optical elements," Opt. Express **25**, 4898–4906 (2017).

6. Y. Jin, R. Kumar, O. Poncelet, O. Mondain-Monval, and T. Brunet, "Flat acoustics with soft gradient-index metasurfaces," Nat. Commun. **10**, 143 (2019).

7. L. Huang, X. Chen, H. Mühlenbernd, H. Zhang, S. Chen, B. Bai, Q. Tan, G. Jin, K.-W. Cheah, C.-W. Qiu, J. Li, T. Zentgraf, and S. Zhang, "Three-dimensional optical holography using a plasmonic metasurface," Nat. Commun. **4**, 2808 (2013).

8. D. Neshev and I. Aharonovich, "Optical metasurfaces: new generation building blocks for multi-functional optics," Light Sci. Appl. **7**, 58 (2018).

9. D. GABOR, "A New Microscopic Principle," Nature **161**, 777 (1948).

10. M. Born and E. Wolf, Principles of Optics, 7th ed. (Cambridge Univ. Press, 1999).

11. A. W. Lohmann and D. P. Paris, "Binary Fraunhofer Holograms, Generated by Computer," Appl. Opt. **6**, 1739–1748 (1967).

12. J. Rosen, M. Segev, and A. Yariv, "Wavelength-multiplexed computer-generated volume holography," Opt. Lett. **18**, 744–746 (1993).

13. R. Piestun and J. Shamir, "Control of wave-front propagation with diffractive elements," Opt. Lett. **19**, 771–773 (1994).

14. S. Borgsmüller, S. Noehte, C. Dietrich, T. Kresse, and R. Männer, "Computer-generated stratified diffractive optical elements," Appl. Opt. **42**, 5274–5283 (2003).

15. W. Cai, T. J. Reber, and R. Piestun, "Computer-generated volume holograms fabricated by femtosecond laser micromachining," Opt. Lett. **31**, 1836–1838 (2006).

16. T. D. Gerke and R. Piestun, "Aperiodic volume optics," Nat. Photonics **4**, 188–193 (2010).

17. H. Wang and R. Piestun, "Dynamic 2D implementation of 3D diffractive optics," Optica **5**, 1220–1228 (2018).

18. J. S. Liu and M. R. Taghizadeh, "Iterative algorithm for the design of diffractive phase elements for laser beam shaping," Opt. Lett. **27**, 1463–1465 (2002).

19. A. J. Caley, M. J. Thomson, J. Liu, A. J. Waddie, and M. R. Taghizadeh, "Diffractive optical elements for high gain lasers with arbitrary output beam profiles," Opt. Express **15**, 10699–10704 (2007).

20. H. Yu, K. Lee, J. Park, and Y. Park, "Ultrahigh-definition dynamic 3D holographic display by active control of volume speckle fields," Nat. Photonics **11**, nphoton.2016.272 (2017).

21. J. Jia, J. Chen, J. Yao, and D. Chu, "A scalable diffraction-based scanning 3D colour video display as demonstrated by using tiled gratings and a vertical diffuser," Sci. Rep. **7**, 44656 (2017).

22. P. Refregier and B. Javidi, "Optical image encryption based on input plane and Fourier plane random encoding," Opt. Lett. **20**, 767–769 (1995).

23. Y. Shi, G. Situ, and J. Zhang, "Multiple-image hiding in the Fresnel domain," Opt. Lett. **32**, 1914–1916 (2007).

24. G. D. Goodno, G. Dadusc, and R. J. D. Miller, "Ultrafast heterodyne-detected transient-grating spectroscopy using diffractive optics," JOSA B **15**, 1791–1794 (1998).

25. G. S. Spagnolo and D. Ambrosini, "Diffractive optical element-based profilometer for surface inspection," Opt. Eng. **40**, 44–53 (2001).

26. D. Dewey, T. H. Markert, and M. L. Schattenburg, "Diffractive-optic telescope for x-ray astronomy," in Multilayer and Grazing Incidence X-Ray/EUV Optics III (International Society for Optics and Photonics, 1996), Vol. 2805, pp. 224–236.

27. D. B. Conkey, R. P. Trivedi, S. R. P. Pavani, I. I. Smalyukh, and R. Piestun, "Three-dimensional parallel particle manipulation and tracking by integrating holographic optical tweezers and engineered point spread functions," Opt. Express **19**, 3835–3842 (2011).

28. A. Jesacher, S. Bernet, and M. Ritsch-Marte, "Combined holographic optical trapping and optical image processing using a single diffractive pattern displayed on a spatial light modulator," Opt. Lett. **39**, 5337–5340 (2014).

29. L. Sacconi, E. Froner, R. Antolini, M. R. Taghizadeh, A. Choudhury, and F. S. Pavone, "Multiphoton multifocal microscopy exploiting a diffractive optical element," Opt. Lett. **28**, 1918–1920 (2003).

30. O. Hernandez, E. Papagiakoumou, D. Tanese, K. Fidelin, C. Wyart, and V. Emiliani, "Three-dimensional spatiotemporal focusing of holographic patterns," Nat. Commun. **7**, 11928 (2016).

31. M. Aeschlimann, M. Bauer, D. Bayer, T. Brixner, F. J. García de Abajo, W. Pfeiffer, M. Rohmer, C. Spindler, and F. Steeb, "Adaptive subwavelength control of nano-optical fields," Nature **446**, 301–304 (2007).

32. O. Tzang, A. M. Caravaca-Aguirre, K. Wagner, and R. Piestun, "Adaptive wavefront shaping for controlling nonlinear multimode interactions in optical fibres," Nat. Photonics **12**, 368–374 (2018).

33. M. T. Gruneisen, W. A. Miller, R. C. Dymale, and A. M. Sweiti, "Holographic generation of complex fields with spatial light modulators: application to quantum key distribution," Appl. Opt. **47**, A32–A42 (2008).

34. J. C. T. Lee, S. J. Alexander, S. D. Kevan, S. Roy, and B. J. McMorran, "Laguerre–Gauss and Hermite–Gauss soft X-ray states generated using diffractive optics," Nat. Photonics 1 (2019).

35. X. Lin, Y. Rivenson, N. T. Yardimci, M. Veli, Y. Luo, M. Jarrahi, and A. Ozcan, "All-optical machine learning using diffractive deep neural networks," Science **361**, 1004–1008 (2018).

36. J. Chang, V. Sitzmann, X. Dun, W. Heidrich, and G. Wetzstein, "Hybrid optical-electronic convolutional neural networks with optimized diffractive optics for image classification," Sci. Rep. **8**, 12324 (2018).

37. L. Golan, I. Reutsky, N. Farah, and S. Shoham, "Design and characteristics of holographic neural photo-stimulation systems," J. Neural Eng. **6**, 066004 (2009).

38. S. Bovetti, C. Moretti, S. Zucca, M. D. Maschio, P. Bonifazi, and T. Fellin, "Simultaneous high-speed imaging and optogenetic inhibition in the intact mouse brain," Sci. Rep. **7**, 40041 (2017).

39. T. G. Bifano, J. Perreault, R. K. Mali, and M. N. Horenstein, "Microelectromechanical deformable mirrors," IEEE J. Sel. Top. Quantum Electron. **5**, 83–89 (1999).

40. F. O. Fahrbach, F. F. Voigt, B. Schmid, F. Helmchen, and J. Huisken, "Rapid 3D light-sheet microscopy with a tunable lens," Opt. Express **21**, 21010–21026 (2013).

41. V. Bansal and P. Saggau, "Digital Micromirror Devices: Principles and Applications in Imaging," Cold Spring Harb. Protoc. **2013**, pdb.top074302 (2013).

42. K. P. Thompson and J. P. Rolland, "Freeform Optical Surfaces: A Revolution in Imaging Optical Design," Opt. Photonics News **23**, 30–35 (2012).

43. P. Berto, L. Philippet, J. Osmond, C. F. Liu, A. Afridi, M. M. Marques, B. M. Agudo, G. Tessier, and R. Quidant, "Tunable and free-form planar optics," Nat. Photonics **13**, 649–656 (2019).

44. P. Lalanne and P. Chavel, "Metalenses at visible wavelengths: past, present, perspectives," Laser Photonics Rev. **11**, (2017).

45. B. Wang, F. Dong, Q.-T. Li, D. Yang, C. Sun, J. Chen, Z. Song, L. Xu, W. Chu, Y.-F. Xiao, Q. Gong, and Y. Li, "Visible-Frequency Dielectric Metasurfaces for Multiwavelength Achromatic and Highly Dispersive Holograms," Nano Lett. **16**, 5235–5240 (2016).

46. Q. Wang, E. T. F. Rogers, B. Gholipour, C.-M. Wang, G. Yuan, J. Teng, and N. I. Zheludev, "Optically reconfigurable metasurfaces and photonic devices based on phase change materials," Nat. Photonics **10**, 60–65 (2016).

47. U. Leonhardt, "Optical Conformal Mapping," Science **312**, 1777–1780 (2006).

48. J. Li and J. B. Pendry, "Hiding under the Carpet: A New Strategy for Cloaking," Phys. Rev. Lett. **101**, 203901 (2008).

49. S. John, "Strong localization of photons in certain disordered dielectric superlattices," Phys. Rev. Lett. **58**, 2486–2489 (1987).

50. A. W. Lohmann, R. G. Dorsch, D. Mendlovic, Z. Zalevsky, and C. Ferreira, "Space-bandwidth product of optical signals and systems," J. Opt. Soc. Am. A **13**, 470 (1996).

51. R. Piestun and D. A. B. Miller, "Electromagnetic degrees of freedom of an optical system," J. Opt. Soc. Am. A **17**, 892 (2000).

52. R. Piestun and C. M. de Sterke, "Fundamental limit for two-dimensional passive devices," Opt. Lett. **34**, 779 (2009).

53. T. D. Gerke and R. Piestun, "Aperiodic computer-generated volume holograms improve the performance of amplitude volume gratings," Opt. Express **15**, 14954–14960 (2007).

54. R. Piestun and J. Shamir, "Synthesis of three-dimensional light fields and applications," Proc. IEEE **90**, 222–244 (2002).

55. R. Piestun, B. Spektor, and J. Shamir, "Wave fields in three dimensions: analysis and synthesis," J. Opt. Soc. Am. A **13**, 1837–1848 (1996).

56. R. Gerchberg and W. Saxton, "A practical algorithm for the determination of the phase from image and diffraction plane pictures," Opt. Jena **35**, 237 (1972).

57. J. R. Fienup, "Phase retrieval algorithms: a comparison," Appl. Opt. **21**, 2758–2769 (1982).

58. R. W. Gerchberg, "Super-resolution through Error Energy Reduction," Opt. Acta Int. J. Opt. **21**, 709–720 (1974).

59. A. Papoulis, "A new algorithm in spectral analysis and band-limited extrapolation," IEEE Trans. Circuits Syst. **22**, 735–742 (1975).

60. F. Wyrowski and O. Bryngdahl, "Iterative Fourier-transform algorithm applied to computer holography," J. Opt. Soc. Am. A **5**, 1058–1065 (1988).

61. H. Stark and Y. Young, Vector Space Projections: A numerical Approach to Signal and Image Processing, Neural Nets, and Optics, (Wiley, New York, 1998).

62. J. A. Fleck, J. R. Morris, and M. D. Feit, "Time-dependent propagation of high energy laser beams through the atmosphere," Appl. Phys. **10**, 129–160 (1976).

63. D. Psaltis, M. Levene, A. Pu, G. Barbastathis, and K. Curtis, "Holographic storage using shift multiplexing," Opt. Lett. **20**, 782–784 (1995).

64. J. E. Curtis, B. A. Koss, and D. G. Grier, "Dynamic holographic optical tweezers," Opt. Commun. **207**, 169–175 (2002).

65. E. Schonbrun, R. Piestun, P. Jordan, J. Cooper, K. D. Wulff, J. Courtial, and M. Padgett, "3D interferometric optical tweezers using a single spatial light modulator," Opt. Express **13**, 3777–3786 (2005).

66. M. Makowski, M. Sypek, I. Ducin, A. Fajst, A. Siemion, J. Suszek, and A. Kolodziejczyk, "Experimental evaluation of a full-color compact lensless holographic display," Opt. Express **17**, 20840–20846 (2009).

67. S. Fürhapter, A. Jesacher, S. Bernet, and M. Ritsch-Marte, "Spiral phase contrast imaging in microscopy," Opt. Express **13**, 689–694 (2005).

68. B. Nie, I. Saytashev, A. Chong, H. Liu, S. N. Arkhipov, F. W. Wise, and M. Dantus, "Multimodal microscopy with sub-30 fs Yb fiber laser oscillator," Biomed. Opt. Express **3**, 1750–1756 (2012).

69. S. R. P. Pavani and R. Piestun, "Three dimensional tracking of fluorescent microparticles using a photon-limited double-helix response system," Opt. Express **16**, 22048–22057 (2008).

70. V. Nikolenko, B. O. Watson, R. Araya, A. Woodruff, D. S. Peterka, and R. Yuste, "SLM Microscopy: Scanless Two-Photon Imaging and Photostimulation with Spatial Light Modulators," Front. Neural Circuits **2**, 5 (2008).

71. Y. Kuroiwa, N. Takeshima, Y. Narita, S. Tanaka, and K. Hirao, "Arbitrary micropatterning method in femtosecond laser microprocessing using diffractive optical elements," Opt. Express **12**, 1908–1915 (2004).

72. A. Jesacher and M. J. Booth, "Parallel direct laser writing in three dimensions with spatially dependent aberration correction," Opt. Express **18**, 21090–21099 (2010).

73. H. Bartelt, "Computer-generated holographic component with optimum light efficiency," Appl. Opt. **23**, 1499–1502 (1984).

74. D. Brady and D. Psaltis, "Control of volume holograms," JOSA A **9**, 1167–1182 (1992).

75. R. V. Johnson and A. R. Tanguay, "Stratified volume holographic optical elements," Opt. Lett. **13**, 189–191 (1988).

76. G. P. Nordin, R. V. Johnson, and A. R. Tanguay, "Diffraction properties of stratified volume holographic optical elements," JOSA A **9**, 2206–2217 (1992).

77. G. Labroille, B. Denolle, P. Jian, P. Genevaux, N. Treps, and J.-F. Morizur, "Efficient and mode selective spatial mode multiplexer based on multi-plane light conversion," Opt. Express **22**, 15599–15607 (2014).

78. F. Yaraş, H. Kang, and L. Onural, "Real-time phase-only color holographic video display system using LED illumination," Appl. Opt. **48**, H48–H53 (2009).

79. M. Makowski, I. Ducin, K. Kakarenko, J. Suszek, M. Sypek, and A. Kolodziejczyk, "Simple holographic projection in color," Opt. Express **20**, 25130–25136 (2012).

80. T. Shimobaba, A. Shiraki, N. Masuda, and T. Ito, "An electroholographic colour reconstruction by time division switching of reference lights," J. Opt. Pure Appl. Opt. **9**, 757 (2007).

81. T. R. M. Sales and D. H. Raguin, "Multiwavelength operation with thin diffractive elements," Appl. Opt. **38**, 3012–3018 (1999).

82. U. Levy, E. Marom, and D. Mendlovic, "Simultaneous multicolor image formation with a single diffractive optical element," Opt. Lett. **26**, 1149–1151 (2001).

83. T. Kämpfe, E.-B. Kley, A. Tünnermann, and P. Dannberg, "Design and fabrication of stacked, computer generated holograms for multicolor image generation," Appl. Opt. **46**, 5482–5488 (2007).

84. A. Jesacher, S. Bernet, and M. Ritsch-Marte, "Colour hologram projection with an SLM by exploiting its full phase modulation range," Opt. Express **22**, 20530–20541 (2014).

85. W. Harm, C. Roider, S. Bernet, and M. Ritsch-Marte, "Tilt-effect of holograms and images displayed on a spatial light modulator," Opt. Express **23**, 30497–30511 (2015).

86. S. Colburn, A. Zhan, and A. Majumdar, "Metasurface optics for full-color computational imaging," Sci. Adv. **4**, eaar2114 (2018).

87. S. Wang, P. C. Wu, V.-C. Su, Y.-C. Lai, C. H. Chu, J.-W. Chen, S.-H. Lu, J. Chen, B. Xu, C.-H. Kuan, T. Li, S. Zhu, and D. P. Tsai, "Broadband achromatic optical metasurface devices," Nat. Commun. **8**, 187 (2017).

88. H. Yang, T. Yu, Q. Wang, and M. Lei, "Wave manipulation with magnetically tunable metasurfaces," Sci. Rep. **7**, 5441 (2017).

89. Z. Zhang, Z. You, and D. Chu, "Fundamentals of phase-only liquid crystal on silicon (LCOS) devices," Light Sci. Appl. **3**, e213 (2014).

90. D. Engström, M. Persson, J. Bengtsson, and M. Goksör, "Calibration of spatial light modulators suffering from spatially varying phase response," Opt. Express **21**, 16086–16103 (2013).

91. R. K. Banyal and B. R. Prasad, "Nonlinear response studies and corrections for a liquid crystal spatial light modulator," Pramana **74**, 961–971 (2010).

92. A. Gahlmann, J. L. Ptacin, G. Grover, S. Quirin, A. R. S. von Diezmann, M. K. Lee, M. P. Backlund, L. Shapiro, R. Piestun, and W. E. Moerner, "Quantitative Multicolor Subdiffraction Imaging of Bacterial Protein Ultrastructures in Three Dimensions," Nano Lett. **13**, 987–993 (2013).

93. Y. Shechtman, L. E. Weiss, A. S. Backer, M. Y. Lee, and W. E. Moerner, "Multicolour localization microscopy by point-spread-function engineering," Nat. Photonics **10**, 590–594 (2016).

94. B. Spektor, "Method for sythesizing the phase structure of knoforms," 35–38 (1985).

95. G. Barbastathis and D. Psaltis, "Volume Holographic Multiplexing Methods," in Holographic Data Storage, Springer Series in Optical Sciences (Springer, Berlin, Heidelberg, 2000), pp. 21–62.

96. K. Curtis, A. Pu, and D. Psaltis, "Method for holographic storage using peristrophic multiplexing," Opt. Lett. **19**, 993–994 (1994).

97. G. Barbastathis, M. Levene, and D. Psaltis, "Shift multiplexing with spherical reference waves," Appl. Opt. **35**, 2403–2417 (1996).

98. L. W. Alvarez, "Development of variable- focus lenses and a new refractor," J. Am. Optom. Assoc. **49**, 24–29 (1978).

99. A. W. Lohmann, "A New Class of Varifocal Lenses," Appl. Opt. **9**, 1669–1671 (1970).

100. S. Bernet and M. Ritsch-Marte, "Adjustable refractive power from diffractive moiré elements," Appl. Opt. **47**, 3722–3730 (2008).

101. S. Bernet, W. Harm, and M. Ritsch-Marte, "Demonstration of focus-tunable diffractive Moiré-lenses," Opt. Express **21**, 6955–6966 (2013).

102. J. Goodman, Introduction to Fourier Optics, 3rd Edition edition (Roberts and Company Publishers, 2004).

103. S. R. P. Pavani and R. Piestun, "High-efficiency rotating point spread functions," Opt. Express **16**, 3484–3489 (2008).

104. D. O'Shea, T. Suleski, A. Kathman, and D. Prather, Diffractive Optics: Design, Fabrication, and Test (SPIE PRESS BOOK, 2003).

105. L. Paterson, M. P. MacDonald, J. Arlt, W. Sibbett, P. E. Bryant, and K. Dholakia, "Controlled Rotation of Optically Trapped Microscopic Particles," Science **292**, 912–914 (2001).

106. R. Horstmeyer, B. Judkewitz, I. M. Vellekoop, S. Assawaworrarit, and C. Yang, "Physical key-protected one-time pad," Sci. Rep. **3**, 3543 (2013).

107. A. Mair, A. Vaziri, G. Weihs, and A. Zeilinger, "Entanglement of the orbital angular momentum states of photons," Nature **412**, 313–316 (2001).

108. B. J. McMorran, A. Agrawal, I. M. Anderson, A. A. Herzing, H. J. Lezec, J. J. McClelland, and J. Unguris, "Electron Vortex Beams with High Quanta of Orbital Angular Momentum," Science **331**, 192–195 (2011).

109. J. Durnin, J. J. Miceli, and J. H. Eberly, "Diffraction-free beams," Phys. Rev. Lett. **58**, 1499–1501 (1987).

110. T. A. Planchon, L. Gao, D. E. Milkie, M. W. Davidson, J. A. Galbraith, C. G. Galbraith, and E. Betzig, "Rapid three-dimensional isotropic imaging of living cells using Bessel beam plane illumination," Nat. Methods **8**, 417 (2011).

111. K. I. Willig, S. O. Rizzoli, V. Westphal, R. Jahn, and S. W. Hell, "STED microscopy reveals that synaptotagmin remains clustered after synaptic vesicle exocytosis," Nature **440**, 935 (2006).

112. G. Grover, K. DeLuca, S. Quirin, J. DeLuca, and R. Piestun, "Super-resolution photon-efficient imaging by nanometric double-helix point spread function localization of emitters (SPINDLE)," Opt. Express **20**, 26681–26695 (2012).